Mathematical modelling of host-disease-drug interactions in HIV disease

Dissertation zur Erlangung des Akademischen Grades

"doktor rerum naturalium" (Dr. rer. nat.)

an der Mathematisch-Naturwissenschaftlichen Fakultät

der Universität Potsdam

vorgelegt von

Sathej Gopalakrishnan

March 2016

Supervisor: Prof. Dr. Wilhelm Huisinga
University of Potsdam
Institute for Mathematics & Institute for Biochemistry and Biology
Science Park Golm
Karl-Liebknecht-Str. 24/25
D-14476 Potsdam Golm

Reviewers: Prof. Dr. Joachim Selbig
Prof. Dr. Leon Aarons

Date of PhD defense: 19. September 2016

Published online at the
Institutional Repository of the University of Potsdam:
URN urn:nbn:de:kobv:517-opus4-100100
http://nbn-resolving.de/urn:nbn:de:kobv:517-opus4-100100

Acknowledgements

Numerous people have contributed in different and irreplaceable ways towards the thesis. Firstly, I thank my supervisor Prof Dr Wilhelm Huisinga for his constant support. Starting with offering me the opportunity to be a part of the PharMetrX PhD program, Wilhelm has been a wonderful mentor throughout the PhD project. Be it in one-on-one meetings, informal conversations over coffee or dinner, or even train rides (ideas for a significant part of the current thesis materialized on the train!), I have always gained fresh insights from him. I express my sincere gratitude to Wilhelm for his trust and support, and for the freedom to explore new ideas. There would always be parts of thought processes in me, that I have imbibed (or at least tried to!) from him.

I also thank Prof Dr Charlotte Kloft, Free University Berlin, for several helpful discussions during the PhD, and for her role in enabling valuable exchange within the PharMetrX program.

I thank Hesam Montazeri and Prof Dr Niko Beerenwinkel, ETH Zurich, for the very fruitful collaboration during the project.

I express my sincere gratitude to the Pharmacometrics group at AbbVie Ludwigshafen, in particular my mentor Dr Sven Mensing and Dr Peter Noertersheuser, for their inputs from industry, and for allowing me to present the progress of my thesis at regular intervals in their group.

I warmly thank all my PhD colleagues at University of Potsdam and Free University Berlin for the numerous interesting interactions. In particular, I wish to thank Ludivine Fronton, in whom I gained a true friend. Thanks Ludivine, for all those conversations about everything under the sun, at office, over lunch, and elsewhere. I also want to thank Stephan Menz for being the ever-approachable problem-solver and for just being there, to bounce off ideas! Will remember the reams of C++ code, debugging sessions and those very satisfying joint investigations into the Gauss-Newton method vis a vis regularization. My thanks also to Christoph Hethey for his very pleasant company during the last couple of years of my PhD and for help with the German translation of the abstract of this thesis.

My gratitude goes to my parents for their ever-present support and love. Thanks are also due to my brother for his role in shaping my ideas and thought processes about several things, the precise nature of which would be hard to articulate. Finally, I thank my wife for just being beside me through things, and for all her love, understanding and patience.

This work was funded by the Graduate Research Training Program 'PharMetrx: Pharmacometrics and Computational Disease Modelling'.

Abstract

The human immunodeficiency virus (HIV) has resisted nearly three decades of efforts targeting a cure. Sustained suppression of the virus has remained a challenge, mainly due to the remarkable evolutionary adaptation that the virus exhibits by the accumulation of drug-resistant mutations in its genome. Current therapeutic strategies aim at achieving and maintaining a low viral burden and typically involve multiple drugs. The choice of optimal combinations of these drugs is crucial, particularly in the background of treatment failure having occurred previously with certain other drugs. An understanding of the dynamics of viral mutant genotypes aids in the assessment of treatment failure with a certain drug combination, and exploring potential salvage treatment regimens.

Mathematical models of viral dynamics have proved invaluable in understanding the viral life cycle and the impact of antiretroviral drugs. However, such models typically use simplified and coarse-grained mutation schemes, that curbs the extent of their application to drug-specific clinical mutation data, in order to assess potential next-line therapies. Statistical models of mutation accumulation have served well in dissecting mechanisms of resistance evolution by reconstructing mutation pathways under different drug-environments. While these models perform well in predicting treatment outcomes by statistical learning, they do not incorporate drug effect mechanistically. Additionally, due to an inherent lack of temporal features in such models, they are less informative on aspects such as predicting mutational abundance at treatment failure. This limits their application in analyzing the pharmacology of antiretroviral drugs, in particular, time-dependent characteristics of HIV therapy such as pharmacokinetics and pharmacodynamics, and also in understanding the impact of drug efficacy on mutation dynamics.

In this thesis, we develop an integrated model of *in vivo* viral dynamics incorporating drug-specific mutation schemes learned from clinical data. Our combined modelling approach enables us to study the dynamics of different mutant genotypes and assess mutational abundance at virological failure. As an application of our model, we estimate *in vivo* fitness characteristics of viral mutants under different drug environments. Our approach also extends naturally to multiple-drug therapies. Further, we demonstrate the versatility of our model by showing how it can be modified to incorporate recently elucidated mechanisms of drug action including molecules that target host factors.

Additionally, we address another important aspect in the clinical management of HIV disease, namely drug pharmacokinetics. It is clear that time-dependent changes in *in vivo* drug concentration could have an impact on the antiviral effect, and also influence decisions on dosing intervals. We present a framework that provides an integrated understanding of key characteristics of multiple-dosing regimens including drug accumulation ratios and half-lifes, and then explore the impact of drug pharmacokinetics on viral suppression.

Finally, parameter identifiability in such nonlinear models of viral dynamics is always a concern, and we investigate techniques that alleviate this issue in our setting.

Publications

Parts of this thesis have been published during the PhD.

Chapter 3 and parts of Chapter 4 (Section 4.2) and Chapter 6 (Section 6.2.2) have been published in PLoS Computational Biology in collaboration with Hesam Montazeri, Stephan Menz, Niko Beerenwinkel and Wilhelm Huisinga, with the title 'Estimating HIV-1 Fitness Characteristics from Cross-Sectional Genotype Data'. Parts of Chapter 5 are included in a manuscript under preparation, jointly with Wilhelm Huisinga.

Table of Contents

Chapter 1

Introduction

After thirty years of its discovery, human immunodeficiency virus (HIV) infection leading to Acquired Immunodeficiency Syndrome (AIDS) continues to be amongst the ten leading causes of mortality globally [1]. Inspite of an increased understanding of the viral biology and pathogenesis in recent years, a cure for the disease remains elusive. Promises of continued viral suppression, observed in a few patients, have been belied with the virus showing up, sometimes after a few years [2]. The pace of resistance development and viral adaptation to therapeutic strategies is remarkably rapid and pose a major challenge to clinical management of the disease. As its name suggests, HIV targets the human immune system and markedly increases the body's susceptibility to numerous infections, that would otherwise not pose serious concern. AIDS manifests as a chronic disease, rather than being acutely fatal, and displays a gradual and insidious course. Notwithstanding this pessimistic picture, our understanding of the virus and the disease have not entirely been in vain. Viral suppression can be achieved and maintained in patients, with right and timely choices of treatment interventions.

Several anti-HIV drugs have been approved and are used to suppress viral replication. The current standard therapeutic recommendations involve a combination of these drugs, rather than a single drug. A principal conundrum in the context of clinical management of HIV infection is the choice of optimal combinations of these drugs [3, 4], particularly in a background of treatment failure having occurred previously with certain other drugs (Figure 1.1). Viral load measurements and viral genotype sequences at the point of treatment failure are generally two of the most common sources of information available to the clinician, who then makes a decision on the next-line combination of drugs that would salvage the situation. An understanding of the causes and mechanisms of treatment failure is crucial in this process of deciding on potential next-line drug combinations.

To analyze failed drug combinations and evaluate a variety of salvage treatment options, one can utilize both experimental and theoretical resources. While experimental assays are admittedly indispensable in assisting our understanding of drug resistance and viral replication, they clearly do not suffice in the face of the multitude of viral genotypes present in patient populations and the variety of drug combinations available. Mathematical models of HIV infection have advanced the understanding of viral replication processes, drug effects, viral evolution and treatment outcomes. Mechanistic models of viral dynamics [5–7] have afforded valuable insights on replication and infection processes. In addition, they have enabled us to examine the impact of drugs on the complex viral life cycle and dissect the mechanisms of action of different drug classes. However, such models typically use simplified and coarse-grained mutation schemes, thereby rendering a direct comparison of their predictions to clinical data on mutations and resistance difficult. This

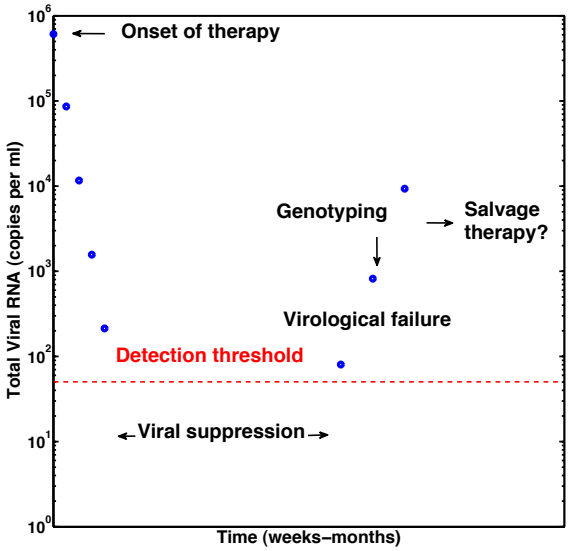

Figure 1.1. The clinical choice. Initial therapy in a HIV-infected person suppresses viral load for a certain time before virological failure occurs with viral RNA being detected (when present above 50 copies/ml) in blood. Viral load measurements and viral genotype sequence at therapy failure are available to the clinician who then has to recommend a potential next-line salvage therapy.

curbs their application in assessing treatment failure with a certain drug combination and exploring different potential follow-up regimens *in silico*. Statistical models of mutation development learned from clinical data [8–10], on the other hand, have helped in revealing evolutionary pathways that the virus adopts to overcome drug pressure. While these models perform very well in predicting treatment outcomes by statistical learning, they lack a mechanistic incorporation of drug effect. Such models also inherently lack temporal features and hence are less informative on aspects such as predicting mutational abundance at treatment failure. This limits their application in analyzing the pharmacology of antiretroviral drugs, in particular, time-dependent characteristics of HIV therapy such as pharmacokinetics and pharmacodynamics.

The evolutionary success of the primitive life-form that HIV is, has engaged the scientific curiosity of researchers over the last couple of decades [11, 12]. The virus undergoes several changes in its genomic sequence and continually adapts itself to changing environments. Resistance to drugs is an emergent property owing to such adaptation. While Darwinian principles remain the governing basis for HIV evolution, the complexities in the different host-drug environments, and evolutionary constraints and bottlenecks present challenges in terms of understanding how HIV adapts to different drugs. The fitness of the virus is a quantifier of the evolutionary advantage that one viral variant has over another. The knowledge of fitness characteristics of the viral population aids in assessing causes of failure of certain drug combinations and helps understand viral evolutionary principles.

In this thesis, we analyze HIV treatment failure by developing mechanistic models of the viral life cycle that incorporate drug-specific mutation schemes statistically learned from clinical data. The combination of these two distinct modelling approaches provides a better understanding of the dynamics of drug-resistant mutant genotypes and mutational

abundance at virological failure. As an application of our model, we estimate *in vivo* fitness characteristics of different viral mutants in the absence and presence of drugs and are able to better understand mechanisms involved in HIV evolution. Importantly, our approach relies only on sparse clinical data, as opposed to detailed time-course measurements of viral load. Additionally, our modelling approach easily generalizes to multiple-drug therapy and we are able to analyze how individual drugs in a combination regimen impact treatment outcome.

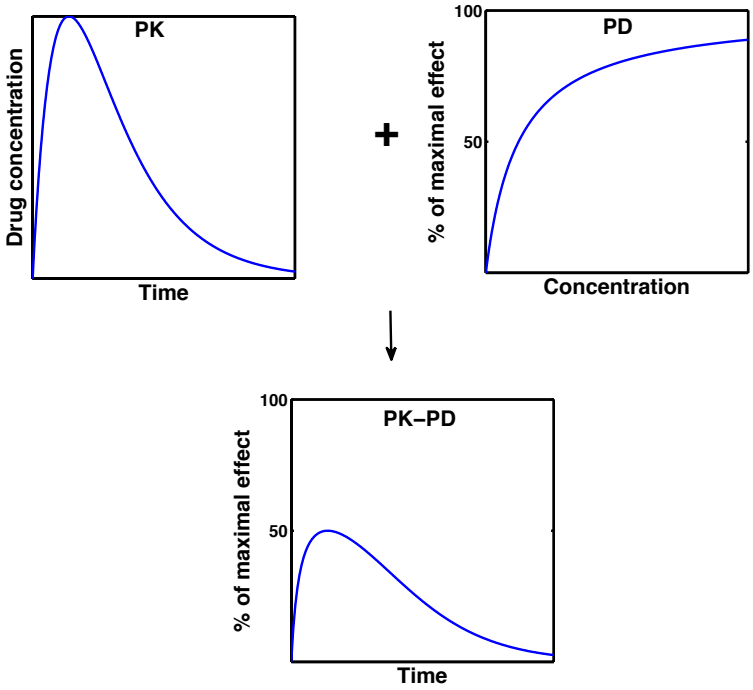

Figure 1.2. Pharmacokinetics and pharmacodynamics interplay. The pharmacokinetics (PK) of a drug describes the variations in its concentration in the body over time, while the pharmacodynamics (PD) of the drug relates its effect and concentration. A combined PK-PD relationship characterizes the drug effect as a function of time.

Another important aspect in the clinical management of a disease is the pharmacokinetics (PK) of drugs adminstered for therapy. It is clear that when a patient infected with HIV is administered a certain drug (or a combination of drugs), the drug concentration changes with time owing to processes such as absorption, distribution, metabolism and elimination of the drug. These factors determine the PK of the drug within the body (i.e, what the body does to the drug) and influence decisions on dosing intervals, for example. The time-dependent changes in drug concentration of an anti-HIV drug could also impact its antiviral effect (Figure 1.2). Further, the long-term nature of therapy in HIV raises questions concerning drug accumulation and half-life. Understanding drug PK associated with multiple dosing thus plays an important role in the development of new antiviral drug molecules, and to devise safe and efficacious dosage regimens.

Pharmacokinetic modelling of drugs has a long history [13,14]. However, most mechanistic models of viral dynamics assume constant drug concentration, mainly for purposes of simplicity [5–7]. In this thesis, to understand the PK of anti- HIV drugs under a multiple dosing scenario, we first develop a framework that provides an integrated under-

standing of different measures of drug accumulation and half-lifes. In drugs displaying a multi-phasic decline in their concentration, reporting only one half-life or measure of accumulation could lead to apparent contradictions [15]. Our framework enables an easy interpretation and a concise understanding of several summary measures of multiple dose PK. We also explore the impact of PK on viral suppression by coupling PK models to models of viral dynamics.

Finally, in the context of such complex nonlinear models of viral dynamics, parameter estimation and identifiability always pose several challenges. We investigate techniques to alleviate these issues in our setting.

This thesis is organized as follows. In Chapter 2, we briefly review the biological aspects of HIV infection and disease and discuss different modelling approaches used to investigate viral dynamics, mutations and antiviral drug action. In Chapter 3, we present a model of *in vivo* viral dynamics that incorporates drug-specific mutation schemes and focus on the estimation of various fitness characteristics of HIV mutants from clinical data. Next, in Chapter 4, we describe how our model generalizes to drug combinations and present simulation results from dual and triple-drug therapies. Further, we also demonstrate how our model can be extended to incorporate the action of antiviral molecules with recently elucidated mechanisms of action. In Chapter 5, we derive and interpret several PK-related characteristics for simple, generic multi-compartment models under a multiple dose setting, and then use them as guiding tools for developing our framework to understand different measures of drug accumulation and half-lifes. We also explore the impact of PK on the antiviral action of drugs used in HIV therapy. In Chapter 6, we discuss the challenges in parameter identifiability in viral dynamic models and investigate techniques that aim at addressing these concerns. Finally, in Chapter 7, we conclude with a summary and outlook.

Chapter 2

Biological background and mathematical models of HIV infection and therapy

This chapter briefly reviews some aspects of the biology of human immunodeficiency virus (HIV) and different mathematical approaches that have been developed to model HIV infection and therapy. We begin by discussing the pathology and epidemiology of acquired immunodeficiency syndrome (AIDS) caused by HIV infection. Then, we present key features of the viral life cycle, before elucidating methods of HIV therapy and the various challenges therein. Subsequently, we describe mechanistic and statistical modelling approaches that have enabled a quantitative understanding of various phenomena concerned with HIV infection and therapy.

2.1 HIV and AIDS: pathology and epidemiology

HIV is a lentivirus of the *Retroviridae* family. Its primary targets are the cells of the human immune system, such as the cluster-differentiated $(CD4)^+$ T-cells, macrophages and dendritic cells. HIV infection leads to a gradual loss of cell-mediated immunity and exposes the body to a slew of opportunistic infections [16]. The first clinical occurrence of HIV was reported in 1981 in the United States (see Chapter 169 of [17]), with patients succumbing to mainly opportunistic infections such as pneumocystosis and Kaposi's sarcoma. These infections were generally known to occur in immuno-compromised individuals, and thus led investigators to speculate on the targets and mechanisms of HIV infection. It was from 1982 that the Center for Disease Control in the United States of America started referring to the disease caused by HIV infection as AIDS. Considered to be the first post-modern pandemic [18], AIDS has caused an estimated 36 million deaths worldwide, and up to 35.3 million people are currently living with HIV, with about 10% of them being children [19]. Additionally, the disease has taken its toll on the economy, education and demographics of countries across the globe [20].

2.1.1 HIV infection and the course of AIDS

The $CD4^+$ T-cell count is the primary clinical marker associated with the pathology of HIV infection. A $CD4^+$T-cell count below 200 per μL of blood in a HIV-infected individual is taken to imply a diagnosis of AIDS [22]. The main routes of transmission of the virus are sexual contact, contact with infected body fluids and vertical mother-to-child transmission during pregnancy, delivery or breast-feeding [23–25].

In general, the disease progression subsequent to HIV infection (Figure 2.1) is divided into an acute phase, a chronic pase and a final phase (see [26], for example). Upon

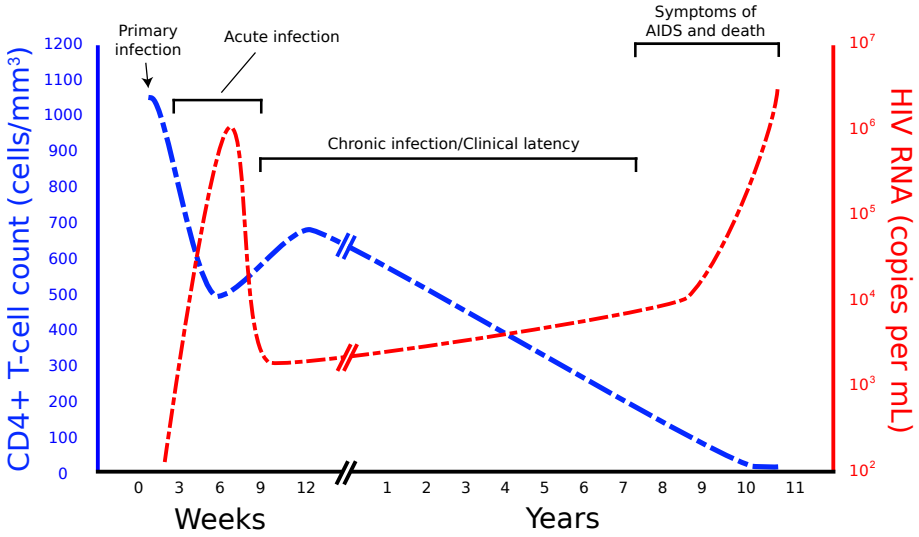

Figure 2.1. The different phases in HIV infection. After an initial acute phase, chronic infection sets in, which gradually progresses to AIDS. Figure modified from [21] and used here for illustrative purposes.

infection, the virus can be detected in the early stages in local lymph nodes [27]. The acute phase of infection has been characterized as the transient, symptomatic illness associated with a high-titre viral replication [28]. However, the detection of disease during the acute phase, referred to as 'closing the window' [29], is a diagnostically challenging task. In the few days after establishing infection in lymph nodes, the virus rapidly travels to other tissues such as the gut-associated lymphoid tissue and attacks the T-cells, resulting in peak viremia, inevitably followed by a massive destruction of T-cells [30]. After this initial onslaught on the immune system, the infection settles down to a long, chronic phase characterized by a gradual decline in T-cell levels. The viral load increases very gradually during this phase. However, the fluctuations are small, relative to the early phase. This phase is marked by its innocuous nature, as the apparent sluggishness in the dynamics of the virus conceals an underlying rapid turn-over [31]. In fact, this interesting observation marked the beginning of modelling host-virus dynamics (see Section 2.4). The final phase of infection marks the progression to AIDS and is accompanied by a severe loss in immune function, making the patient susceptible to numerous opportunistic infections ranging from candidiasis to carcinomas [32].

2.1.2 Immune response

The virus initially establishes infection by penetrating through the genital mucosal layers, and this, by itself, is a remarkably complex process [33]. The initial days of infection see an increase in the levels of acute-phase proteins like serum amyloid A and cytokines like interleukin (IL)-15, IL-18 and tumour necrosis factors (TNF) [34]. Natural killer (NK) and natural killer T (NKT)-cells are also involved in this acute phase of infection [35]. HIV modulates the expression of ligands that are necessary to trigger NK-cell cytotoxic responses [36]. This, along with other evidence led investigators to ascertain the involvement of NK and NKT cells in the immune response mounted against the virus. All these

host cellular responses, in general, have antiviral roles. Subsequent to peak viremia and during the decline of the viral load to the viral set-point (which is the viral load level during chronic infection phase), the $CD8^+$ T-cell responses manifest strongly [37]. A significant event during this phase is the change in the viral founder sequence and the subsequent selection of mutants [38]. The T-cell mediated immune responses are collectively termed cytotoxic T-lymphocyte (CTL) responses and these exhibit antiviral effects by lysis, apoptosis of infected cells or IL-mediated impeding of viral replication. The CTL responses to the viruses are believed to be the strongest form of defense by the host [39]. However, they focus only on specific epitopes and this has enabled the virus to develop mechanisms to evade them. Other intracellular immune responses involve host cellular proteins such as APOBEC3G that reduce viral replication [40], and host-mediated clearance of viral mRNA and proteins (see [41] for a review).

2.1.3 HIV subtypes and diversity

The genetic variability of HIV has been well-known since 1986, when it was observed in some West-African patients, that AIDS was caused by a strain morphologically similar to, but antigenically different from viruses that had been isolated earlier [42].

There are two major HIV strains currently recognized, namely HIV-1 and HIV-2 [44].

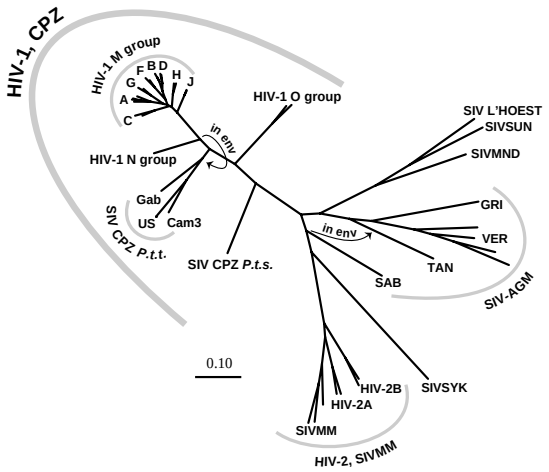

Figure 2.2. Phylogeny of HIV and SIV. A phylogenetic tree showing the origins of HIV-1 and HIV-2 strains and the various groups therein. The graphic is adapted from [43].

HIV-1 is known to have had its origins in a certain simian immunodeficiency virus (SIV) lineage *SIVcpzPtt* [45] that is observed in chimpanzees, while a sootey mangabey lineage *SIVsmm* has been demonstrated to be the origin for HIV-2 [46] (Figure 2.2). HIV-1 is the more prevalent of the two forms with HIV-2 being restricted mainly to Africa. HIV-2 is also known to be less pathogenic causing lower average viral loads and having lower rates of transmission [47]. Interestingly, it is also possible that a single individual can be infected with both HIV-1 and HIV-2 [48]. This is referred to as a super-infection. Such diversity in viral strains raise pertinent questions on the relevance of existing treatment strategies that are largely devised for HIV-1. It is now recognized that resistance acquisition and

thereby, the selection of second-line treatment regimens depends on the subtype [49].

Phylogenetically, HIV-1 is further grouped into four groups—M, N, O and P. The group M (for major) is the most common and accounts for about 90% of infections globally. The M group is again further classified into sub-types that are each denoted by a letter (A, B, C, ...). The HIV-1B is the dominant sub-type found in Western Europe and North America. Resistance patterns and phenotypic attributes are known to vary amongst the sub-types, necessitating further studies [50].

2.1.4 Epidemiology of AIDS

AIDS is classified as a pandemic disease [51]. The World Health Organization (WHO) regards a pandemic to be a global outbreak (Figure 2.3), with the spread of a disease-causing agent. According to the report of the UNAIDS committee in 2012, 68% of infections occur in sub-Saharan Africa, making it the worst-affected region [52]. The report places a prevalence of 0.35% in east and south-east Asia, and owing to the highly dense population in many countries of this region, it has the most infected individuals after sub-Saharan Africa. North America has about 1.3 million infected individuals, while Western and Central Europe account for close to 0.8 million patients. Amongst recent worrisome trends, is a rise in incidence of AIDS in a few high-income countries [53]. Quantifying the spread of the pandemic is a non-trivial task and there have been challenges in developing appropriate measures of the spread of AIDS [54].

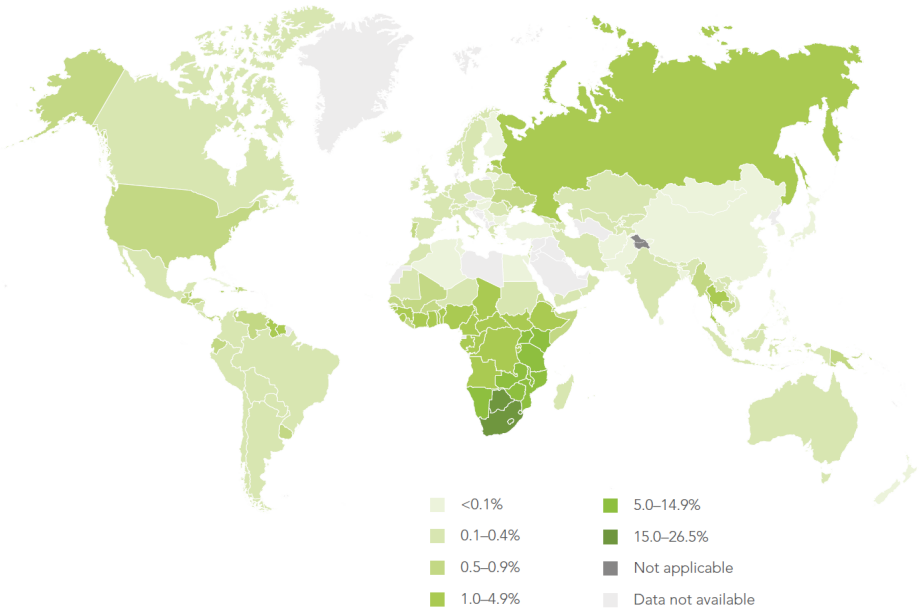

Figure 2.3. Global prevalence of HIV. A map depicting the global occurrence of AIDS. The darker regions have a higher prevalence. The graphic is adapted from the Global report: UNAIDS report on the global AIDS epidemic 2012 [52].

In summary, HIV infection is a complex and highly dynamic process that results in a gradual progression to AIDS. The myriad immune responses mounted by the host are insufficient to check viral proliferation. Phylogenetically, there are different HIV groups and sub-types that compound problems in treatment. Although anti-HIV therapy (see

section 2.3) has served to limit the disease, the global numbers are rising and challenges in combating disease transmission lie ahead.

2.2 HIV-1 Infection cycle

Morphologically, HIV is roughly spherically shaped with a diameter of about 120 nm [55]. See [16], for example, for details on cellular and molecular aspects of the virus. Here, we outline some key characteristics. The virus consists of two copies of positive, single-stranded ribonucleic acid (RNA), that encode for nine genes *gag, pol, env, tat, rev, nef, vif, vpr and vpu*. The viral RNA is enclosed within a protein capsid. The *gag* gene codes for a pre-cursor Gag polyprotein that is later processed by the viral protease to form products such as the viral matrix and capsid proteins, while *pol* is a gene coding for three key proteins of the viral machinery—the reverse transcriptase, integrase and HIV protease. The entry and binding mechanisms of the virus are mainly controlled by the surface lipoproteins Gp120 and Gp41 that are encoded by *env*. The *tat* and *rev* genes encode for proteins that play important roles in the reverse transcription and protein synthesis of HIV. The *nef, vif, vpr* and *vpu* parts of the genome encode for accessory regulatory protein products responsible for successful release and infectivity of new virions.

The replication cycle of HIV begins with the entry, binding and fusion of the virus to target cells in the human immune system, followed by reverse transcription of the viral RNA, the integration of the resulting viral DNA into the host genome, the synthesis of viral proteins and finally culminates in the assembly and release of new, mature virions. An understanding of the viral life cycle forms the basis for the design of various drugs targeting different stages in the viral life cycle. The replication cycle is also centrally involved in mathematical models describing within-host viral dynamics of HIV. Hence, we briefly review these various stages in the replication cycle of HIV.

2.2.1 Entry and fusion of the virus

The Gp120 and Gp41 proteins encoded by the *env* gene of HIV are responsible for coordinating the sequence of events leading to the entry, binding and fusion of the virus with the target cells of the human immune system. The initial binding of the virus with the CD4 receptor induces conformational changes in the Gp120 moiety, that is thought to facilitate the engagement of co-receptors (Figure 2.4). Two very important co-receptors are the C-C chemokine receptor type-5 (CCR5) and C-X-C chemokine receptor type-4 (CXCR4).

Upon binding of the Gp120 to these co-receptors, the Gp41 moiety is oriented parallel to the viral and cellular membranes and a fusion-pore formation is induced by a *cast-and-fold* mechanism [57] and finally virus internalization occurs. See [58] for a detailed review of the cascade of events leading to the entry and fusion of HIV.

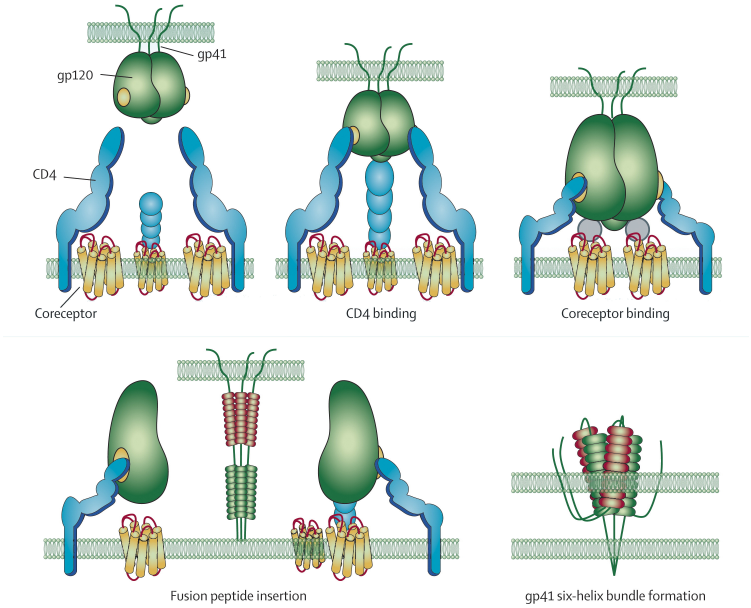

Figure 2.4. Entry cascade in HIV. The sequence of events leading to the binding, entry and fusion of HIV with a target cell. Figure adapted from [56] and used here for purposes of illustration.

Reverse transcription of viral RNA and integration of viral DNA

The reverse transcriptase of HIV is a key enzyme responsible for generating a complementary DNA (cDNA) sequence from the viral RNA. This process is termed reverse transcription, since it can be perceived as a counter-role of the conventional transcription process—synthesis of messenger RNA from DNA, that forms part of the central dogma of molecular biology. Howard Temin and David Baltimore were joint recipients of the Nobel Prize for Physiology and Medicine in 1975 for their discovery of the reverse transcription in viruses (see [59] for a joint chapter by Temin and Baltimore on RNA-directed DNA synthesis in viruses).

A cellular transfer-RNA (tRNA) initiates the process of reverse transcription by binding to a primer-binding site on the viral RNA. The reverse transcriptase then copies the long terminal region (LTR) of the RNA into a single stranded DNA. The RNase H part of the RT enzyme degrades the RNA that has been copied. This enables the tRNA, RT and the single stranded DNA fragment to move on to the other LTR end. The RNase thus serves to eliminate the RNA fragments that have been copied and facilitates propagation of the copying mechanism. A second strand of DNA is later generated that loops around the first strand to form circular DNA, which is then clipped in the final stages, to yield double stranded DNA. See [60] for a review of the reverse transcription process.

The process of reverse transcription is error-prone in the sense that misincorporation of base pairs is highly common and the fidelity of the reverse transcriptase enzyme has been a subject of investigation since the late 1980s [61]. The *in vivo* mutation rates of HIV are higher than several other viruses, with an average of about 3.4×10^{-5} mutations per base pair per cycle of replication [62]. Upon completion of reverse transcription, the synthesized DNA binds to a few viral and host cell proteins, forming a pre-integration

complex (PIC). The formation, composition and kinetic features of PIC have also been characterized [63].

The integration of the viral DNA into the host genome is performed by the integrase enzyme. First, the enzyme prepares the viral DNA by processing the 3'-end of the LTR. This is followed by the transport of the PIC across the nuclear membrane into the nucleus, where integrase cleaves the host DNA at preferred sites to create ligation openings for the viral DNA [64]. After ligation, DNA repair mechanisms operate to 'close gaps' in the DNA.

Once the viral DNA has been integrated into the host genome, it is free to exploit the host cellular machinery for transcription and translation processes. The LTR region, along with Tat and Rev proteins, again plays a pivotal role in transcription of viral DNA. Interestingly, the basal transcriptional activity of the LTR region is low. However, in the presence of Tat, transcription proceeds much faster [65]. This mechanism of transcriptional control by Tat has generated interest, particularly after it became known that positive transcription elongation factor b (P-TEFb) comprising of cyclin dependent kinase-9 (CDK-9) and cyclin T1 plays a crucial role [66]. Tat binds to P-TEFb and this forms a complex with nascent transcripts of the trans-activation response element (TAR) region of HIV. CDKs are traditional targets in oncology [67] and this led to studies that investigated the role of CDK inhibitors as antivirals (see Section 2.3.4). Some promising results have been obtained [68, 69], but one is yet to see clinical applications.

Subsequent to integration, the infected cell can also enter into latency, whereby post-integration events are suppressed and the cell goes into hibernation. There are different explanations for such behaviour including a defective Tat protein that lowers transcription rates [70], a poorly functioning Rev that hinders export of transcribed RNA into the cytoplasm for further processing [71] and restrictive chromatin structures being formed in the LTR region [72].

2.2.2 Viral protein assembly and maturation

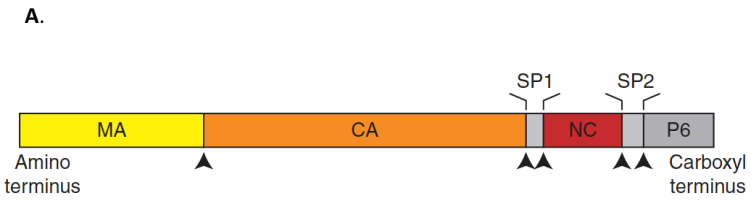

After transcription of viral DNA and translation of viral mRNA, the process of assembling the proteins (Figure 2.5) and eventual maturation and release of new viral particles begins. This is an extremely intricate sequence of events and we give only brief details. See [73] for example, for a review on HIV protein assembly and maturation processes. The viral protein assembly occurs at the plasma membrane of the host cell within specialized microdomains. The Gag polyprotein coordinates all events leading to the assembly and maturation of viral particles. At the amino-terminal of this polyprotein is the MA (matrix) domain that controls proper targeting and binding of Gag to the plasma membrane and engagement of the Env protein (Figure 2.5A). The central CA (capsid) domain regulates

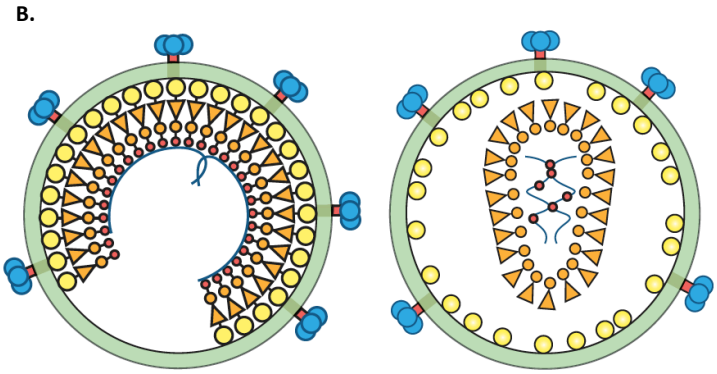

Figure 2.5. The *Gag* polyprotein and maturation of viral particles. Top: The different domains of the *Gag* polyprotein. **Bottom:** The organization of proteins within an immature (left) and mature (right) virus particle. Figure reproduced from [73] for purposes of illustration.

protein-protein binding during maturation in immature viral particles and triggers multimerization. The NC (nuceleocapsid) domain serves as a chaperoning agent facilitating tRNA priming at the start of reverse transcription and is also responsible for packaging of viral RNA. The carboxy domain of Gag mainly contains binding sites for viral accessory proteins. The viral protease catalyzes its own cleavage, as well as cleavage of other enzymes from the Gag polyprotein. Recently, a full kinetic model has been developed to study events during assembly and maturation events [74]. For budding, the virus makes extensive use of host-cell machinery.

2.3 HIV therapy

Equipped with the knowledge of the viral replication cycle, we now discuss the different HIV therapeutic strategies.

2.3.1 History of antiretroviral treatment

The treatment of AIDS has a long history. In 1987, zidovudine (ZDV), became the first antiretroviral drug to be developed [75]. It targeted the reverse transcription process in the replication cycle of HIV. Almost foreshadowing the immense challenges ahead, high-level resistance development against zidovudine with the acquisition of multiple mutations was described as early as 1989 [76]. More drugs with similar mechanisms were developed until 1995, with some success.

In 1995, there was a huge leap forward and much promise appeared to lie in store with the advent of HIV protease inhibitors —saquinavir being the first such drug to be approved [78]. More drugs like ritonavir and nelfinavir followed in 1996, but the hopes from this family of drugs were belied to a certain extent, when resistance was detected soon [79, 80]. The first decade of the new millenium saw the development and approval of three drugs from novel drug classes. While enfuvirtide was the first anti-HIV drug targeting the viral fusion with the host cell to be approved in 2002, maraviroc was the first drug inhibiting the entry of HIV into host cells, to be approved in 2006. In 2007,

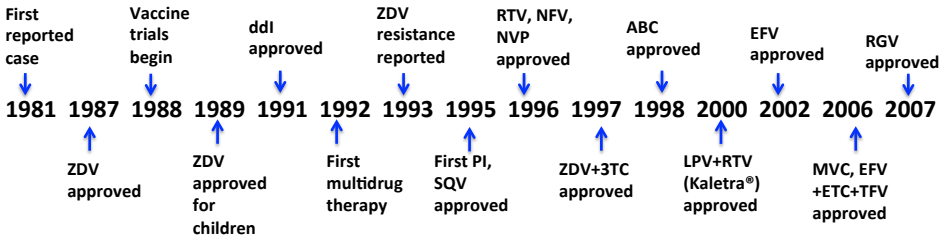

Figure 2.6. A timeline of antiretroviral therapy. The development of different anti-HIV drugs beginning in the 1980s continuing into the recent years. Adapted from [77].

raltegravir became the first drug inhibiting integration of HIV DNA with the host genome, to be approved. In the following sub-section, we discuss these drug classes in more detail.

2.3.2 Major antiviral drug classes

The major anti-HIV drugs can be classified under different drug classes on the basis of their targets and mechanism of action (see Figure 2.7).

Entry inhibitors: These bind to receptors or co-receptors on the target cells, thereby preventing the virus from recruiting them. Maraviroc (MVC) is an approved entry inhibitor, that is a negative allosteric modulator of the CCR5 receptor [81]. It binds to the CCR5 receptor and hence Gp120 does not effectively trigger the entry process. However, the long-term safety of CCR5 blockage and escape mechanisms of HIV by recruitment of other receptors are some concerns [82].

Fusion inhibitors: They interfere with the ability of HIV to fuse with the target cell and release viral contents. Enfuvirtide (EFV) is a peptide drug that acts as a fusion inhibitor [83]. It binds to Gp41 and prevents HIV from infecting the cell. Its inconvenient administration via a sub-cutaneous injection is a drawback [84].

Reverse transcriptase inhibitors: As their name indicates, these drugs disrupt the reverse transcription process during viral replication. This was the mechanism of the earliest introduced anti-HIV drugs. Drugs of this class may be further classified into nucleoside reverse transcriptase inhibitors (NRTIs) and non-nucleoside reverse transcriptase inhibitors (NNRTIs). In general, the NRTIs are pro-drugs that are phosphorylated by cellular kinases and then incorporated into the viral DNA during reverse transcription, since they are analogs of natural nucleosides. This halts the reverse transcription process by chain termination. Zidovudine (ZDV), lamivudine (3TC), didanosine (ddI), emtricitabine (ETC), abacavir (ABC), and tenofovir (TFV) are some of the common NRTI drugs. On the other hand, NNRTIs inhibit the activity of the reverse transcriptase enzyme by binding to an allosteric site. Efavirenz (EFV) and nevirapine (NVP) are two common NNRTIs. See [85] for a detailed survey of reverse transcriptase inhibitors in HIV therapy. Mitochondrial toxicity induced by NRTIs and related lipodystrophy [86], and heptotoxicity by NNRTIs such as nevirapine [87] are a few adverse effects of concern.

Integrase inhibitors: These target the viral integrase enzyme that is responsible for integrating the reverse transcribed viral DNA into the host genome. Raltegravir (RGV) [89] was the first integrase inhibitor (InI) to be approved. Recently, two other drugs of this class have been approved—elvitegravir (EVG) [90] and dolutegravir (DTG) [91].

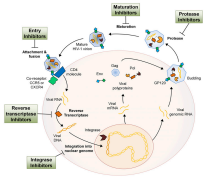

Figure 2.7. HIV drug classes. The action of the different drug classes at different stages in the HIV replication cycle. The graphic is reproduced from [88] for purposes of illustration.

Integrase inhibitors appear to be well-tolerated, although long-term safety data is scarce.

Protease inhibitors: These are amongst the most potent drugs for HIV monotherapy. They target the HIV protease and inhibit successful protein assembly and release of new viral particles. Recently, their mechanism has been debated and a multi-step inhibition has been proposed [92]. Indinavir (IDV), lopinavir (LPV), ritonavir (RTV), nelfinavir (NFV) and saquinavir (SQV) are some examples of HIV protease inhibitors (PI). RTV is commonly used to boost the pharmacokinetics of other drugs in a treatment regimen as it inhibits enzymes responsible for metabolism of many other protease inhibitors [93]. Risks of elevated triglycerides and myocardial infarction have been reported [94].

Maturation inhibitors: These bind to the viral Gag protein and result in immature virions being released that are incapable of further infection [95]. There are no approved maturation inhibitors currently. Clinical trials with bevirimat were discontinued in 2010 owing to unsatisfactory response in a significant number of patients.

2.3.3 The HAART regimen

Countering HIV infection by a combination of drugs, rather than a single drug has been the norm since the mid 1990s. Gulick and colleagues published a series of studies with IDV-based combination regimens [96, 97]. In 1996, Hammer et al [98] studied the efficacy of monotherapy versus dual therapy for nucleoside inhibitors zidovudine, didanosine and zalcitabine. Such use of multiple drugs to combat HIV infection and AIDS is termed highly active antiretroviral therapy (HAART). In present times, first-line HAART regimens recommended for treatment naïve patients usually consists of two NRTIs and an InI. The recommended NRTI backbone consists of the drugs TFV and ETC, and the recommended first-line InIs are RGV or DTG. In some instances, the InIs may be replaced by RTV-boosted PIs. Currently, HAART cannot achieve eradication of HIV, primarily due to the phenomenon of long-lived infection resulting from latently infected pools of target cells. However, sustained viral suppression and recovery in $CD4^+$ T-cell counts have been reported in studies involving large patient cohorts [99, 100].

2.3.4 Host-cell targeting, error catastrophe and vaccines

It is clear that HIV recruits host proteins at several points during its replication cycle. This has triggered efforts in development of drug agents that target these host-proteins, rather than the virus. For example, CCR5 antagonists like MRV have proven to be effective in suppressing HIV replication [101]. Bioinformatic approaches like high-throughput genome-

scale screens based on RNA interference have been used to identify host factors that are attractive targets [102].

Another novel family of host targets are the cyclin dependent kinases (CDKs). Traditionally investigated in oncology, the antiviral effects of CDK inhibitors have generated considerable interest. Flavopiridol, a CDK9 inhibitor that is in clinical trials for the treatment of chronic lymphocytic leukemia, was shown to possess antiviral properties [103]. It inhibits transcription by RNA Polymerase II by blocking the elongation step. This is controlled by the protein P-TEFb (CDK9 + Cyc T1). Notably, lower concentrations of flavopiridol were needed for antiviral activity, as opposed to its role as an anti-cancer drug. Roscovitine, another drug in clinical trials for non-small cell lung cancer and leukemia has also demonstrated antiviral properties [69].

Vaccines have proven to be effective against numerous viral infections ranging from influenza to small pox. The development of a vaccine against HIV would provide enormous thrust in the battle against AIDS and in offering a potential cure. However, there are immense challenges to be overcome. To start with, the development of a vaccine against HIV encounters its first hurdle in meeting a fundamental tenet of vaccinology - to mimic the infection and introduce responses similar to natural immunity. The natural immune response against HIV infection is too weak to be useful [104]. Secondly, the epitopes of the viral envelope are highly variable, in addition to HIV isolates themselves differing in their sub-types and groups. High throughput screening of B-cell clones from infected patients for broadly neutralizing antibodies [105], together with recent attempts at a rational vaccine design [106] offer some possibilities. In 2012, a combination regimen of ETC and TFV was approved by the Food and Drug Administration (FDA) as a preventive measure for high risk populations [107]. There have been several clinical trials to explore the success of different candidates. For example, the STEP study tested the possibility of inducing cell-mediated immune responses to injected adenovirus-based HIV vaccines and did not entirely succeed [108]. Worryingly, it also raised questions of higher risks amongst vaccinated patients [109]. Some researchers hold the view that more fundamental advances in understanding HIV biology are needed before anti-HIV vaccine efforts can bear fruit [110].

2.4 Mechanistic models of HIV infection and treatment

The initial motivation for development of models describing viral dynamics within the host lay in attempts to explain viral load measurements in patients chronically infected with HIV. In a seminal article that established the relevance of measuring viral load and forecasted its crucial role in monitoring HIV disease progression, Ho et al [31] used simple mechanistic arguments to propose a dynamic equilibrium between the production and clearance of virions. This balance in the dynamics results in a viral set-point that characterizes infection in a patient. While the viral set-points themselves remained almost constant in time in patients with chronic disease, the onset of antiretroviral treatment caused a significant drop ($\sim$2 orders of magnitude in about 2 weeks) in the viral load [111]. Such a behaviour on perturbation by drugs suggested a rapid viral turn-over and pointed

to a frenzied underlying dynamics, in spite of almost constant viral loads during disease progression. Mathematical models of infection dynamics, thus, had their origins in this need to investigate the rates of viral production and decay, and their significance in disease progression and drug action.

2.4.1 Basic models of viral dynamics

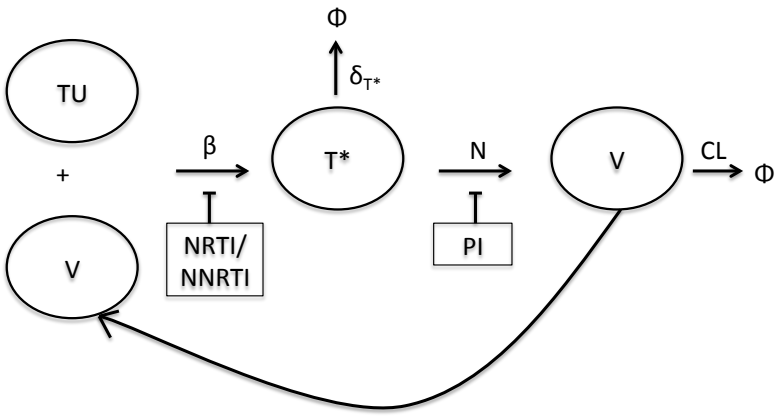

Figure 2.8. A basic viral dynamics model. A single-stage infection model to describe viral dynamics.

Early models of viral dynamics [111–115] sought to explain the rates of decay in viral load upon antiretroviral treatment. For illustration, we describe one such model [114] (Figure 2.8).

Uninfected target cells TU are infected by viruses V with a reaction rate constant of β resulting in an infected-cell population T^*. These productively-infected cells can then release new viruses with a rate constant N, which are either cleared with a rate constant CL or re-infect the uninfected target cells, thereby propagating the cycle. The infected-cells T^* die at a constant rate, with the correponding rate constant specified by δ_{T^*}. Uninfected target cells are synthesized and degraded with rate constants λ_{TU} and δ_{TU} respectively. Such models are generically classified as one-stage viral infection models as they include a single stage of infected-cells in their scheme. The ordinary differential equation (ODE) description of such a model can be written as

$$\begin{aligned}
\frac{\mathrm{d}}{\mathrm{dt}}\mathrm{TU} &= \lambda_{\mathrm{TU}} - \delta_{\mathrm{TU}} - \beta \cdot \mathrm{V} \cdot \mathrm{TU} \\
\frac{\mathrm{d}}{\mathrm{dt}}\mathrm{T}^* &= \beta \cdot \mathrm{V} \cdot \mathrm{TU} - \delta_{\mathrm{T}^*} \cdot \mathrm{T}^* \\
\frac{\mathrm{d}}{\mathrm{dt}}\mathrm{V} &= N \cdot \mathrm{T}^* - \mathrm{CL} \cdot \mathrm{V} - \beta \cdot \mathrm{V} \cdot \mathrm{TU}
\end{aligned} \tag{2.1}$$

The action of drugs is incorporated by inhibiting the appropriate reaction rate constants in the model. For example, in the presence of a protease inhibitor, the production of new viruses is blocked. A drug that blocks viral protease production by 100% would imply $N = 0$. The parameters δ_{T^*} and CL are estimated from viral load measurements after administering a protease inhibitor [114]. In reality, drugs are not 100% effective and

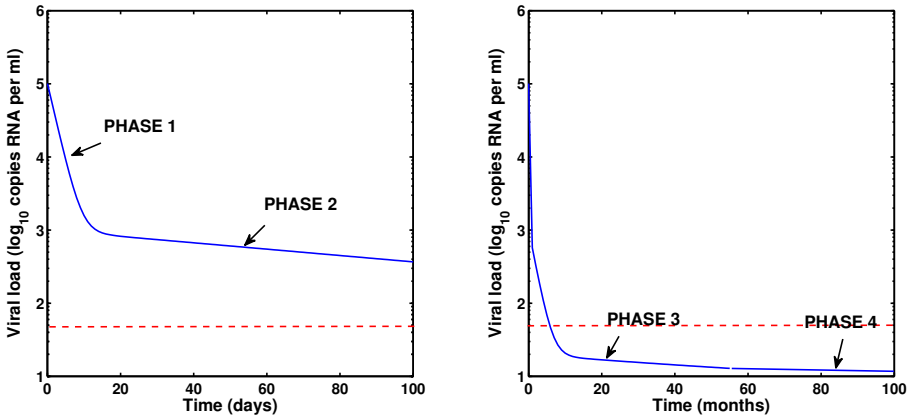

Figure 2.9. Phases of viral decay. The different phases of viral decay upon antiretroviral therapy. The first two phases occur over a time scale of weeks, while the third phase occurs over months. A final fourth phase is also observed over years. Figure adapted from [116].

to model drug-effect more explicitly, models motivated from pharmacodynamics can be used (see Section 2.4.3). The action of a reverse transcriptase inhibitor can be modelled by lowering the infection reaction rate constant β.

Note that this model assumes a reservoir of uninfected target cells that remains constant during the course of infection. To be more realistic, later models included a density dependent synthesis mechanism and a death process for the target cells [5, 117]. For example,

$$\frac{\mathrm{d}}{\mathrm{dt}}\mathrm{TU} \quad = \quad \lambda_{\max} \cdot \mathrm{TU} \cdot \left(1 - \frac{\mathrm{TU}}{\mathrm{TU}_{\max}}\right) - \delta_{\mathrm{TU}} \cdot \mathrm{TU} - \beta \cdot \mathrm{V} \cdot \mathrm{TU} \tag{2.2}$$

where, $\lambda_{\max}$ is the maximum proliferation rate of the target cells and $\mathrm{TU}_{\max}$.

When more than one drug is used in a treatment regimen, the initial drop in the viral load is much higher and a second phase of viral decay (see Figure 2.9 left) can be observed experimentally. To account for this, a second pool of target cells MU was postulated [115], that contributed to a longer-lived population of infected-target cells M^*. Biological candidates for such a pool were postulated to be the macrophages, dendritic cells or other such viral reservoirs. Additionally, to incorporate the existence of a latent reservoir of infection attributed to resting $\mathrm{CD4}^+$ memory T-cells and explain further phases of viral decay (see Figure 2.9 right), models have included a pool of latently infected cells, which can be re-activated to productively infected-cells [118–120]. With the development of new drug classes, the need for more detailed models capturing other stages in the viral cycle was imperative to assess the differences between various drugs, their modes of action and reasons for their success or failure.

2.4.2 Two-stage viral dynamics model

In the early days following the development of the integrase inhibitor raltegravir, a puzzling discrepancy was noted between its *in vitro* efficacy measured by phenotypic single-round infectivity assays and *in vivo* efficacy assessed by viral load measurements [121]. Sedgahat et al [6] used mathematical models to infer that the high apparent *in vivo* efficacy of integrase inhibitors was owing to the stage inhibited in the viral life cycle and not due to any innate superior efficacies of these drugs. A detailed mechanistic model of the viral life cycle [7] revealed more details on the how the nature of the step inhibited in the viral life cycle plays an important role in efficacy assessments and suggested a single measure termed the reproductive capacity to translate *in vitro* efficacy measures into an *in vivo* context. The authors in [7] also performed a model-reduction of their detailed model to enable an easier parametrization and were able to validate their model with clinical viral load data. This reduced model has also been extended to include latently infected T-cells [122]. Here, we briefly discuss the features of this two-stage viral dynamics model. Later in the thesis, we present a generalization of this model to incorporate drug-specific mutation schemes (Chapter 3).

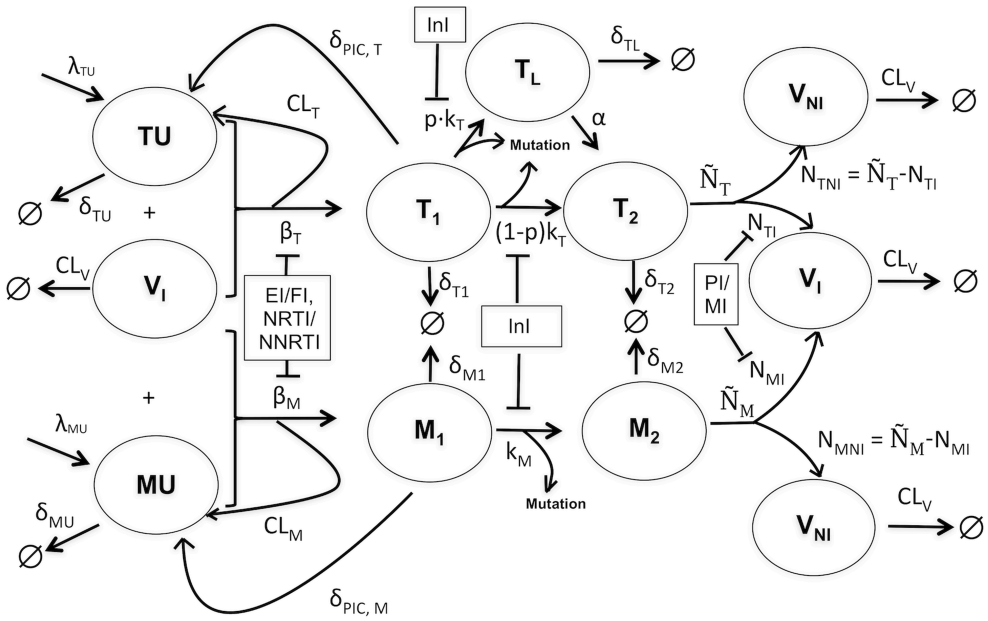

Figure 2.10. A two-stage viral dynamics model. A within-host model of viral infection that allows for incorporation of all approved anti-HIV drug classes: EI/FI - entry/fusion inhibitors, NRTI/NNRTI - nucleoside/non-nucleoside reverse transcriptase inhibitors, InI - integrase inhibitors, PI/MI - protease/maturation inhibitors.

The model includes target cells TU (T-cells) and MU (macrophages), that can be infected by infective viruses V_I (with effective infection reaction rate constants β_T and β_M), resulting in early stage infected cells T_1 and M_1, respectively. Infection can potentially be unsuccessful after fusion of the virus, rendering the cell uninfected and thereby eliminating the virus (CL_T, CL_M). The infected T_1 and M_1 cells can also possibly return to uninfected states by destruction of essential viral proteins or DNA prior to integration ($\delta_{PIC,T}, \delta_{PIC,M}$). The T_1 cells can enter into a latent state T_L (with a probability p) that

can get re-activated with a rate constant α. Integration of viral DNA in the host genome proceeds with a rate constant of k_T in the T-cells and k_M in the macrophages, resulting in late stage infected T-cells T_2 and macrophages M_2, respectively. The infected T_2 cells release new infective (V_I) and non-infective (V_{NI}) viruses (with rate constants N_{TI} and N_{TNI}, respectively) while the infected M_2 cells release new infective and non-infective viruses (with rate constants N_{MI} and N_{MNI}, respectively). Target cells TU and MU are produced by the immune system at constant rates with reaction rate constants λ_{TU} and λ_{MU}, respectively. All of TU, MU, T_1, M_1, T_2 and M_2 can be cleared by the immune system with rate constants δ_{TU}, δ_{MU}, δ_{T1}, δ_{M1}, δ_{T2} and δ_{M2}, respectively. Viruses are cleared by the immune system with rate constant CL_V. The system of ODEs describing the model is given by:

$$\begin{aligned}
\frac{d}{dt}TU &= \lambda_{TU} - \delta_{TU} \cdot TU + \delta_{PIC,T} \cdot T_1 - \beta_T \cdot V_I \cdot TU \\
\frac{d}{dt}MU &= \lambda_{MU} - \delta_{MU} \cdot MU + \delta_{PIC,M} \cdot M_1 - \beta_M \cdot V_I \cdot MU \\
\frac{d}{dt}T_1 &= \beta_T \cdot V_I \cdot TU - \big(\delta_{T1} + \delta_{PIC,T} + k_T\big) \cdot T_1 \\
\frac{d}{dt}M_1 &= \beta_M \cdot V_I \cdot MU - \big(\delta_{M1} + \delta_{PIC,M} + k_M\big) \cdot M_1 \\
\frac{d}{dt}T_2 &= (1-p) \cdot k_T \cdot T_1 + \alpha \cdot T_L - \delta_{T2} \cdot T_2 \\
\frac{d}{dt}M_2 &= k_M \cdot M_1 - \delta_{M2} \cdot M_2 \\
\frac{d}{dt}T_L &= p \cdot k_T \cdot T_1 - \alpha \cdot T_L - \delta_{TL} \cdot T_L \\
\frac{d}{dt}V_I &= N_{TI} \cdot T_2 + N_{MI} \cdot M_2 - \Big[CL_V + \big(CL_T + \beta_T\big)TU + \\
&\qquad \big(CL_M + \beta_M\big)MU\Big] \cdot V_I \\
\frac{d}{dt}V_{NI} &= N_{TNI} \cdot T_2 + N_{MNI} \cdot M_2 - CL_V \cdot V_{NI}
\end{aligned} \tag{2.3}$$

A primary feature characterizing the behaviour of viruses, that has been missing in the description thus far, is the occurrence of mutations. Modelling mutations, their impact on resistance to different drugs and fitness characteristics is an integral component in predicting *in vivo* viral dynamics.

2.4.3 Modelling mutations, viral resistance and drug-action

Mutations in HIV occur to the absence of a proof-reading mechanism during reverse transcription (see Section 2.2.2). In the two-stage model, mutations are modelled to occur between early infected cells (first stage T_1 and M_1) and late infected cells (second stage T_2 and M_2). Consider two mutant viral genotypes g and g'. The probability $r_{g' \to g}$ of a mutation that changes the genotype from g' to g can be written as

$$r_{g' \to g} = \mu^h \cdot (1-\mu)^{L-h}, \tag{2.4}$$

where $h = h(g, g')$ is the Hamming distance between the genotypes g and g' (i.e., the number of positions at which the genotypes g and g' differ), L is the number of positions at which mutant genotypes are described, and μ is the probability of mutation per base-pair per cycle of replication. Since mutations are primarily a result of error-prone reverse transcription, both the forward and backward mutation processes are generally considered. For example, with mutations modelled at two loci, Figure 2.11 shows a simple mutational pathway with appropriate mutation rates between the different mutant genotypes. As mentioned earlier (Section 2.2.2), the average error rate in viral reverse transcription has been estimated to about about $\mu = 3.4 \cdot 10^{-5}$ mutations per nucleotide per cycle of replication. However, nucleotide-specific mutation rates have also been reported [123].

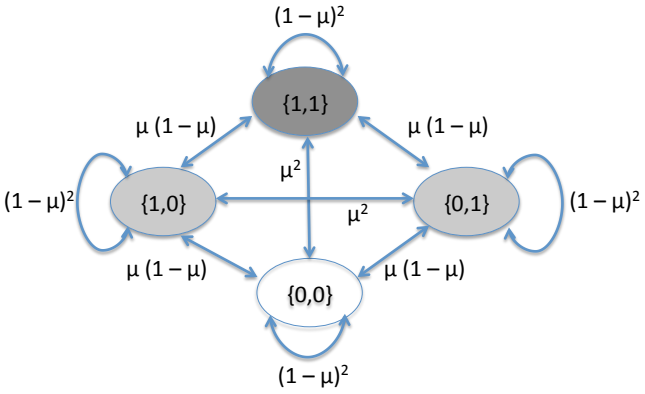

Figure 2.11. A simple mutation scheme. The mutation scheme models mutations at two loci. While {0,0} denotes the wild type, {1,1} denotes the mutant genotype with mutations at both loci. The mutants {0,1} and {1,0} are intermediate genotypes.

The effect of an antiretroviral drug on a viral genotype g can be modelled by a fractional reduction of the targeted process characterized by a drug efficacy parameter. For example,

$$\epsilon = \epsilon_g = \frac{C_{\text{drug}}/\text{IC50}_g}{1 + C_{\text{drug}}/\text{IC50}_g}, \tag{2.5}$$

where IC50_g denotes the drug concentration at which the fractional reduction is 50%. The subscript g indicates that the IC50-value and thus the drug efficacy is assumed to be genotype dependent (see below). Denoting by k_ϵ and k_0 the rate constants of the targeted process, in the presence and absence of the drug, respectively, drug action was modelled by

$$k_\epsilon = (1 - \epsilon)k_0. \tag{2.6}$$

As stated earlier, the two-stage model in [122] was derived from a more detailed viral infection model by model reduction (see [7] for details). As a consequence, the processes of infection of T-cells and macrophages (with rate constants β_T and β_M, respectively) and production of new infectious and non-infectious viruses from infected T-cells (with rate constants N_{TI} and N_{TNI}, respectively) and from infected macrophages (with rate constants N_{MI} and N_{MNI}, respectively) are lumped processes, integrating several subprocesses. For example, the infection process comprises the subprocesses of receptor binding, fusion and reverse transcription. Hence, the consequences of model reduction have to be taken into

account when modelling the actions of drugs targeting some of these subprocesses in the two-stage model, resulting in an additional model reduction factor γ_ϵ. For example, with RTIs and PIs, eq. (2.6) becomes

$$k_\epsilon = \big(1 - \gamma_\epsilon \epsilon\big) k_0 \quad \text{with} \quad \gamma_\epsilon = \frac{1-\rho}{1-\rho\epsilon}, \tag{2.7}$$

where ρ denotes the probability of successful reverse transcription (for RTIs) or the probability of successful viral maturation (for PIs). For more details on implementation of other drug classes, we refer to the Supplementary Text of [7].

The advantage of the decreased drug-susceptibility of a mutant genotype g is typically counter-balanced by a reduction in its fitness relative to the wild type [113]. This is usually quantified in terms of the fitness costs s_g (see Chapter 3 for details on fitness costs and fitness). In general, it can be assumed that a mutation in one part of the viral genome that is associated with a certain process of the viral replication cycle caused a drop in the rate of only this process. For example, a mutation in the reverse transcriptase part of the HIV-1 genome, resulting in a mutant genotype g, lowers only the rate of reverse transcription. This is a reasonable assumption at least for HIV-1 [124], as most resistance mutations occur in the region of the genome that codes for the drug target. Hence, any cost due to a resistance mutation is also most likely to be incurred on the function of this region.

The fitness costs and resistance factors of all mutant genotypes are parametrized with reference to the wild type. Denoting the rate constant of the targeted process in the wild type, in the absence of any drug, by $k_{\mathrm{wt},0}$, the rate constant of the targeted process in a genotype g with a drug efficacy ϵ_g, can be defined as

$$k_{g,\epsilon_g} = (1 - \gamma_{\epsilon_g}\epsilon_g) \cdot (1 - s_g) \cdot k_{\mathrm{wt},0}. \tag{2.8}$$

The first factor accounts for the reduction in activity due to drug action. The genotype-dependent drug efficacy ϵ_g is given by eq. (5.63), where

$$\mathrm{IC50}_g = \mathrm{RF}_g \cdot \mathrm{IC50}_{\mathrm{wt}} \tag{2.9}$$

is defined in terms of the wild type $\mathrm{IC50}_{\mathrm{wt}}$-value and the resistance factor $\mathrm{RF}_g \geq 1$ accounting for the increase in drug-resistance. The second factor in eq. (2.8) accounts for the reduction in activity due to loss in fitness of the mutant genotype.

2.5 Statistical models of mutation accumulation and viral resistance

In the last section, we discussed a few examples of mechanistic models that seek to describe viral dynamics. Such models have been of great utility in the investigation of drug-class effects and general features of antiretroviral therapy. However, the incorporation of realistic drug-specific mutation pathways in such models is needed to enable direct

comparisons with clinical data. In the current thesis, we combined drug-specific mutation models, learned statistically from clinical data, with mechanistic models to predict viral load profiles under monotherapy and combination therapy, and to estimate fitness characteristics of HIV mutant genotypes. In this section, we briefly review different statistical models of mutations and resistance.

The analysis of mutation accumulation in the HIV genome has relevance in several contexts. It enables the understanding of viral evolutionary pathways and mechanisms and thus aids in the choice of treatment regimens by anticipating future resistance development. Furthermore, statistical models predicting mutation accumulation have also led to estimates of phenotypic attributes like resistance and fitness. By learning from viral sequencing data, these methods accomplish a quantitative translation of genotyping results and enable more decisive treatment choices. There is a huge body of work in this regard, aiming at estimating mutational pathways of HIV [125–129], predicting viral phenotype from genotype data [8, 130, 131] and the prediction of treatment outcomes under different antiretroviral therapies [132–135]. Here, we briefly describe a few of these modelling approaches.

2.5.1 Mutagenetic trees

A mutagenetic tree is a directed tree (informally, a tree is a connected graph without cycles) whose vertices represent mutations, and edges denote mutational transitions between the connected vertices. Each edge has a conditional probability associated with it —the probability that a certain mutation occurs (until the time of data sampling by viral genotyping), given that its predecessor mutation has already occurred. For example, in the right most tree in Figure 2.12, the probability of mutation 210W occurring, given that 41L has already occurred is 0.40 (note the lack of an explicit time scale).

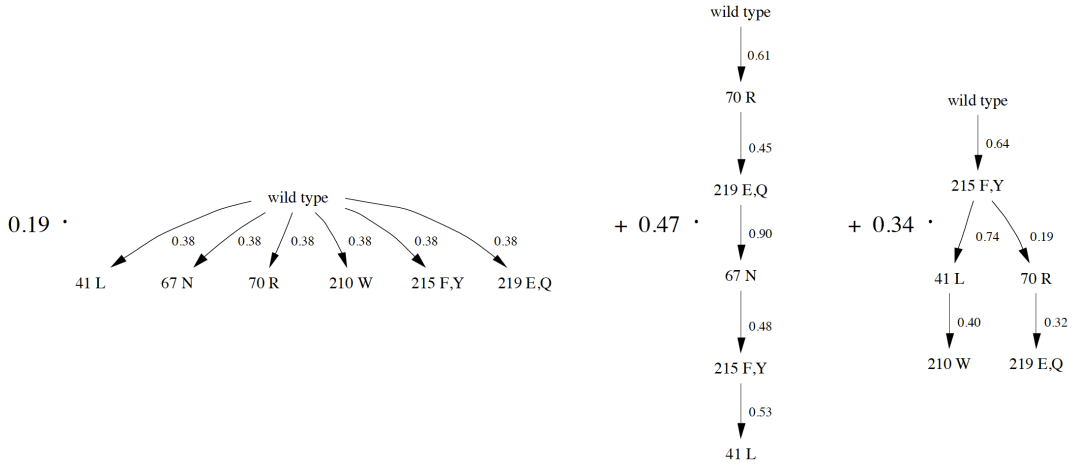

Figure 2.12. A mutagenetic tree. An example of a mutagenetic tree estimated from cross-sectional genotype data after zidovudine therapy. Figure reproduced from [136] for illustration.

Mutagenetic trees have been successfully used to model the accumulation of mutations under antiretroviral therapy and to compute probabilities of escape from treatment

regimens (commonly referred to as the genetic barrier) [126, 127]. Typically, the models are not single trees, but rather weighted combinations of disjoint trees, known as mixture mutagenetic trees. They are estimated by expectation-maximization (EM) algorithms, followed by appropriate model selection procedures. For example, Figure 2.12 shows an estimated mixture mutagenetic tree comprising of three weighted disjoint trees, that describes the accumulation of mutations under zidovudine therapy. See [126] and [136] for details on mutagenetic trees, their estimation and application.

2.5.2 Conjunctive Bayesian networks

Bayesian networks [137] are probabilistic-graphical models used widely in bioinformatics for the analysis of gene regulatory networks and gene expression [138]. A Bayesian network is a directed acyclic graph together with a joint probability distribution over a set of random variables $X = (x_1, ..., x_n)$. The vertices of the graph are the random variables x_i, while the edges reflect conditional dependencies between them. Mutagenetic trees are restrictive instances of Bayesian networks where the graph is a tree and this readily enables an evolutionary phlogenetic interpretation. We refer to [137] for a detailed treatment on Bayesian networks.

A conjunctive Bayesian network (CBN) [139] is a specialization of Bayesian networks specified by a set $\mathcal{E}$ of events, a partial order $\preceq$ on the events and parameters θ_e for each event e. The relation $e_1 \preceq e_2$ between events e_1 and e_2 indicates that e_1 has to occur before e_2. In this case, e_1 is also referred to as a parent of e_2. The parameter θ_e represents the conditional probability of event e occurring, given that all its parents have occurred.

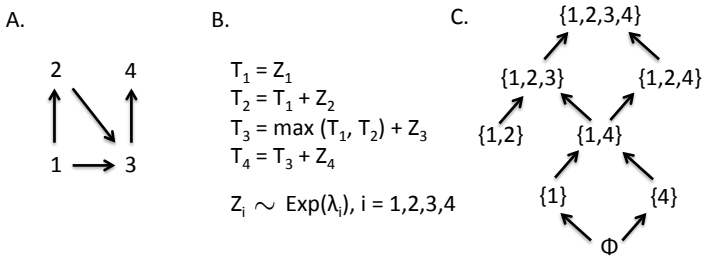

Figure 2.13. Continuous-time conjunctive Bayesian networks. (A) A poset of events 1, 2, 3 and 4, **(B)** Average statistical waiting times to the different events in **(A)**, and **(C)** The genotype lattice induced by **(A)**

Continuous-time analogues of the CBN, termed continuous-time conjunctive Bayesian networks (CT-CBNs) were introduced and used to model HIV mutational pathways [140]. These are more flexible than mutagenetic trees. See Figure 2.13 for an illustration. As their name indicates, they are generalizations of CBNs to a state space consisting of times of mutation events. A CT-CBN consists of a set $\mathcal{E}$ of events, a partial order $\preceq$ and rates of fixation λ_e of each event $e \in \mathcal{E}$. The data needed for estimation of such a model would include the time of occurrence of the different mutations. Owing to the fact that that this is rarely known from experiments (sets of mutations are observed to have occurred at points where genotyping is performed, for example, while the occurrence of each mutation cannot be tracked), censored formulations of the CT-CBN have also been studied (censored in the

sense that exact times of occurrence of mutations are not necessarily available) in [140]. A subset $g \subseteq \mathcal{E}$ of mutations is called a genotype. The genotype lattice, denoted by $\mathcal{G}$ consists of all genotypes that are compatible with the order constraints of $\mathcal{E}$. It defines the subset of possible mutational pathways (see Figure 2.13 for illustration). Algebraically, a genotype lattice is the distributive lattice of order ideals induced by the poset $\mathcal{E}$ (note that, as is generally done, we slightly abuse notation here by subsuming both the set and its partial order in $\mathcal{E}$). The occurrence times of mutations is usually assumed to follow independent exponential distributions. Further, the exponential waiting process for a mutation is considered to start only after occurrence of all of its parent mutations in the poset. Formally, for each mutation $e \in \mathcal{E}$, a random variable $Z_e \sim \text{Exp}(\lambda_e)$ can be defined. This leads to a definition of the statistical waiting times $T_{e,\text{stat}}$ recursively as the random variables

$$T_{e,\text{stat}} = \max_{j \in \text{pa}(e)} T_{j,\text{stat}} + Z_e, \tag{2.10}$$

for each mutation $e \in \mathcal{E}$. Here, $\text{pa}(e)$ denotes the set of mutations that are parent to mutation e in the poset $\mathcal{E}$.

The parameters λ_e of the CT-CBN are estimated by EM-based algorithms and as mentioned earlier, the censored nature of observations presents challenges. In the context of HIV, genotyping is typically performed only after therapy failure and this precludes the observation of the occurrence of each individual mutation. The sampling time T_s is assumed to be exponentially distributed with $T_s \sim \text{Exp}(\lambda_s)$, and independent from the poset. In this setting, if genotype g is observed, then $T_{e,\text{stat}} \leq T_s$ for all $e \in g$ and $T_{e,\text{stat}} > T_s$ for all $e \notin g$. Typically, one does not have access to λ_s and hence, in our work, we considered only the relative time scales of appearance of the different mutations. This was done by normalizing the statistical waiting times by the time to the fastest occurring mutation.

2.5.3 Prediction of genotype-phenotype relationships

Current guidelines for HIV therapy clearly recommend resistance testing in both treatment naïve patients and in patients with virological failure, regardless of the planned time for initiation or change of therapy [141]. Resistance testing prior to treatment initiation is also known to significantly improve the response to antiretroviral therapy [142]. The resistance of HIV mutant genotypes can be quantified by measurements from phenotypic replication assays or by empirical susceptibility scores assigned to results from genotyping assays. While the former is a direct quantification, the latter is subject to interpretation. Statistical learning techniques ranging from neural networks to decision trees have been extensively used to predict genotype-phenotype maps [8, 143]. Some of these approaches rely on classification of resistance levels into different drug-specific thresholds and predict ranges of resistance. Owing to the inherent difficulty in determining such appropriate cut-offs, support-vector machine based strategies and other regression techniques have also been developed to enable direct quantitative prediction of phenotypic attributes like resistance factors [144, 145].

Isotonic regression techniques have recently been proposed to predict resistance factors

from genotype-phenotype data [146]. Isotonic regression can be regarded as approximating a series of observations by a non-decreasing function. Given $a = (a_1, ..., a_n) \in \mathbb{R}^n$ and associated positive weights $w = (w_1, ..., w_n) \in \mathbb{R}^n_+$, the task is to approximate a by $y = (y_1, ..., y_n) \in \mathbb{R}^n$ subject to certain monotonic constraints of the form $y_i \geq y_j$. Formally, suppose $\mathbb{E} \subset \{1, ..., n\}^2$ is a set of all ordered pairs (i, j) corresponding to each constraint $y_i \geq y_j$, then the optimization problem

$$\begin{aligned} \min_y \sum_i w_i \cdot (y_i - a_i)^2 \quad \text{w.r.t.} \quad & y \in \mathbb{R}^n \\ & \text{such that} \\ & y_i \geq y_j \quad , \forall\, (i, j) \in \mathbb{E}, \end{aligned}$$

is referred to as isotonic regression. Here, $\mathbb{E}$ denotes the collection of constraints (if $\mathbb{E}$ is empty, the problem reduces to ordinary regression). This is a convex quadratic programming problem, and is tractable by standard numerical tools such as active-set algorithms. The existence of a unique global minimum can also be demonstrated (see [147] for example).

To amalgamate the prediction of resistance factors of the mutant genotypes into a Bayesian network model, the notion of an isotonic conjunctive Bayesian network (I-CBN) has been introduced [146]. For a fixed poset $(\mathcal{E}, \preceq)$ with an induced genotype lattice $\mathcal{G}$, the joint distribution of genotype-phenotype pairs (X, Y) is defined by the hierarchical model

$$\begin{aligned} X &\sim \text{CBN}(\mathcal{E}, \preceq, \theta) \\ Y|\{X = g\} &\sim \mathcal{N}(\mu_g, \sigma^2), g \in \mathcal{G}, \end{aligned} \tag{2.11}$$

where μ_g refers to the mean resistance factor of genotype g and σ^2 is a constant variance in the model. Here, $Y|\{X = g\}$ are the conditional phenotypes (say $Y = (y_g)$ for a genotype g) and these are assumed to be independent and normally distributed random variables.

Given the genotype lattice $\mathcal{G}$ of mutations represented by the CT-CBN, a resistance factor $\text{RF}_g = \mu_g$ is assigned to each genotype g. The estimation of the statistical models is performed in two steps. For example, to model resistance accumulation under ZDV therapy, in the first step, an I-CBN model is estimated using *in vitro* cross-sectional genotype–phenotype observations (from the Stanford HIV Drug Resistance Database [148]) for treatment regimens containing ZDV. The genotype–phenotype observations (1392, in number) were restricted to the Phenosense$^{\text{TM}}$ [149] or the Antivirogram$^{\text{TM}}$ [150] assays. The I-CBN model includes a poset of mutations and the estimated resistance factors. In the second step, based on the estimated poset, the fixation rate parameters λ_e of the CT-CBN model are estimated from the cross-sectional genotype observations of the Stanford HIV Drug Resistance Database by an EM-algorithm.

In practice, resistance factors are available for some genotypes from *in vitro* experiments, but not necessarily for all genotypes of interest. Note that in the model, it is assumed that resistance factors are non-decreasing over the genotype lattice in the di-

rection of evolution. Due to this monotonicity assumption, the regression problem is constrained, which serves as a means of regularization.

2.5.4 Prediction of treatment outcomes

The ultimate clinical goal is to identify an optimal salvage therapeutic regimen of drugs to a patient who has failed treatment. This necessitates the ability to predict treatment outcomes with different drug combinations, given information on phenotypic resistance, data on viral load, $CD4^+$ T-cells, past treatment history and other such measurable disease markers. However, the multitude of drug combinations available makes the task of therapy assessment by *in vitro* assays impossible.

To aid in quantifying genotypic resistance at failure and exploring salvage therapy options, rule-based systems [132,151] have been devised, resulting in measures such as the genotypic susceptibility score (GSS) [152]. The principle of GSS involves certain scores being assigned to different resistance mutations present, and a net score is then calculated for potential salvage therapy options, based on the current genotypic status of the patient. Hence, this approach is based on the current genotype in the patient. Recent studies have proposed the computation of a simplified individualized genetic barrier (IGB) that additionally takes into account the risk to acquire additional mutations via viral escape mechanisms [135]. The simplified IGB can also be computed for drug combinations and performs statistically well in the prediction of treatment outcomes. There are several other approaches that predict treatment outcomes by learning directly from large cohort data, and a detailed overview is beyond our current scope. We refer to [153] for a discussion on the benefits of such approaches, in general.

In summary, statistical models of mutation accumulation enable the understanding of viral evolutionary pathways and have applications in predicting phenotypic attributes of HIV such as resistance factors. They have also been profitably exploited to predict treatment outcomes. Current interests focus on efficient means to tackle problems of high dimensional data, and dealing with the combinatorial complexity in treatment possibilities. Studies on larger patient populations would strengthen the case of eventually integrating these methods into clinical practice.

Chapter 3

Fitness landscapes and evolution of HIV

In this chapter, we begin by briefly reviewing different notions of viral fitness, its theoretical and experimental measures and clinical relevance. We discuss some previous work from literature towards quantifying viral fitness using mathematical and statistical models. We then present an *in vivo* viral dynamics model, incorporating drug-specific mutation schemes that have been learned statistically from clinical data. Our aim is to estimate fitness characteristics from common cross-sectional clinical data by combining statistical methods designed for such data with a mechanistic model of virus dynamics, which explicitly accounts for viral fitness. This integration is achieved by (i) learning drug-specific mutational pathways from cross-sectional *in vivo* data and modelling viral infection dynamics on these genotype lattices, and (ii) by coupling the resistance factor, a readily accessible *in vitro* measure of drug resistance, to drug efficacy and rate constants of the virus-host dynamics *in vivo*.

Our model allows us to leverage sparse clinical data for the estimation of *in vivo* fitness characteristics, which is a first step towards analyzing and ultimately predicting clinical outcomes of drug combinations and assessing causes of therapy failure. To illustrate our modelling approach, we estimate fitness characteristics of HIV mutant genotypes that arise under treatment with two anti-retroviral drugs —zidovudine (a nucleoside reverse transcriptase inhibitor) and indinavir (a protease inhibitor). We also examine the utilities and limitations of such combined modelling approaches.

3.1 Viral fitness and its clinical relevance

3.1.1 Definitions of viral fitness and its quantifiers

From the perspective of evolutionary genetics, the fitness of an organism refers to its ability to survive and reproduce in a biological environment [154]. The quasispecies theory [155] of HIV postulates the existence of an ensemble of viral mutant genotypes at all times. The fitness of a certain mutant may be quantified in different ways.

One widely used measure of viral fitness is the reproductive ratio R_0 [118]. This is defined as the expected number of newly infected cells arising from a single infected cell in one cycle of replication. The notion of reproductive ratio has its origins in the study of demographics [156] and has been widely used in epidemiology to quantify the spread of diseases. For an infection to spread in a population of susceptible individuals, it is necessary that $R_0 > 1$. See [157] for a survey on the estimation, interpretation and applications of the reproductive ratio.

In the context of HIV infection models, the reproductive ratio is a measure of whether

the virus can establish an infection or not. For example, in the one-stage infection model (Eq. 2.1, Chapter 2), the reproductive ratio can be derived [158], and is given by

$$R_0 = \frac{\lambda_{\mathrm{TU}} \cdot \beta \cdot N}{\delta_{\mathrm{TU}} \cdot \delta_{\mathrm{T}^*} \cdot \mathrm{CL}} \tag{3.1}$$

Recent studies have estimated an average reproductive ratio of 8.0 in the early exponential infection phase of HIV-1 [158]. In a multi-strain infection model, the reproductive ratio of a certain mutant serves as a quantifier of its fitness [159, 160]. Note that in the context of such *within-host* models, R_0 reflects the infection process within a single individual, which is different from its role in characterizing epidemic spread [161].

Generalizations of the reproductive ratio, such as the reproductive capacity R_{cap}, have also been used to characterize the fitness of a certain state of infection [7]. The reproductive capacity $R_{\mathrm{cap}}(g)$ of a mutant genotype g can be interpreted as the total number of infectious offsprings of genotype g produced in a cycle of replication, given the current state of infection. Thus, it accounts for the contributions of different stages in the viral life cycle towards the production of pathogenic offsprings. For example, in the two-stage viral dynamics model (Eq. 2.3, Chapter 2), we have

$$\begin{aligned} R_{\mathrm{cap},g} \;=\; \sum_i \Big[& \mathrm{V_{I,g}} \cdot R_{\mathrm{V},g} + \mathrm{T}_{1,g} \cdot R_{\mathrm{T}_1,g} + \mathrm{M}_{1,g} \cdot R_{\mathrm{M}_1,g} \\ & + \mathrm{T}_{2,g} \cdot R_{\mathrm{T}_2,g} + \mathrm{M}_{2,g} \cdot R_{\mathrm{M}_2,g} + \mathrm{T}_{\mathrm{L},g} \cdot R_{\mathrm{T}_{\mathrm{L}},g} \Big]. \end{aligned} \tag{3.2}$$

Here, $R_{\mathrm{T}_1,g}$, $R_{\mathrm{T}_2,g}$, $R_{\mathrm{M}_1,g}$, $R_{\mathrm{M}_2,g}$, $R_{\mathrm{T}_{\mathrm{L}},g}$ and $R_{\mathrm{V}_{\mathrm{I}},g}$ are the reproductive ratios for the species T_1, T_2, M_1, M_2, T_{L} and V_{I} respectively. See [7] for a derivation of the reproductive capacity for the two-stage infection model. The reproductive number and reproductive capacities can be very difficult to determine *in vivo*, but *in vitro* replication capacity measurements are generally considered to be approximations to such quantities [162].

Another quantifier of viral fitness is the fitness cost, that was introduced earlier (see Eq. 2.8, Chapter 2). The fitness cost of a mutant genotype reflects the cost incurred by it in a certain step of the viral life cycle, relative to the wild type. In this sense, it is a measure of fitness at a more mechanistic level than the reproductive ratio or the reproductive capacity, which can be regarded as downstream read-outs in the viral life cycle. Fitness costs at such mechanistic levels have been measured by enzyme processivity assays [163, 164].

3.1.2 Experimental techniques to quantify viral fitness

There are numerous *in vitro* assays and some *in vivo* techniques to assess viral replication and fitness (see [165] for a review). This diversity in experimental techniques also implies differences amongst the assay set-ups, and a debate on the interpretation of fitness read-outs from such assays is still ongoing. Here, we list some of the common techniques and present details of one specific assay that has been used extensively to measure replication capacities in the data that we utilize.

Assays for viral fitness always compare the replication of a test strain (say, a mu-

tant genotype) to that of a reference strain (for example, the wild type). Two types of replication assays are well-known—parallel infection assays and growth competition assays. Parallel infection assays [166, 167] employ different pools of susceptible cells to assess replication of the test and reference strains, while growth competition assays [168] involve infection of a single culture of susceptible cells by two competing strains. Growth competition assays are generally preferred, in particular, when assessing small fitness differences [169]. They also reduce the impact of environment variations and experimental artifacts as the two strains are compared in the same culture. Fitness assays can also be classified on the basis of whether replication is allowed for one or multiple cycles of infection. Single cycle assays are shorter and less sensitive. The widely used commercial Monogram Biosciences RC assay [149, 170] involves a single cycle of replication and generally employs an *env*-deleted HIV vector, resulting in viral progeny that are incapable of further infection. Further variation amongst assays can arise from the type of susceptible cells used for infection ranging from cell-lines to human peripheral blood mononuclear cells and the impact of this has also been studied (see [171], for example). In growth-competition assays, several methods are available to distinguish the reference and test strains, including heteroduplex tracking assays [172] and real-time polymerase chain reaction (RT-PCR) based assays [170, 173].

The Monogram Biosciences RC assay, a modification of the PhenoSense resistance assay has been widely used to determine replication capacity of HIV mutant strains isolated from patients. We briefly outline its features here, since the fitness data that we compare our results to, are either determined directly using this assay, or some modification of it. We refer to [149] for a detailed description of the assay.

First, the viral RNA is purified from the patient plasma sample and then the protease, reverse-transcriptase (first 313 codons) and 3'-end of *gag* region are isolated and amplified using RT-PCR. The patient-derived sequence is cloned into a vector that contains a luciferase (*luc*) reporter gene, and then transfected into a mammalian cell-line, together with a plasmid that contains a gene coding for an amphotropic-murine leukemia virus envelope (A-MLV *env*). This results in the production of a pool of infectious patient-derived recombinant viruses. The pool of viruses is then used to infect a cell-line and viral replication is quantified by assaying for expression of *luc*. Only a single round of infection is possible, since the recombinant viruses lack an envelope protein. The assay does suffer from limitations. The use of an A-MLV envelope instead of that of HIV-1 could potentially influence replication rates. Additionally, recent studies on protease inhibitor resistant mutations have pointed out consequences of the inability of this assay to assess the impact of mutations in the *env* region [92]. Nevertheless, the assay has been in widespread use owing to its commercial availability.

Other techniques, such as the rapid cell turnover assay [174], are also used in practice to assess viral replication. Though a detailed discussion on the different assay techniques is not the focus here, we note the impact of variability present in literature, as regards fitness estimates.

3.1.3 Clinical relevance

While replication capacity measurements from *in vitro* assays approximately reflect fitness characteristics of mutant genotypes, their *in vivo* relevance is not well-understood. Recent theoretical studies have indicated that predicted replicative capacities have a significant correlation with the viral load, a known surrogate marker of disease progression [175]. Clinical investigations [176, 177] have demonstrated inverse correlations of baseline $CD4^+$ T-cell count with replication capacities. Disease progression monitoring in patient cohorts has also suggested a correlation between viral load and replication capacities [178]. An analysis of viral load data from the Study of the Consequences of the Protease Inhibitor Era (SCOPE) in patients undergoing antiretroviral therapy showed that viral isolates from individuals with suppressed viral loads had reduced replicative capacities [179]. In the context of selection of treatment options, certain mutations such as the lamivudine resistant 184V are known to increase susceptibility to other nucleoside reverse transcriptase inhibitors and the benefits of taking advantage of this fact have been acknowledged [180]. Alternatives proposed for virological control have included the intentional use of suboptimal drug regimens to maintain a low-fitness variant [181], although the escape of such a variant to a fitter genotype is a constant threat.

Using mutagenic molecules to drive HIV mutation rates beyond a certain error threshold has been a topic of interest, and the antiviral potential of such agents has been demonstrated [182]. The postulation of an error catastrophe had its beginnings in the concept of viral quasispecies [183], wherein the viral replication mechanism is destroyed when the mutation rates are increased beyond a certain threshold. Recent simulation-based studies have also provided estimates of the error threshold to be within 2-6 times of the natural mutation rate, suggesting a high susceptibility of the virus to such mutagenic drugs [184]. Conceptually, exploiting the idea of an error catastrophe relies on trapping the viral quasispecies ensemble in a fitness valley. Better characterizations of evolutionary trajectories and fitness landscapes of HIV may thus aid in investigating the mechanisms of such novel therapeutic strategies.

Another realm where HIV fitness comes into play is the transmission of drug-resistance mutations. The transmission of HIV is a complex process and its success depends on several factors including the abundance of mutations in blood and/or genital secretions. However, it was earlier observed that only about 8-10% of known drug resistant mutations were identified in treatment naïve patients. This, along with other evidence from surveillance studies of newly-infected patients, led to the hypothesis that a reduced fitness of drug-resistant mutations lowered their rates of transmission. However, some recent studies have suggested a hidden epidemic of transmitted resistance—drug resistant mutations with low fitness costs, such as the thymidine analog mutation 70R can reach self-sustaining levels in certain communities [185].

In summary, replicative capacities and other measures of fitness have shown clinical significance and more studies are needed to dissect the complex and confounding factors affecting *in vivo* fitness of HIV.

3.2 Viral fitness in mathematical models

3.2.1 Statistical models to predict fitness characteristics

Early work characterizing fitness of HIV mutant genotypes using experimental techniques [168, 186] resorted to simple methods of quantifying fitness differences. Typically, the ratio of two mutant genotypes of interest was plotted logarithmically against time and the fitness was read off from the slope. That is, if WT(t) and M(t) represented the wild type and mutant population over time t, then

$$\log \frac{\mathrm{M(t)}}{\mathrm{WT(t)}} = \log \frac{\mathrm{M(0)}}{\mathrm{WT(0)}} + t \cdot \log F \tag{3.3}$$

where, F denotes the fitness difference between the mutant and the wild type. Clearly, this yields only the absolute fitness difference between the two variants, and not the relative fitness ratio. A major assumption underlying the derivation of Eq. (3.3) is that the rates of replication of the competing strains are constant in time. This is often violated both *in vitro* and *in vivo*. Consequently, Marée et al [187], and later Bonhöffer et al [188] developed a growth-corrected method to estimate relative fitness ratios from time-course data. The growth-corrected method also circumvents the need for an estimate of the generation time *in vitro*. This method has since been also used in *in vivo* estimations of fitness measures from experimental data [189, 190].

Recent work has enabled prediction of replication capacities from large-scale *in vitro* data. Hinkely et al [162] used a generalized kernel ridge regression approach to fit data from 70,081 virus sample measurements of replication capacities. Briefly, the fitness function used accounted for main effects due to mutations and two-point epistatic interactions.

$$\log W_s = I + \sum_{ij} M_{ij} \cdot s_{ij} + \sum_{ijkl} E_{ij,kl} \cdot s_{ij} \cdot s_{kl}, \tag{3.4}$$

where W_s denotes the replication capacity of viral sequence s, I denotes the intercept, i.e, the replication capacity of the reference strain, M_{ij} is the main effect on fitness of allele j at position i, $E_{ij,kl}$ is the epistatic effect on fitness that allele l at position k has on allele j at position i and s_{ij} denotes the presence ($s_{ij} = 1$) or absence ($s_{ij} = 0$) of allele j at position i. Strong epistatic interactions, particularly intragenic epistasis, were found to exist in the HIV-1 protease and reverse transcriptase fitness landscapes. This work also led to the observation that predicted replicative capacities correlated well with viral load measurements and thus have a clinical significance [175].

Statistical models utilizing information-theoretic techniques and decision trees [8] have been used to establish genotype-phenotype correlations and to estimate phenotypic attributes such as resistance factors from genotype data and partially observed phenotypes. More recently, isotonic regression methods have also been used to predict resistance factors [146].

3.2.2 Estimating *in vivo* fitness parameters

Most experiments measuring viral fitness characteristics are performed *in vitro*. Clearly, the complex *within-host* environment that the virus is exposed to, is different from laboratory cell-cultures. The fitness of a HIV-1 variant within the host is subject to a multitude of selection pressures and depends on the genetic background, immune control [191], fluctuating drug concentrations [192] and target cell availability [193] amongst others, that cannot be wholly mimicked *in vitro*.

Although less numerous, there are studies using viral dynamics models that have estimated fitness costs *in vivo* of HIV mutant genotypes. Goudsmit et al [194] deduced a broad spectrum of *in vivo* fitness costs for mutations at codons 41 and 215 in the RT region of HIV-1. Devereux et al [195] monitored genotypic evolution of the viral population in eleven patients undergoing treatment interruption after NRTI and PI therapy, and estimated fitness costs of different mutations based on their rates of disappearance. The mutations 184I and 184V confer resistance to lamivudine and Frost et al [193] used viral load data from lamivudine monotherapy in conjunction with a simple mathematical model to estimate relative fitness costs of the two mutant genotypes. More recently, [196], while investigating increasing $CD4^+$ T-cell levels with almost constant viral load after therapeutic failure, estimated *in vivo* fitness cost of 38A, a mutation in the Gp41 region of HIV-1, that leads to resistance to the fusion inhibitor enfuvirtide.

Investigations of large scale *in vivo* fitness landscapes have also been performed [197]. These rely on sequence information derived from patient cohorts and first predict the evolutionary paths of mutations. Next, they assume a fitness function and estimate its parameters from the cross-sectional sequence data.

In summary, while mathematical models have been developed to predict replicative capacities from *in vitro* data, and at times to also estimate *in vivo* fitness measures from detailed viral load measurements, there is a lack of knowledge on fitness costs of mutations, resistance and the complex interplay between the two in an *in vivo* context. Further, the sparsity of cross-sectional clinical data is a severe limitation to more detailed models.

3.3 Development of a viral dynamics model with *in vivo* drug-specific mutation schemes

Motivation

As discussed in Chapter 2, mathematical models of *in vivo* viral infection dynamics and statistical mutation models have both provided critical insights into HIV-1 disease and therapy. However, the utility of the former in studying the emergence of drug-specific mutations and resistance, is limited by the availability of realistic mutation landscapes. Existing approaches typically use mutation schemes that are unspecific for the drug or coarse-grained [198–200]. On the other hand, statistical models of mutational pathways do not integrate details of the viral infection dynamics and the specific actions of different drug classes. In viral mutational landscapes, the path to resistant mutants that fixate

and eventually cause therapy failure typically consists of several intermediate mutants. Understanding the accumulation of mutations and associated genotypic and phenotypic changes is critical for prediction of treatment failure and selection of optimal patient-specific treatments [201]. Additionally, it has been observed that models incorporating quasispecies distributions of HIV-1 mutants can lead to a different qualitative behaviour than what would be expected from simplified mutation models [202].

Attempts to estimate fitness parameters in an *in vivo* setting [193, 196] have relied mainly on detailed time course measurements of different mutant strains, which is a severe limitation in the most common situation of sparse data collected during routine clinical diagnostics. Thus, there is a definite need for an approach that combines the merits of the mechanistic and statistical approaches, to estimate viral fitness characteristics, and better understand the dynamics of mutation accumulation during anti-retroviral treatment.

Model description

We described *in vivo* viral infection dynamics by extending the two-stage model (Eq. 2.3, Chapter 2 and presented in detail in [203]) for multiple mutant genotypes. The model allowed for integrating drug-specific mutation schemes and the actions of all approved antiretroviral drug classes including reverse transcriptase inhibitors, protease inhibitors and integrase inhibitors. Since mutations are primarily a result of error-prone reverse transcription [62], both forward and backward mutations were considered. The average error rate in viral reverse transcription is about $\mu = 3 \cdot 10^{-5}$ mutations per nucleotide per cycle of replication; and two-thirds of these mutations are known to be base-pair substitutions [62]. In agreement with [200], we used the following nucleotide-specific mutation rates: for a G $\rightarrow$ A nucleotide change, we set a mutation rate of $\mu_1 = 1 \cdot 10^{-5}$ (because about half of the base-pair mutations are of this type [62]), for mutations involving nucleotide changes A $\rightarrow$ G, we used a lower rate of $\mu_2 = \mu_1/2$, and for transversion and other mutations (involving a change from a purine to a pyrimidine or *vice-versa*), we set $\mu_3 = \mu_1/10$.

The system of ODEs governing the viral dynamics model with the integrated mutation scheme was given by:

$$
\begin{aligned}
\frac{\mathrm{d}}{\mathrm{dt}}\mathrm{TU} &= \lambda_{\mathrm{TU}} - \delta_{\mathrm{TU}} \cdot \mathrm{TU} + \sum_{g\in\mathcal{G}} \delta_{\mathrm{PIC,T}} \cdot \mathrm{T}_{1,g} - \sum_{g\in\mathcal{G}} \beta_{\mathrm{T},g} \cdot \mathrm{V}_{\mathrm{I},g} \cdot \mathrm{TU} \\
\frac{\mathrm{d}}{\mathrm{dt}}\mathrm{MU} &= \lambda_{\mathrm{MU}} - \delta_{\mathrm{MU}} \cdot \mathrm{MU} + \sum_{g\in\mathcal{G}} \delta_{\mathrm{PIC,M}} \cdot \mathrm{M}_{1,g} - \sum_{g\in\mathcal{G}} \beta_{\mathrm{M},g} \cdot \mathrm{V}_{\mathrm{I},g} \cdot \mathrm{MU} \\
\frac{\mathrm{d}}{\mathrm{dt}}\mathrm{T}_{1,g} &= \beta_{\mathrm{T},g} \cdot \mathrm{V}_{\mathrm{I},g} \cdot \mathrm{TU} - \big(\delta_{\mathrm{T1}} + \delta_{\mathrm{PIC,T}} + k_{\mathrm{T},g}\big)\cdot \mathrm{T}_{1,g} \\
\frac{\mathrm{d}}{\mathrm{dt}}\mathrm{M}_{1,g} &= \beta_{\mathrm{M,g}} \cdot \mathrm{V}_{\mathrm{I},g} \cdot \mathrm{MU} - \big(\delta_{\mathrm{M1}} + \delta_{\mathrm{PIC,M}} + k_{\mathrm{M},g}\big)\cdot \mathrm{M}_{1,g} \\
\frac{\mathrm{d}}{\mathrm{dt}}\mathrm{T}_{2,g} &= \sum_{g'\in\mathcal{G}} (1-p) \cdot k_{\mathrm{T},g'} \cdot \mathrm{T}_{1,g'} \cdot r_{g'\to g} + \alpha \cdot \mathrm{T}_{\mathrm{L},g} - \delta_{\mathrm{T2}} \cdot \mathrm{T}_{2,g} \\
\frac{\mathrm{d}}{\mathrm{dt}}\mathrm{M}_{2,g} &= \sum_{g'\in\mathcal{G}} k_{\mathrm{M},g'} \cdot \mathrm{M}_{1,g'} \cdot r_{g'\to g} - \delta_{\mathrm{M2}} \cdot \mathrm{M}_{2,g} \\
\frac{\mathrm{d}}{\mathrm{dt}}\mathrm{T}_{\mathrm{L},g} &= \sum_{g'\in\mathcal{G}} p \cdot k_{\mathrm{T},g'} \cdot \mathrm{T}_{1,g'} \cdot r_{g'\to g} - \alpha \cdot \mathrm{T}_{\mathrm{L},g} - \delta_{\mathrm{TL}} \cdot \mathrm{T}_{\mathrm{L},g} \\
\frac{\mathrm{d}}{\mathrm{dt}}\mathrm{V}_{\mathrm{I,g}} &= \mathrm{N}_{\mathrm{TI},g} \cdot \mathrm{T}_{2,g} + \mathrm{N}_{\mathrm{MI},g} \cdot \mathrm{M}_{2,g} - \Big[\mathrm{CL_V} + \big(\mathrm{CL}_{\mathrm{T},g} + \beta_{\mathrm{T},g}\big)\mathrm{TU} + \\
&\qquad \big(\mathrm{CL}_{\mathrm{M},g} + \beta_{\mathrm{M},g}\big)\mathrm{MU}\Big] \cdot \mathrm{V}_{\mathrm{I},g} \\
\frac{\mathrm{d}}{\mathrm{dt}}\mathrm{V}_{\mathrm{NI,g}} &= \mathrm{N}_{\mathrm{TNI},g} \cdot \mathrm{T}_{2,g} + \mathrm{N}_{\mathrm{MNI},g} \cdot \mathrm{M}_{2,g} - \mathrm{CL_V} \cdot \mathrm{V}_{\mathrm{NI,g}}
\end{aligned}
$$

where the subscript g refers to a mutant genotype g from the genotype lattice $\mathcal{G}$. The poset genotype lattice $\mathcal{G}$ and the underlying poset $\mathcal{E}$ and resistance factors used were were obtained from continuous-time conjunctive Bayesian network and isotonic regression models, as described in Chapter 2. This statistical component of the model was implemented in collaboration with co-authors of [203]. We modelled mutations as occurring between stages T_1 and T_2 of the infection cycle. We embedded the genotype lattice $\mathcal{G}$ into the system of ODEs and enabled mutation reactions compatible with $\mathcal{G}$. In line with the genotype lattice, we only considered mutation events between genotypes g' and g that differed by a single amino acid. The probability $r_{g'\to g}$ of such a single amino acid mutation to occur per replication cycle was classified into amino acid mutations requiring a single underlying base pair mutation and those requiring two underlying base pair mutations:

$$
r_{g'\to g} = \begin{cases} \mu & \text{; single underlying base pair mutation} \\ \frac{1}{2}\mu & \text{; double underlying base pair mutation} \end{cases} \tag{3.5}
$$

For a background on this assumption and for further details on parameterization, we refer the interested reader to [203]. For the drug action, we assumed that reverse transcriptase inhibitors such as ZDV inhibit the infection rates β_{T}, β_{M} and the rates of clearance due to unsuccessful infection $\mathrm{CL_T}$ and $\mathrm{CL_M}$, while protease inhibitors such as IDV inhibit the viral production rates $\mathrm{N_{TI}}$ and $\mathrm{N_{MI}}$.

Drug-effects and fitness costs were incorporated into the appropriate reaction rates as explained in Chapter 2. In the absence of drug (i.e., $\epsilon = 0$), resistance plays no role and

it is clear that the wild type would eventually outcompete the mutant. In the presence of drug, the fitness of a mutant genotype g depends on the dynamic interplay between the two factors: the fitness cost s_g and the resistance factor RF_g. We quantified the overall fitness of a mutant genotype g relative to the wild type by the selective advantage (similar to [204]) as

$$\mathrm{SA}_g = \frac{(1 - s_g) \cdot (1 - \gamma_{\epsilon_g} \epsilon_g)}{(1 - s_{\mathrm{wt}}) \cdot (1 - \gamma_{\epsilon_{\mathrm{wt}}} \epsilon_{\mathrm{wt}})} \tag{3.6}$$

with $s_{\mathrm{wt}} = 0$ by definition. We refer to Eqs. (2.4)–(2.8), Chapter 2 for descriptions of $\gamma_{\epsilon_g}, \gamma_{\epsilon_{\mathrm{wt}}}, \epsilon_g$ and ϵ_{wt}. If $\mathrm{SA}_g > 1$, the mutant g has a replicative advantage over the wildtype in the presence of drug.

To quantify epistatic interactions between mutations, we defined an epistatic coefficient $E_{ij,\mathcal{D}}$ between mutations i and j in an environment with drug $\mathcal{D}$ ($\mathcal{D} = \Phi$ denotes the absence of drug), as follows.

$$E_{ij,\mathcal{D}} = \mathrm{SA}_{\mathrm{avg},ij} \cdot \mathrm{SA}_{\mathrm{wt}} - \mathrm{SA}_{\mathrm{avg},i} \cdot \mathrm{SA}_{\mathrm{avg},j} \tag{3.7}$$

where, $\mathrm{SA}_{\mathrm{avg},ij}$ denotes the average selective advantage of all mutant genotypes containing both mutations i and j, $\mathrm{SA}_{\mathrm{avg},i}$ denotes the average selective advantage of mutant genotypes containing mutation i, but not mutation j, and $\mathrm{SA}_{\mathrm{avg},j}$ denotes the average selective advantage of mutant genotypes containing mutation j, but not mutation i.

Estimation of fitness characteristics

Having specified the parameters of the two-stage dynamical model of viral infection, a mutation landscape of genotypes, resistance factors and drug efficacies, the only unknown parameters of the model were the fitness costs of the different genotypes. These unknown parameters were estimated by comparison of predicted mechanistic waiting times (based on the mechanistic model of viral infection dynamics) to the statistical waiting times (Eq. 2.10, Chapter 2). We linked the statistical point of view in terms of mutations and the mechanistic point of view in terms of mutant genotypes as follows.

A given mutant genotype $g \in \mathcal{G} \subset 2^{\mathcal{E}}$ was defined as the set of all mutations $e \in \mathcal{E}$ that are manifested in g. We defined the mechanistic waiting time $T_{e,\mathrm{mech}}$ for each mutation $e \in \mathcal{E}$, as the earliest time, at which the following two criteria were satisfied: (i) all the mutant genotypes containing the mutation e together constituted at least 20% of the total viral population V_{tot}; the 20% detection threshold reflects the limitations of the genotyping assay [205]; and (ii) the total viral load was greater than a typical detection limit $\mathcal{L} =$ 500 copies/ml of viral RNA, that enables genotyping [206]. This resulted in the following definition of the mechanistic waiting time of mutation e:

$$T_{e,\mathrm{mech}} = \inf \left\{ t \geq 0 : \sum_{g \in \mathcal{G}; e \in g} V_g(t) > 0.2 \cdot V_{\mathrm{tot}}(t) \quad \text{and} \quad V_{\mathrm{tot}}(t) > \mathcal{L} \right\}. \tag{3.8}$$

As discussed in Chapter 2, the average waiting times computed from the statistical model $T_{e,\mathrm{stat}}$ are dependent on the sampling rate λ_s, to which we typically do not

have access. As a solution to this problem, we compared only the relative time scales of appearance of the different mutations. This was done by normalizing the statistical waiting times by the time to the fastest occurring mutation, and then comparing these to correspondingly normalized mechanistic waiting times.

For simulations of the mechanistic viral dynamics model under therapy, we first performed a pre-treatment steady state computation to estimate levels of different mutants at the onset of therapy. All model simulations were performed with MATLAB$^{\mathrm{TM}}$ R2010b. For estimation of fitness costs, we used the MATLAB$^{\mathrm{TM}}$ optimization function *fminsearchbnd* that is based on the Nelder-Mead simplex direct search algorithm [207] to perform the constrained least-squares estimation

$$\min_{s\in[0,1]^{|\mathcal{G}|}} \sum_{e\in\mathcal{E}} (\mathbb{E}[T_{e,\mathrm{stat}}] - T_{e,\mathrm{mech}})^2, \tag{3.9}$$

where $T_{e,\mathrm{mech}}$ depends on the fitness costs $s = (s_g)_{g\in\mathcal{G}}$ via the system of ODEs specifying the viral dynamics. Fitness costs s_g with $g \in \mathcal{G}$ were then defined as the solution of eq. (3.9). Note that in addition to the constraints on fitness costs, the mechanistic waiting times are also subject to the order constraints imposed by the structure of the mutation poset. Further refinement of the optimization was carried out by simulated annealing. To examine the relevance of parameter identifiability, we performed 500 rounds of estimation and analyzed our results on an ensemble of fits instead of one best fit. The robustness of parameter estimation and techniques to alleviate this issue in our setting are detailed in Chapter 6 of this thesis.

3.4 Estimation of fitness landscapes of HIV mutants under zidovudine therapy

We used the partially ordered set (poset) of mutations (Figure 3.1A) associated with resistance to zidovudine (ZDV) and the corresponding genotype lattice (Figure 3.1B) that were estimated from the Stanford HIV Drug Resistance Database [148]. The poset and the rates of fixation λ_e (Table 3.2) for each mutation were estimated by a continuous-time conjunctive Bayesian network (CT-CBN). The resistance factors of the mutant genotypes were learned using isotonic conjunctive Bayesian network (I-CBN) models. The poset of mutations reflected clustering along the well-known thymidine analog mutations (TAM)-1 and -2 mutation pathways.

3.4.1 Fitness costs, resistance factors and selective advantages

We focussed on the key thymidine-analog mutations (TAMs) that arise under ZDV monotherapy: 41L, 67N, 70R, 210W, 215Y and 219Q. The mutations are classified intoTAM-1 (41L, 215Y, 210W) and TAM-2 (67N, 70R, 219Q) mutants [208, 209] and two mixed mutants (with cross-TAM profiles). Mixed mutants are observed to generally occur with a lower frequency [210]. We used a drug efficacy of $\epsilon_{\mathrm{wt}} = 0.75$ on the wild type (corresponding to a drug concentration of 3 times the $\mathrm{IC50}_{\mathrm{wt}}$) to illustrate our results. This value was

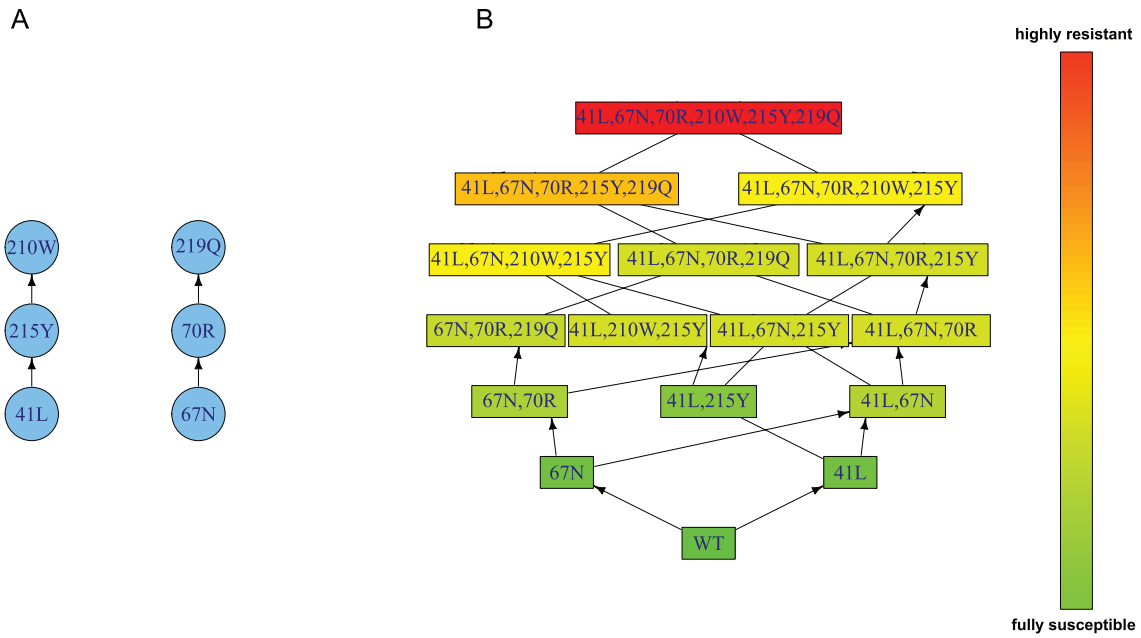

Figure 3.1. Partially ordered set (poset) and induced genotype lattice for mutations associated with resistance to ZDV. A. Poset of resistance development to ZDV. Vertices represent mutations and directed edges represent the order constraints of mutation accumulation. We observe the clustering of thymidine analog mutations (TAMs) along the two classical TAM-1 and TAM-2 pathways that is well-known under ZDV therapy [208, 209]. The left arm of the poset (mutations 41L, 215Y and 210W) is the TAM-1 pathway, while the right arm (mutations 67N, 70R and 219Q) is the TAM-2 pathway. **B.** Genotype lattice of mutants induced by the poset of mutations in **A**. The vertices represent the genotypes that are compatible with the poset in **A**. Predicted levels of phenotypic resistance are color-coded (green, fully susceptible; red, highly resistant).

chosen to match average nadir values in viral load after ZDV monotherapy (a drop of $\sim$1 log unit from baseline, within 7–10 days of therapy and a nadir at $\sim$3 weeks) [211].

The estimated fitness costs and selective advantages (Table 3.1 and Figure 3.2) were in excellent agreement with established knowledge from several *in vitro* assays and some *in vivo* observations. The mechanistic predicted waiting times also had a high and statistically significant correlation (r=0.995, p<0.05) with the statistical waiting times (Table 3.2). Our estimates of fitness costs were within general reported ranges of $(0.1 - 0.4)$ [159, 186, 196, 212]. Additionally, we also agreed with observations on fitness characteristics of specific mutant genotypes. For example, it is well known that the addition of the 210W mutation into a {41L, 215Y} backbone has opposing effects on fitness depending on the presence or absence of ZDV. In the absence of ZDV, the triple mutant {41L, 210W, 215Y} has been observed to be less fit than {41L, 215Y}, while the introduction of ZDV causes a reversal, i.e., the triple mutant becomes fitter than the double mutant [213, 214]. This was well-reflected in our estimates (Table 3.1). We observed that this reversal in fitness upon adding ZDV is because of the higher fitness cost of the triple mutant being more than offset by the resistance acquired in the presence of drug. This can be seen by comparing the selective advantages and fitness costs for the corresponding double and

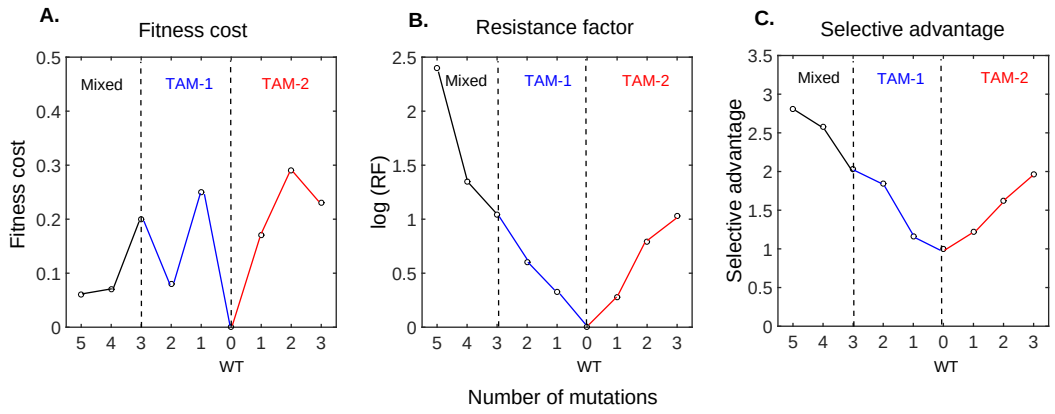

Figure 3.2. Fitness costs, resistance factors, and selective advantages of mutants arising under ZDV therapy. A. Estimated fitness costs (normalized by setting fitness cost of wild type to 0), **B.** Resistance factors (normalized by setting resistance factor of wild type to 1), on a logarithmic scale, and **C.** Estimated selective advantages (normalized by setting selective advantage of wild type to 1) of ZDV mutants . In **A**, **B** and **C**, the x-axis depicts the number of mutations. The TAM-1 mutants (joined by blue solid lines) are to the left and TAM-2 mutants (joined by red solid lines) are to the right of the wild type. The mixed mutants (joined by black solid lines) are to the left of the TAM-1 mutants. The TAM-1, TAM-2 and mixed mutants are separated by vertical dashed lines.

triple mutants in the TAM-1 pathway (Figure 3.2).

TAM-1 mutations are known to occur at almost double the frequency of TAM-2 mutations [215]. This difference was reflected in our results by mutants containing TAM-1 mutations having lower fitness costs than those containing TAM-2 mutations. Additionally, we also observed that the selective advantages of TAM-1 mutants is higher, on average, than their TAM-2 counterparts. This is also in concordance with observations that TAM-2 mutations accumulate only after much longer durations of monotherapy with ZDV [210].

The presence of 41L together with 215Y is a strong predictor of virological failure in patients on ZDV monotherapy [216]. We estimated a low fitness cost for this TAM-1 double mutant and also observed the presence of these two mutations in mutant genotypes contributing to therapy failure.

Our estimated fitness costs are also supported by other *in vitro* investigations on the order of fitness values, such as the TAM-1 triple mutant {41L, 210W, 215Y} being fitter than its TAM-2 counterpart [186] and the TAM-2 double mutant {67N, 70R} being less fit than the single mutant {67N} [217]. Notably, we concurred with the observation in [217] that the occurrence of 70R in a 67N or {67N, 219Q} backbone has a significant cost.

Further, our model also allowed us to quantify epistatic interactions (Eq. (3.7)) between different mutations. We observed predominantly positive epistatic interactions in fitnesses, with the absence of drug, while the introduction of ZDV resulted in small, but negative epistatic coefficients (Table 3.3). Epistasis in HIV fitness landscapes has been a topic of considerable debate [218–220]. There is evidence of positive epistasis at least *in vitro*, especially in a drug-free environment [218]. Recent work, however, has shown

Table 3.1. Estimated fitness costs for ZDV mutants.

Mutant	log RF	Fitness cost	Comment
WT	0	0	Wild type
{67N}	0.28 (0.15, 0.49)	0.17 (0.14, 0.24)	TAM-2
{67N, 70R}	0.79 (0.59, 0.99)	0.29 (0.27, 0.36)	TAM-2
{67N, 70R, 219Q}	1.03 (0.95, 1.11)	0.23 (0.18, 0.30)	TAM-2
{41L}	0.32 (0.18, 0.52)	0.25 (0.17, 0.34)	TAM-1
{41L, 215Y}	0.60 (0.53, 0.65)	0.08 (0.07, 0.11)	TAM-1
{41L, 210W, 215Y}	1.04 (0.95, 1.09)	0.20 (0.16, 0.26)	TAM-1
{41L, 67N, 210W, 215Y}	1.35 (1.30, 1.42)	0.07 (0.05, 0.08)	Mixed
{41L, 67N, 70R, 210W, 215Y, 219Q}	2.40 (1.73, 2.79)	0.06 (0.04, 0.07)	Mixed

Estimated resistance factors (on a logarithmic scale, log RF, column 2) and fitness costs (column 3) of TAM-1 and TAM-2 mutants and two mixed mutants arising during ZDV therapy. In parentheses, are the 95% confidence intervals for the estimates obtained from 200 bootstrap samples.

that the buffering effect of such epistasis on acquisition of mutations, is only minimal, and moreover, in the presence of drug, epistasis changes in sign to being mildly negative [171]. The importance of the fitness ranking of different mutant genotypes on epistasis and its relevance is also stressed. More large-scale studies are needed to better assess the magnitude and relevance of epistasis. Though for a small subset of mutations, our results are a step in this direction.

3.4.2 Mutational abundance, competition and rebound

In addition to estimated fitness characteristics, the viral load time courses predicted by our model gave insights into the dynamics of different mutations. In the TAM-2 pathway, we observed a transient disappearance of mutations 70R and 219Q before their eventual fixation. Interestingly, such behaviour has been reported earlier [221] for the mutation 70R. This phenomenon is attributed to the competition between TAM-1 and TAM-2 mutations: the mutation 70R appears initially and is then outcompeted by 215Y. 70R later fixates in the population after being associated with 67N and other TAM-1 mutations (Figure 3.3C).

Further to this observation, since our model included the different mutant genotypes, we could readily resort to dissecting their contribution to the appearance and disappearance of underlying mutations. Interestingly, unlike 70R, the TAM-1 mutations desist from exhibiting such behaviour and have a more direct route to fixation (Figure 3.4). This is due to the longer persistence of 'pure' TAM-1 containing mutant genotypes, partly owing to their low finess costs.

Our results were also in agreement with an earlier study [200] where a mechanistic modelling approach was used to fit drug efficacy and fitness parameters to clinically observed mutant data under zidovudine and lamivudine therapy. As observed in this study, the lack of adequate suppression of the wild type strain contributes significantly to the initial rebound in the viral load. In this scenario, the wild type strain initially rebounds

Table 3.2. Statistical and mechanistic waiting times to observe mutations under ZDV therapy.

Mutation (e)	Normalized statistical mutation rates (λ_e/λ_s)	Statistical average waiting times	Mechanistic waiting times
41L	0.81 (0.73, 0.88)	1.00	1.00
67N	0.73 (0.68, 0.82)	1.10	1.10
70R	0.75 (0.63, 0.87)	2.18	2.26
210W	4.11 (3.29, 4.96)	1.28	1.29
215Y	9.19 (6.50, 17.17)	1.08	1.01
219Q	5.14 (3.77, 8.80)	2.34	2.26

The statistically estimated rates of occurrence of different mutations (column 2) with 95% confidence intervals in parentheses, the average statistical waiting times (column 3) and the corresponding mechanistic waiting times (column 4) to observe mutations at the different positions under ZDV therapy. The average statistical and mechanistic waiting times are calculated as described in Sections 2.5.2 (Chapter 2) and in the previous section of the current chapter. Both waiting times are expressed relative to the time to the fastest occurring mutation.

Table 3.3. Estimated epistatic coefficients for mutations under ZDV therapy.

Mutations (i,j)	Epistatic coefficient in the absence of drug($E_{ij,\Phi}$)	Epistatic coefficient in the presence of ZDV($E_{ij,\mathrm{ZDV}}$)
(41L, 67N)	0.30	0.001
(41L, 70R)	0.31	-0.07
(41L, 219Q)	0.28	-0.1
(67N, 210W)	0.32	-0.06
(67N, 215Y)	0.27	-0.04
(70R, 210W)	0.30	-0.15
(70R, 215Y)	0.28	-0.12
(210W, 219Q)	0.27	-0.19
(215Y, 219Q)	-0.63	-0.71

Estimated epistatic coefficients of fitness amongst mutations in the absence and presence of ZDV.

leading to virological failure and then later declines after being out-competed by the mutants (Figure 3.5A). In comparison to [200], our model incorporates detailed drug-specific mutation pathways. Furthermore, it relies only on sparse clinical data, as opposed to extensive viral load measurements.

To study how the fitness of the viral population changes over time during the course of treatment, we computed the total replicative fitness $\mathrm{F}_{\mathrm{rel}}(t)$ of HIV-1 under ZDV monotherapy as follows.

$$\mathrm{F}_{\mathrm{rel}}(t) = \frac{\sum_g \mathrm{V}_g(t) \cdot \mathrm{SA}_g}{\sum_g \mathrm{V}_g(t=0)} \tag{3.10}$$

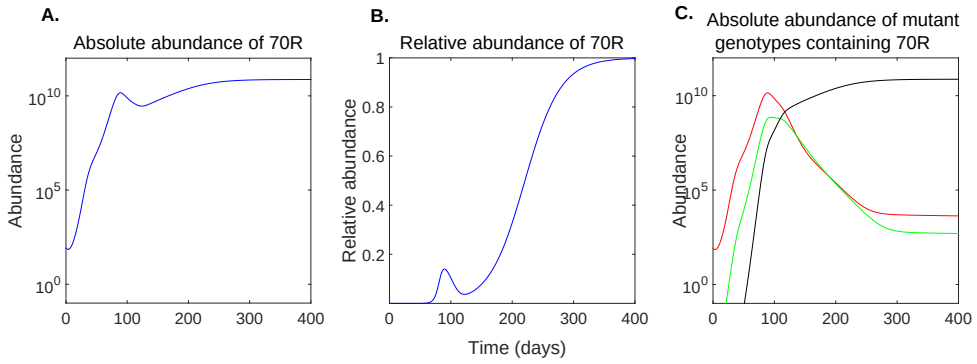

Figure 3.3. Abundance of the 70R mutation and mutant genotypes with 70R under ZDV therapy. A. Absolute abundance (in numbers) of the 70R mutation. **B.** Relative abundance of the 70R mutation in the viral population. The transient appearance and eventual fixation of the mutation 70R can be seen. **C.** Absolute abundance (in numbers) of mutant genotypes containing the mutation 70R. The absolute abundance of a certain mutation is calculated by adding all mutant genotypes containing the mutation. The mutant genotypes shown are the TAM-2 double (red) and triple (green) mutants, and the mixed and sextuple (black) mutants.

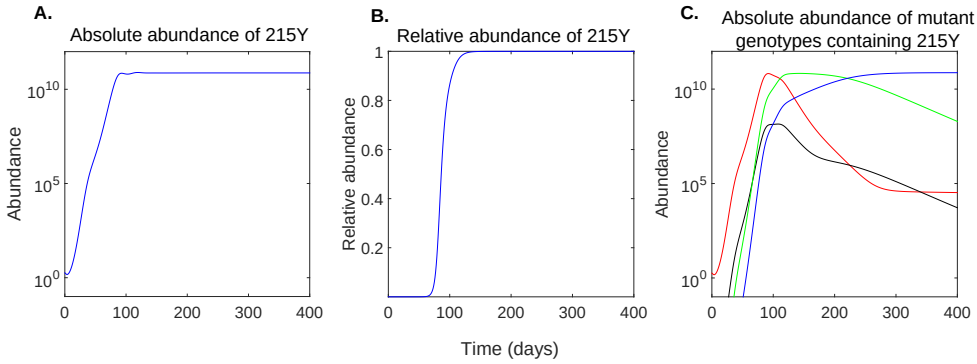

Figure 3.4. Abundance of the 215Y mutation and mutant genotypes with 215Y under ZDV therapy. A. Absolute abundance (in numbers) of the 215Y mutation. **B.** Relative abundance of the 215Y mutation in the viral population. **C.** Absolute abundance (in numbers) of mutant genotypes containing the mutation 215Y. The absolute abundance of a certain mutation is calculated by adding all mutant genotypes containing the mutation. The mutant genotypes shown are the TAM-1 double (red) and triple (black) mutants, and the mixed quadruple (green) and sextuple (blue) mutants.

The viral population has two means of increasing its total fitness—by increasing the viral load or by selecting mutant genotypes with a higher selective advantage. Figure 3.5B captures both these influences. We noted that in spite of the early rebound and a rather poor antiviral effect, the initial 'hit' phase lasting until about 3 weeks succeeds in reducing the fitness of the population to ∼10% of the pre-treatment value (Figure 3.5B). We also observed how the viral population continues to evolve even well after the total viral load has attained its set-point level upon failure (after ∼ 150 days. This also re-iterates the importance of treatment changes being effected at the right time after (or even before!) the detection of failure [122].

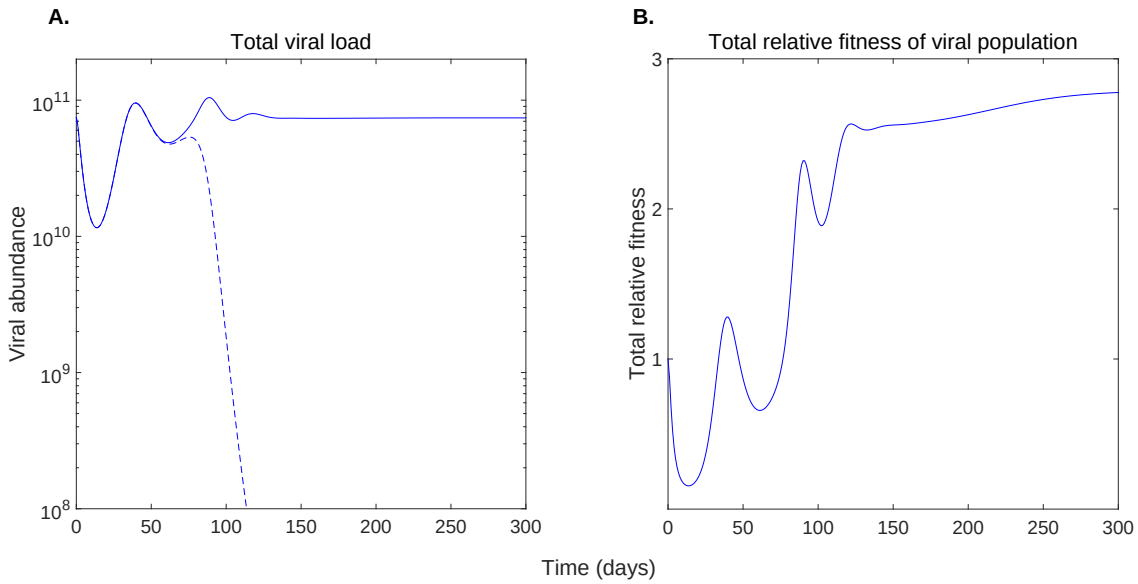

Figure 3.5. Total viral load and total relative fitness under ZDV therapy. A. The total viral load (solid blue line) and the wild type population (dashed blue line) are plotted against time in days. **B.** The total relative fitness of the viral population (calculated from Eq. (3.10)).

3.5 Estimation of fitness landscapes of HIV mutants under indinavir therapy

We again used the the poset (Figure 3.6A) and genotype lattice (Figure 3.6B) of mutations associated with resistance to indinavir (IDV), a protease inhibitor estimated from the Stanford HIV Drug Resistance Database [148], and the corresponding resistance factors of IDV mutants predicted by isotonic regression. We focussed on the five mutations 46I, 54V, 71V, 82A, and 90M. Four of these (46I, 54V, 82A and 90M) are among the most frequent primary (major) mutations reported in the Stanford HIV Drug Resistance Database under IDV therapy [148].

We chose 71V to represent a common secondary (minor) mutation to study possible compensatory fitness effects. We used a drug efficacy $\epsilon_{\text{wt}} = 0.90$ on the wild type to illustrate our results. This value was chosen to match average nadir values in viral load after IDV monotherapy (a drop of ∼1–1.5 log units within 3–4 weeks of therapy) [97,222].

The estimated fitness costs, resistance factors and selective advantages (Table 3.4 and Figure 3.7) agreed well with reported experimental findings. As with ZDV, the mechanistic predicted waiting times also had a high and statistically significant correlation (r=0.9995, $p<0.05$) with the statistical waiting times (Table 3.5). In general, we observed that early mutations have a high fitness cost, while the accumulation of further mutations succeeds in compensating almost entirely for this loss in fitness (Figure 3.7A). This is in agreement with clinical observations that mutations selected early during therapy with protease inhibitors cause impaired protease function and that subsequent accumulation of mutations

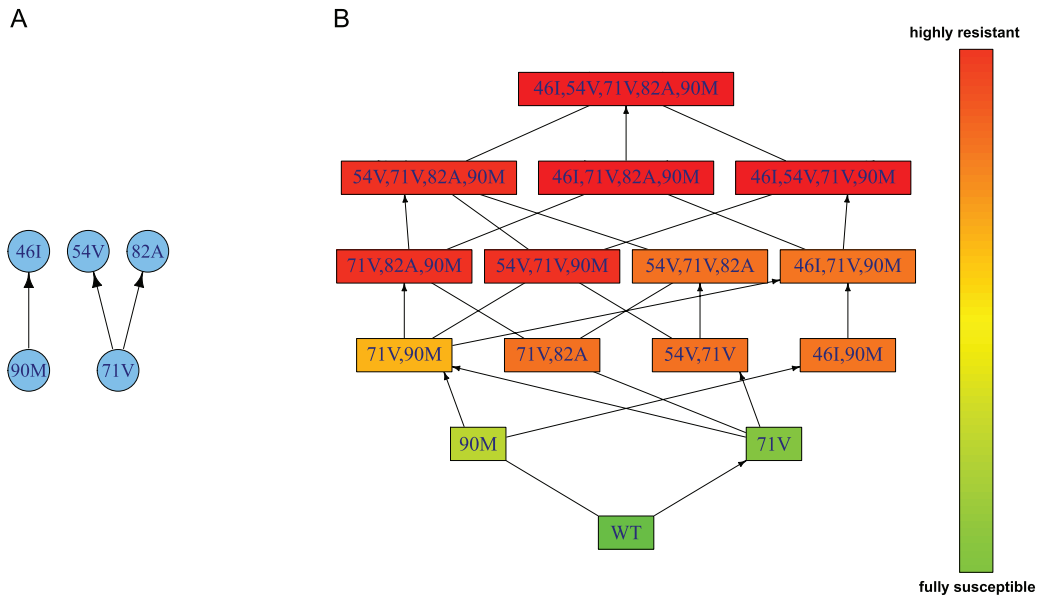

Figure 3.6. Partially ordered set and induced genotype lattice for mutations associated with resistance to IDV. A. Poset of the continuous time conjunctive Bayesian network for resistance development to IDV. **B.** The genotype lattice of mutants induced by the poset in **A**. The vertices represent the genotypes that are compatible with the poset in **A**. The predicted levels of phenotypic resistance are color-coded (green= fully susceptible, red = highly resistant).

Table 3.4. Estimated fitness costs for IDV mutants.

Mutant	log RF	Fitness cost	Type
WT	0	0	Wild type
{90M}	0.59 (0.56, 0.72)	0.36 (0.33, 0.38)	Single point (M)
{71V}	0.32 (0.26, 0.48)	0.45 (0.38, 0.50)	Single point (m)
{46I, 90M}	1.28 (1.26, 1.37)	0.66 (0.56, 0.70)	Double (MM)
{71V, 90M}	1.08 (1.04, 1.18)	0.31 (0.29, 0.34)	Double (mM)
{54V, 71V}	1.29 (1.26, 1.37)	0.49 (0.47, 0.54)	Double (Mm)
{71V, 82A}	1.29 (1.26, 1.37)	0.42 (0.39, 0.44)	Double (mM)
{54V, 71V, 82A}	1.29 (1.26, 1.34)	0.58 (0.53, 0.71)	Triple (MmM)
{54V, 71V, 90M}	1.52 (1.35, 1.64)	0.28 (0.26, 0.34)	Triple (MmM)
{71V, 82A, 90M}	1.52 (1.45, 1.64)	0.39 (0.32, 0.42)	Triple (mMM)
{46I, 71V, 90M}	1.28 (1.26, 1.34)	0.44 (0.41, 0.47)	Triple (MmM)
{54V, 71V, 82A, 90M}	1.52 (1.45, 1.64)	0.28 (0.22, 0.32)	Quadruple (MmMM)
{46I, 71V, 82A, 90M}	1.67 (1.57, 1.74)	0.31 (0.28, 0.33)	Quadruple (MmMM)
{46I, 54V, 71V, 90M}	1.67 (1.65, 1.74)	0.15 (0.12, 0.17)	Quadruple (MMmM)
{46I, 54V, 71V, 82A, 90M}	1.67 (1.65, 1.74)	0.04 (0.03, 0.05)	Quintuple (MMmMM)

Estimated resistance factors (on a logarithmic scale, log RF, column 2) and fitness costs (column 3) of mutants arising during IDV therapy. In parentheses, are the 95% confidence intervals for the estimates obtained from 200 bootstrap samples. Mutant types (column 4) are encoded by one 'M' for each major mutation and one 'm' for each minor mutation in the genotype.

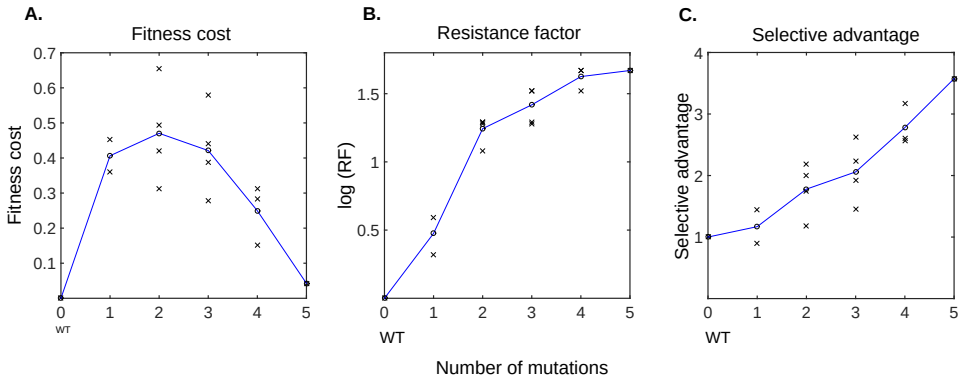

Figure 3.7. Fitness costs, resistance factors and selective advantages of mutants arising under IDV therapy. A. Estimated fitness costs (normalized by setting fitness cost of wild type to 0), **B.** Resistance factors, on a logarithmic scale (normalized by setting resistance factor of wild type to 1), and **C.** Estimated selective advantages (normalized by setting selective advantage of wild type to 1) of IDV mutants. In **A**, **B** and **C**, the x-axis depicts the number of mutations. Black crosses represent the values for the different mutant genotypes, while the blue solid line represents the average of fitness costs, resistance factors and selective advantages across all mutant genotypes with a given number of mutations.

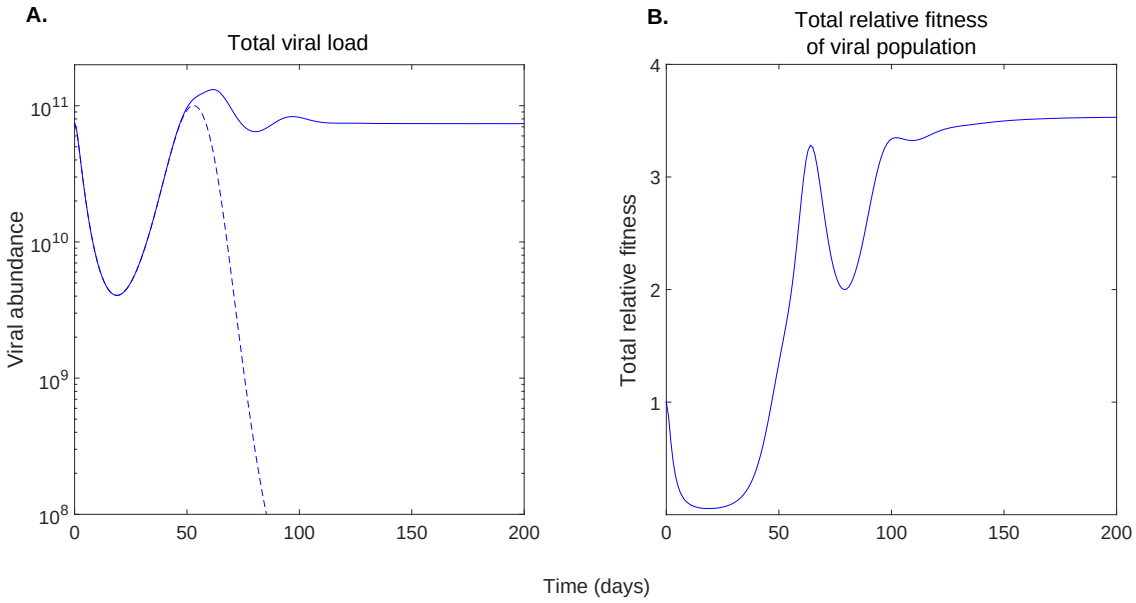

Figure 3.8. Total viral load and total relative fitness under IDV therapy. A. The total viral load (solid blue line) and the wild type population (dashed blue line) are plotted against time in days. **B.** The total relative fitness of the viral population (calculated from Eq. (3.10)).

compensates for this fitness cost [223, 224]. A striking behaviour that we noted is the presence of staircases in the fitness landscape, which has also been described earlier [225]. We observed a monotonic increase of the average selective advantages of the mutants with increasing number of mutations (Figure 3.7C). This observation provides additional rea-

soning for the accumulation of mutations during IDV therapy. Notably, the high fitness costs for the double and triple mutants (Figure 3.7A) are not sufficient to deter their occurrence, as their fitness costs are well-offset by resistance (Figure 3.7B), which facilitates further climbing of the fitness landscape by accumulating mutations (Figure 3.7C).

Table 3.5. Statistical and mechanistic waiting times to observe mutations under IDV therapy.

Mutation (e)	Normalized statistical mutation rates (λ_e/λ_s)	Statistical average waiting times	Mechanistic waiting times
46I	1.49 (1.20, 1.84)	1.47	1.53
54V	2.03 (1.68, 2.61)	1.36	1.44
71V	0.69 (0.62, 0.76)	1.02	1.00
82A	1.13 (0.92, 1.44)	1.64	1.71
90M	0.70 (0.62, 0.76)	1.00	1.00

The statistically estimated rates of occurrence of different mutations (column 2) with 95% confidence intervals in parentheses, the average statistical waiting times (column 3) and the corresponding mechanistic waiting times (column 4) to observe mutations at the different positions under IDV therapy. The average statistical and mechanistic waiting times are calculated as described in Sections 2.5.2 (Chapter 2) and in the previous section of the current chapter. Both waiting times are expressed relative to the time to the fastest occurring mutation.

In addition to these general fitness trends, specific characteristics of particular mutations were also in line with prior findings. The minor mutation 71V is known to play a compensatory role [226]. In our estimates, this was observed by a partial recovery in fitness of the triple mutant {46I, 71V, 90M} compared to the double mutant {46I, 90M} from 0.66 to 0.44 (Table 3.4). In the presence of IDV, the addition of 54V to a {71V, 82A} backbone is known to not confer a significant advantage [227], and this was reflected by a ratio of approximately 1.3 for the selective advantages of this pair of mutants. Furthermore, as in [228], we noted a higher fitness cost for the single mutant 71V as compared to 90M.

Table 3.6. Estimated epistatic coefficients for mutations under IDV therapy.

Mutations (i,j)	Epistatic coefficient in the absence of drug($E_{ij,\phi}$)	Epistatic coefficient in the presence of IDV($E_{ij,\mathrm{IDV}}$)
(46I, 54V)	0.59	-0.04
(46I, 71V)	0.56	0.03
(46I, 82A)	0.48	-0.08
(54V, 82A)	0.26	-0.20
(54V, 90M)	0.52	-0.02
(71V, 90M)	0.47	0.03
(82A, 90M)	0.43	-0.05

Estimated epistatic coefficients of fitness amongst mutations in the absence and presence of IDV.

Maarseveen et al observed the persistence of protease resistant mutants for long periods of time even after the cessation of therapy [226]. They argue that the reversal of the underlying mutations might not be feasible due to lower replication capacities of intermediate mutants upon reversion. Our results support this hypothesis by showing that the most resistant strain that develops after therapy failure is very unlikely to reverse back in the mutational landscape, owing to a fitness barrier encountered in its reversion to the wild type (Figure 3.7A).

Further, in spite of eventual viral rebound (Figure 3.8A), an inspection of the total relative fitness of the viral population under IDV therapy (Figure 3.8B) revealed that the drug succeeds in maintaining the population at a fitness of $<10\%$ for $\sim$5 weeks of therapy. This again points to the role that a timely treatment intervention can play, even in the face of modestly effective therapies. We again computed epistatic coefficients both in the presence and absence of IDV (Table 3.6) and observed a similar trend (as with ZDV) of positive epistasis in a drug-free environment and predominantly negative coefficients in the presence of IDV.

3.6 Sensitivity analysis

Since the viral turn-over parameters are subject to uncertainty, a sensitivity analysis of the predictions of mechanistic waiting times with respect to these parameters was performed. We use the example of ZDV therapy to illustrate this. To this end, we chose each turn-over parameter (the death rates of the different stages, the infection rates, the rates of integration of viral DNA and clearance of the infectious and non-infectious viruses) from a uniform distribution with a range of up-to $\pm 50\%$ of their original value. This is a sufficiently large range of perturbation compared to a 20-25% range reported for viral clearance and death rates of infected cells in [114], 5-10% standard errors reported in [229] or 2-12% standard errors estimated in [230]. The mean predicted waiting times (Figure 3.9) retained an excellent correlation ($r = 0.98$, $p<0.05$) with the average statistical waiting times. This showed our predictions to be robust with respect to variations in the parameters of the virus dynamics model.

Our model of dynamics is deterministic. However, the evolution of viral mutant genotypes is dictated by random events. We expect the impact of stochasticity to be dependent on the so-called genetic barrier, i.e., the number of mutations needed to confer high level resistance (larger than 10-fold increase). Drugs with a high genetic barrier are expected to result in lower viral load levels, such that fluctuations become (relatively) more important. The drugs we considered in our analysis, however, have a low genetic barrier (approximately 2 mutations needed for 10-fold increase in resistance levels). Nevertheless, to assess the impact of stochasticity quantitatively, we performed hybrid deterministic-stochastic simulations of our model, where rare mutation events were modelled stochastically, while e.g., the viral infection dynamics of abundant genotypes was modelled deterministically (a fully stochastic simulation would hardly be feasible even on supercomputers). The employed hybrid algorithm is discussed in [231], where the mathematical basis and the implementation details are given. For illustration of our results here, we chose IDV, since it

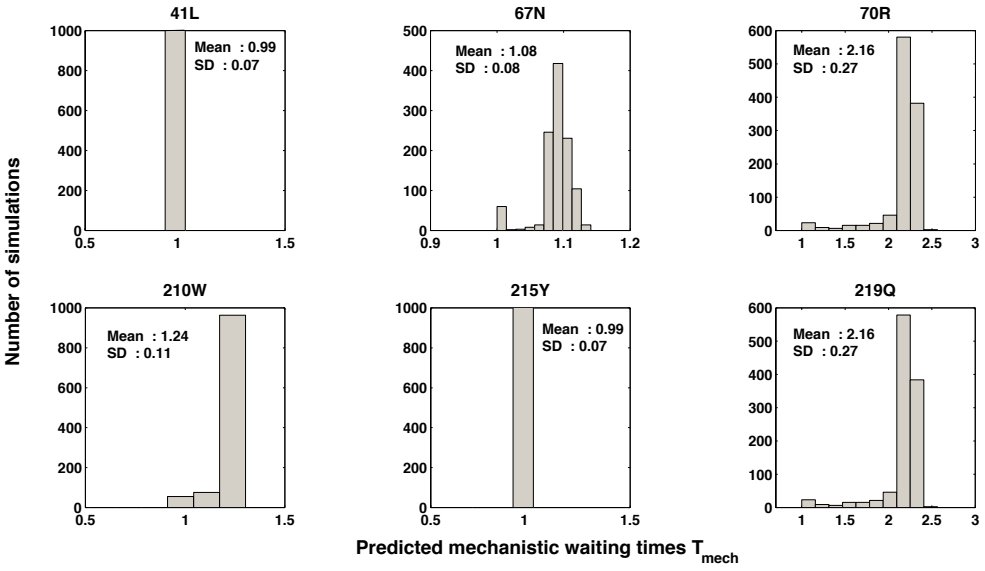

Figure 3.9. Distribution of mechanistic waiting times from 1000 simulations of the virus dynamics model. The turn-over parameters of the virus dynamics model for ZDV therapy were perturbed by up to ±50% and 1000 simulations were performed by choosing parameters from a uniform distribution on this range. The distribution of the waiting times to different mutations with their mean and standard deviation (SD) are shown.

is a more effective drug than ZDV in that it drives the viral load to lower levels. We chose a reaction propensity threshold of 10^{-3} and performed 500 realizations. The predicted mechanistic waiting times continued to agree well (Table 3.7, Figure 3.10) with the average statistical waiting times ($r=0.98$, $p< 0.05$). We observed a delay in the appearance of certain mutations, in particular the later mutations. This is in line with similar observations made earlier [232]. A hybrid estimation procedure is also possible, in principle, but suffers from increased computation times. Our model utilizes a deterministic framework and thus is an approximation. However, for the examples we considered, the model-based fitness costs, resistance factors, selective advantages and other features of viral dynamics agree well with experiments. The design of more efficient hybrid stochastic-deterministic approaches or alternative stochastic estimation methods could aid in more robust and realistic models, with the deterministic predictions as the starting point for a subsequent hybrid approach.

3.7 Model limitations

The presented viral infection dynamics model incorporating drug-specific *in vivo* mutation landscapes aimed at capturing the complex competition dynamics between the different mutant strains. It was based on a simplified representation of drug efficacies. In Chapter 5, we analyze how varying drug concentrations affect the time of emergence of mutant genotypes. If detailed data on drug pharmacokinetics and patient-specific viral load dynamics and baseline characteristics are available, a population-pharmacokinetic/pharmacodynamic analysis would be the appropriate approach to account for inter-individual variations [233].

Table 3.7. Median of mechanistic waiting times predicted from 500 hybrid deterministic-stochastic simulations of the model for IDV therapy.

Mutation (e)	Statistical average waiting times	Median of mechanistic waiting times
46I	1.47	2.69
54V	1.36	2.42
71V	1.02	1.01
82A	1.64	4.01
90M	1.00	1.00

The statistical and median mechanistic waiting times (derived from 500 hybrid deterministic- stochastic realizations) of the model for IDV therapy. The predicted mechanistic waiting times continue to correlate well with the statistical waiting times (r = 0.98, p-value = 0.0006).

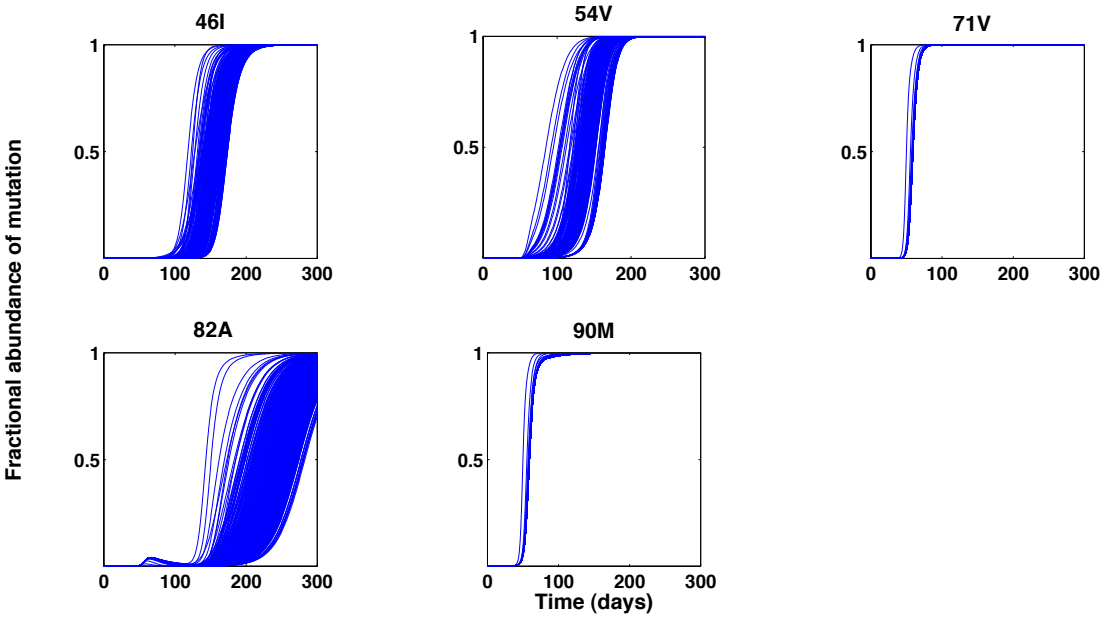

Figure 3.10. Predicted mutational abundance from 500 hybrid deterministic-stochastic simulations of IDV therapy. The model for IDV therapy is simulated using a hybrid deterministic-stochastic model to compute 500 realizations. The predicted fractional abundance of different mutations is shown.

Without such detailed data, as in our setting, constant drug concentrations and effects is a reasonable assumption, which was used in most prior analyses [5]. Further, while deterministic simulations represent the average dynamical behaviour of the system, stochastic effects would need to be incorporated using numerical hybrid algorithms [231] to explain the variability in clinical data.

There are several mechanisms of resistance in HIV-1 infection. In addition to the mechanisms included in the two-stage virus dynamics model, features such as the compensatory Gag mutations [234] and other compensatory mechanisms adopted by HIV-1 have also been described, including frame-shifts in the Gag region that increase viral protease expression levels [235]. These effects can be integrated by including information on

the Gag region into the mutational scheme and this extended model may then partially account for higher observed fitness levels of some mutants.

3.8 Summary

We presented an HIV-1 infection dynamics model with statistically learned drug-specific *in vivo* mutational landscapes. Our approach relied on typical and frequently available clinical data, which consists of censored observations, as opposed to scarce extensive time course measurements of different mutant genotypes. Mutations were detected through their appearance in specific mutant genotypes and our model described how their dynamics is coupled. For both ZDV and IDV, our estimated fitness characteristics showed excellent agreement with experimental knowledge. Our model also extends to multiple-drug regimens, and this would be examined next in Chapter 4.

Chapter 4

Understanding HIV dynamics under combination therapy

In the last chapter, we presented a virus dynamics model incorporated with drug-specific mutation schemes learned from clinical data. As an application, we estimated fitness characteristics of HIV mutant genotypes in the presence and absence of drugs, and illustrated this using monotherapy with two standard antiretroviral drugs - zidovudine (ZDV) and indinavir (IDV). However, the current standards in antiretroviral therapy involve the administration of a combination of several drugs, for example in the HAART. Recently, there has been great interest in using mathematical models of antiretroviral therapy to perform clinical trial simulations [160]. The identification of reasons contributing to the failure of certain treatment regimens and the evaluation of optimal salvage options constitute the main objectives behind these studies. While simulations based on monotherapy can yield valuable insights on viral dynamics, implementing multiple-drug therapy with drug-specific mutational pathways is a step towards analyzing realistic current therapy regimens.

In this chapter, we discuss how our virus dynamics model extends to multiple drugs. We illustrate our results using therapies comprising of two and three drugs. We also assess the impact of variability in parameters of the virus dynamics model (that could reflect underlying inter-individual variability in the immune system, for example). Next we present a modification of our model for the incorporation of a new class of anti-HIV drugs under development, namely molecules that target host cellular factors. Our model helps in understanding two conflicting mechanisms of drug action—the inhibition and promotion of transcription rates in HIV-infected cells. Inhibiting transcription (by targeting host transcription factors, for example) has the impact of lowering viral replication ratess [236]. We extend our model to incorporate the action of such antiviral molecules and parametrize our model using *in vitro* data from literature. We then examine the impact of such molecules in an *in vivo* setting using our model. Finally, we conclude with a brief discussion on the perspectives of modelling approaches in antiretroviral therapy and the challenges that lie ahead.

4.1 Extension of viral dynamics model to combinations of drugs

To simulate a combination therapy with multiple drugs using our viral dynamics model, we require a poset of mutations (see Section 2.3.5, Chapter 2). This is constructed by combining the posets of the individual drugs. For example, if $\mathcal{E}_{\mathrm{D}_i}$ denotes the poset of

mutations under monotherapy with drug D_i, then the poset $\mathcal{E}_{D_1+\ldots+D_n}$ under a combination therapy with the n drugs—$D_1, \ldots D_n$, can be written as the disjoint union of the individual posets $\mathcal{E}_{D_i}$. That is,

$$\mathcal{E}_{D_1+\ldots+D_n} = \biguplus \mathcal{E}_{D_i}, \tag{4.1}$$

with the partial order relation in the poset $\mathcal{E}_{D_1+\ldots+D_n}$ being the disjoint union of the partial orders in each of the individual posets $\mathcal{E}_{D_i}$.

Next, the two characteristics associated with mutant genotypes, namely fitness costs and resistance factors, have to be computed. Here, we illustrate this with an example of a dual therapy with drugs D_1 and D_2 from two different drug-classes. For clarity in illustration, we use simplified mutation schemes (Figure 4.1).

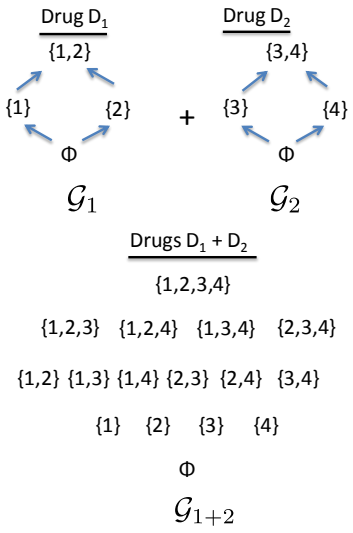

$\mathcal{G}_1$ $\mathcal{G}_2$

$\mathcal{G}_{1+2}$

Figure 4.1. Dual therapy with drugs D_1 and D_2. The genotype lattices of mutations under monotherapy with drugs D_1 and D_2, and with their combination. A simplified mutation scheme with only two mutations 1 and 2 for drug D_1 and two mutations 3 and 4 for drug D_2 is used. The directed edges representing transitions between genotypes in the lattice $\mathcal{G}_{1+2}$ are omitted for clarity.

If $\mathcal{G}_{D_1+D_2}$ is the combined genotype lattice induced by the combined poset $\mathcal{E}_{D_1+D_2}$ of mutations under the dual therapy, then a mutant genotype $g \in \mathcal{G}_{D_1+D_2}$ has contributions from two sources towards both its fitness cost s_g and resistance factor RF_g—one, from the underlying mutations in g to drug D_1 and the other due to the mutations in g to drug D_2. As before, the drug influence manifests as changes in the reaction rates of appropriate target steps of our viral dynamics model, the only difference being that there are two target steps, instead of one in monotherapy. We assumed mutations in two different genomic regions (corresponding to the two different target processes in the viral life cycle) to be free from fitness and resistance epistasis. This is a reasonable assumption in view of studies indicating that intragenic epistatic effects are more significant than intergenic

epistatic effects [162].

Consider a mutant genotype $g = g_1 \cup g_2$, resistant to the dual therapy with drugs D_1 and D_2 from different drug classes, with $g_1 \in \mathcal{G}_{D_1}$ and $g_2 \in \mathcal{G}_{D_2}$. If $k_{wt,0}^{D_1}$ and $k_{wt,0}^{D_2}$ are the reaction rate constants of the corresponding target steps in the wild type in the absence of any drug, we write

$$k_{g,\epsilon_{g_1}}^{D_1} = (1 - \gamma_{\epsilon_{g_1}} \epsilon_{g_1}) \cdot (1 - s_{g_1}) \cdot k_{wt,0}^{D_1}. \tag{4.2}$$

and

$$k_{g,\epsilon_{g_2}}^{D_2} = (1 - \gamma_{\epsilon_{g_2}} \epsilon_{g_2}) \cdot (1 - s_{g_2}) \cdot k_{wt,0}^{D_2}. \tag{4.3}$$

Here, ϵ_{g_1} and ϵ_{g_2} are the efficacies of drugs D_1 and D_2 on the mutant genotypes g_1 and g_2 (defined as in Eq. 2.5, Chapter 2), while s_{g_1} and s_{g_2} are the associated fitness costs. If D_1 and D_2 are from the same drug class, we require additional assumptions on intragenic epistatic effects. Two notions of drug-interactions are commonly used to model net drug efficacy of jointly acting drugs —Bliss independence [237] and Löwe additivity [238].

Briefly, if C_1 and C_2 are the (averaged) concentrations of the two drugs D_1 and D_2 with 50% inhibitory concentration values of $IC50_1$ and $IC50_2$ respectively (for the wild type), the net drug efficacy under the Bliss-independence model (ϵ_{BI}) on a mutant genotype $g \in \mathcal{G}$ that has a resistance factor RF_1 to drug D_1 and a resistance factor RF_2 to drug D_2 can be written as

$$\epsilon_{BI} = 1 - \frac{1}{1 + C_1/(RF_1 \cdot IC50_1)} \cdot \frac{1}{1 + C_2/(RF_2 \cdot IC50_2)}, \tag{4.4}$$

On the other hand, the Löwe additivity model implies a net drug efficacy (ϵ_{LA}) of

$$\epsilon_{LA} = 1 - \frac{1}{1 + C_1/(RF_1 \cdot IC50_1) + C_2/(RF_2 \cdot IC50_2)}. \tag{4.5}$$

Jilek et al [239] showed that neither of these two models precisely predicts drug-interactions for common anti-HIV drugs, and that the net drug efficacies are often characterized by synergistic or antagonistic effects, which they quantified using the notion of a degree of independence (see [239] for details on the computation of this quantity). We used their approach to predict net drug efficacies in our triple drug example (Section 4.4), where we have two drugs from the same drug class.

For all simulations of combination therapies in our studies, we used the adaptive ODE-solver *ode15s* in MATLAB^{TM} R2010b with relative and absolute tolerances of 10^{-3}, and a non-negativity constraint. To study the effects of changing drug-efficacy parameters on treatment outcomes, we performed simulations of the dual therapy with different individual drug-efficacies for 300 days. To classify therapy outcomes, we monitored total viral load and detected failure when the viral RNA exceed 500 copies/ml [206]. Again, we chose this threshold to correspond with limits of genotyping assays. We reported no detection of failure if the viral load does not exceed this threshold within our simulation time.

4.2 Dual therapy simulation

To illustrate the application of our viral dynamics model in the setting of multiple drugs, we first performed simulations of a dual antiretroviral therapy with the reverse transcriptase inhibitor ZDV and the protease inhibitor IDV. We used the posets of mutations for ZDV and IDV that we estimated earlier (Figures 3.1 and 3.6), together with the resistance factors and fitness costs of the different mutant genotypes (computed as explained in Section 4.1). Our main goal was to assess the treatment outcomes with different individual drug efficacies and ascertain the reasons for failure of the dual regimen. To this end, we used a range of ϵ_{wt} values for ZDV and IDV to account for differential drug effects and adherence patterns, and studied the treatment outcome by monitoring the total viral load. Our simulations enabled us to predict the dominant mutant genotypes at the point of failure. Based on this, we classified failure as being due to wild type, mutations resistant to ZDV, mutations resistant to IDV or mutations resistant to both drugs used.

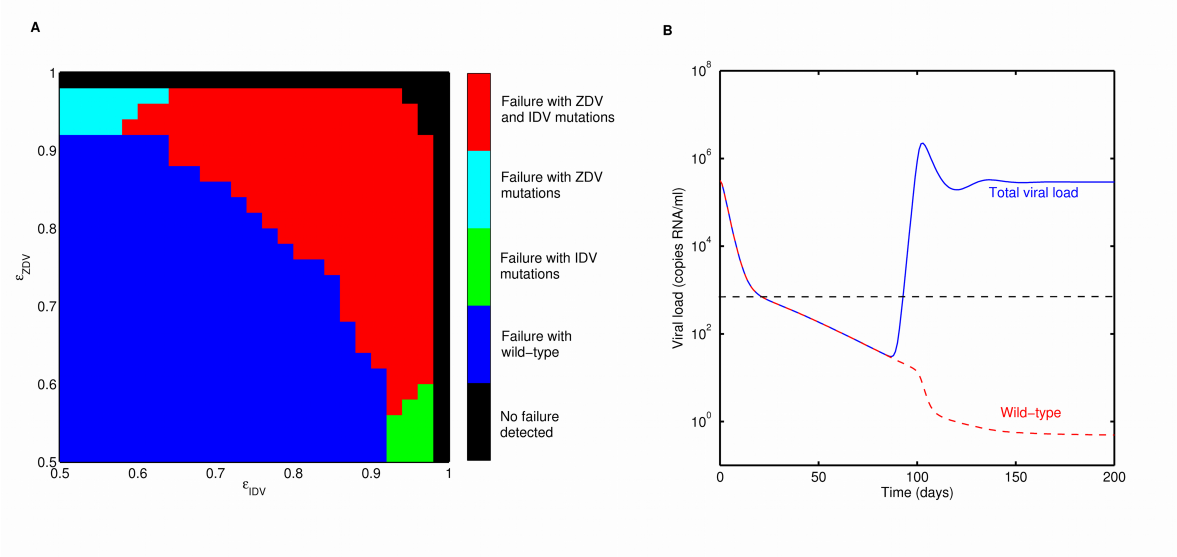

Figure 4.2. Treatment outcome with ZDV+IDV dual therapy. A. Genotypic reasons of treatment failure were assessed in terms of mutations present at point of virological failure. For different combinations of drug efficacies $\epsilon_{\text{wt,ZDV}}$ and $\epsilon_{\text{wt,IDV}}$, the different genotypic reasons of failure are shown in different colours. The treatment outcome could be failure with mutations resistant to both ZDV and IDV (red), failure with mutations resistant only to ZDV (light blue), failure with mutations resistant only to IDV (green), failure with wild type (blue), or no detection of failure (black). **B.** Viral load (in copies RNA/ml) under ZDV+IDV therapy with $\epsilon_{\text{wt,ZDV}} = 0.75$ and $\epsilon_{\text{wt,IDV}} = 0.90$. The blue line shows the total viral load, while the red dashed line depicts the wild type. The horizontal black dashed line represents the detection threshold used (500 copies/ml).

We observed that there are different regimes of the individual drug efficacies ($\epsilon_{\text{wt,ZDV}}$ and $\epsilon_{\text{wt,IDV}}$) that result in varying causes of failure (Figure 4.2A). With $\epsilon_{\text{wt,ZDV}} = 0.75$ and $\epsilon_{\text{wt,IDV}} = 0.90$ (the corresponding values used in our monotherapy simulations with each of the two drugs, see Chapter 3), for example, we observed virological failure after ∼3 months (Figure 4.2B) due to mutations resistant to both drugs. In this case, the wild

type was sufficiently suppressed and monotonically declines during the treatment period. However, we also identified regions in the $\epsilon_{\text{wt,ZDV}}$-$\epsilon_{\text{wt,IDV}}$ plane, where treatment failure occurred due to insufficient suppression of the wild type. We classified the treatment as having failed owing to the wild type, if the wild type was the dominant genotype at the point of virological failure (note that, in the presence of drug, the wild type would eventually be out-competed by resistant mutants in all situations).

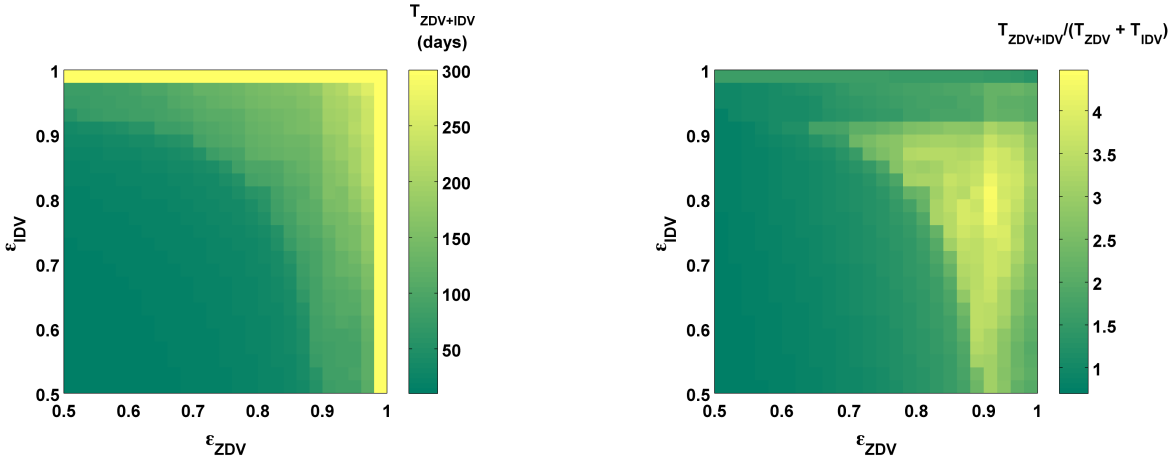

Figure 4.3. Time to viral rebound with ZDV+IDV dual therapy. Left. The time to virological rebound (as defined in Section 4.2) $\text{T}_{\text{ZDV+IDV}}$, under dual therapy with ZDV and IDV, was computed for a range of $\epsilon_{\text{wt,ZDV}}$ and $\epsilon_{\text{wt,IDV}}$ values. **Right.** The time to virological rebound $\text{T}_{\text{ZDV+IDV}}$ under the dual therapy was compared to the sum of the viral rebound times under ZDV and IDV monotherapies. It is seen that over realistic values of drug-efficacies, the drugs behave significantly synergistically.

Such situations of failure with the wild type could indicate insufficient drug pharmacokinetics, a low drug efficacy or poor adherence. Additionally, we also observed that there are combinations of $(\epsilon_{\text{wt,ZDV}}, \epsilon_{\text{wt,IDV}})$, for which failure occurred due to mutations to one of the two drugs (Figure 4.2A). Our model, thus, enabled the prediction of viral evolution and ascertained the genotypic causes of treatment failure under a dual treatment scenario.

Further, we computed the time to virological rebound and observed that the time to failure with the combination is not a simple linear function of the time to failure with the individual drugs (Figure 4.3). In general predictors of treatment outcome under multiple drug therapy (for example, the genetic barriers to resistance, see [135]) are often assumed to be simple functions of the corresponding outcomes with monotherapy. Our results serve as partial evidence for the limitations of such assumptions.

We noted that predicting the treatment outcome from monotherapy with a certain drug might lead to qualitatively different results, as opposed to using a model with multi-drug therapy, even when predicting effects of the same drug. It is easy to see that the $\epsilon_{\text{wt,ZDV}}$ value below which failure with wild type is detected is a function of $\epsilon_{\text{wt,IDV}}$ as well. This reiterates the value of implementing multi-drug treatment regimens in *in silico*

simulations.

We further emphasize that in order to simulate a certain drug combination, our approach needs only clinical data from treatment regimens in which the individual drugs are a part. For instance, in the current example of dual therapy with ZDV and IDV, the estimation of resistance factors and fitness characteristics relied on sparse cross-sectional clinical data from treatment regimens that included ZDV and/or IDV (not necessarily both). Subsequent to this, we were able to simulate the dual therapy and assess genotypic reasons of therapy failure.

4.3 Triple therapy simulation

We next illustrate the application of our model to the antiretroviral triple therapy comprising of lamivudine (3TC), ZDV and IDV. Of these, the first two are NRTIs, while IDV is a PI. This combination was amongst the first multi-drug regimens that were extensively characterized in the late 1990s [96, 222].

The posets of mutations for ZDV and IDV remained the same, while for 3TC, almost complete resistance is conferred by the mutation M184V. This mutation has occupied center-place in many debates regarding viral fitness and treatment interruptions [240,241]. As detailed in Section 4.1, we then constructed the combined genotype lattice of mutations and proceeded to compute the fitness costs and resistance factors of different mutant genotypes. For 184V, we used a resistance factor of 50 and a fitness cost of 0.35 sourced from literature [242]. As before, we assumed no epistasis between the RT and PR regions of the genome. For the two NRTIs, we computed a net drug efficacy. Under an assumption of$\epsilon_{\text{wt,ZDV}} = 0.75$ and $\epsilon_{\text{wt,3TC}} = 0.80$ (chosen as before, to reflect experimental nadir viral loads under monotherapy (see Sections 3.4 and 3.5, Chapter 3), we calculated the combined drug efficacy of ZDV and 3TC using the Bliss-independence model (Eq. (4.4)), $\epsilon_{\text{BI},g}$ and Löwe additivity model (Eq. (4.5)), $\epsilon_{\text{LA},g}$ for the different mutant genotypes $g \in \mathcal{G}$, where $\mathcal{G}$ is the combined genotype lattice of mutations. Jilek et al [239] defined a degree of independence (DI) for a drug combination as follows.

$$\text{DI} = \frac{F_{\text{E}} - F_{\text{LA}}}{F_{\text{BI}} - F_{\text{LA}}}, \tag{4.6}$$

where F_{E}, F_{LA} and F_{BI} denote the logarithmic measures of inhibition $\left(\text{i.e., } F = \log\frac{\epsilon}{1-\epsilon}\right)$ for the experimental data, Löwe additivity and Bliss-independence predictions, respectively. Note that we drop the index g for mutant genotypes here, for clarity. Since all quantities except F_{E} in Eq. (4.6) are known, we then calculated F_{E}, and hence ϵ_{E}, i.e., the combined drug efficacy of ZDV and 3TC, for different mutants.

Our results indicated a sharp decline in viral RNA to levels less than the detection threshold of 50 copies/ml in about 2 months (Figure 4.4C). This level of viral suppression is maintained for ∼32 weeks when the viral load rebounds with mutations resistant to all three drugs. The wild type virus monotonically declines, but is not wholly eradicated (Figure 4.4B). Such archiving of wild type virus is of concern, when treatment interventions such as structured treatment interruptions or induction-maintenance changes are planned.

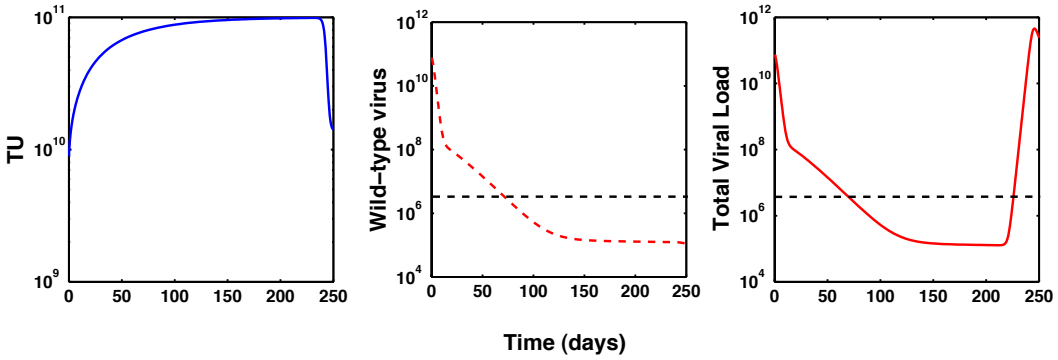

Figure 4.4. Triple therapy with ZDV, 3TC and IDV. The uninfected target cell (TU) levels, the wild type virus levels and the total viral load (all in numbers). The horizontal dashed black lines denote the detection threshold of 50 copies/ml of viral RNA.

4.4 Inter-individual variability

So far, in all our models of viral dynamics, we assumed identical immune system function, drug efficacy and viral fitness parameters across patient populations. In other words, we modelled only the 'average' patient. Of these, viral fitness is the least variable quantity, since, by definition, it depends on the viral mutant genotype, and not the host. By contrast, drug efficacy and immune function are expected to vary considerably within a patient population. In fact, strictly speaking, drug efficacy is a time-dependent quantity since it depends on the pharmacokinetic-pharmacodynamic interplay. We discuss more about this in the next chapter. There are two primary features that have to be remembered when using models such as ours, in predicting treatment response. Firstly, even amongst patients expected to respond identically (a practical impossibility), stochastic effects are presently not captured in our model. These become relevant, especially at low levels of viral load, as in HAART. This would be a potential line of investigation for future work. Secondly, it is well-known that the viral load at the onset of therapy, or the maximal viral load prior to a treatment change is a significant predictor of treatment outcomes (see [135], for example), and this varies widely between patients. At least in treatment naïve patients, one major cause of this variability is the differences in immune function amongst individuals (note the feedback implied here—qualitatively speaking, a poor immune response increases the viral load and lowers the $CD4^+$ T-cell count, thereby affecting the immune system).

We examined the second feature by studying the impact of immune function on our model simulations. To this end, we varied all immune-related parameters in our model (death rates of infected cells and clearance of virions) by a fixed constant k and noted their impact on both the pre-treatment viral load levels and treatment outcome. We illustrate this using IDV monotherapy. With a two-fold ($k = 2$) increase in the clearance rates, we observed viral suppression up to 25 weeks, which is much longer than when $k = 1$ (Figure 4.5). Unless more detailed immune system models are integrated, together with experimental knowledge, it is difficult to make speculations on the realistic range of k. In [203], we have also examined the impact of variability of other model parameters on

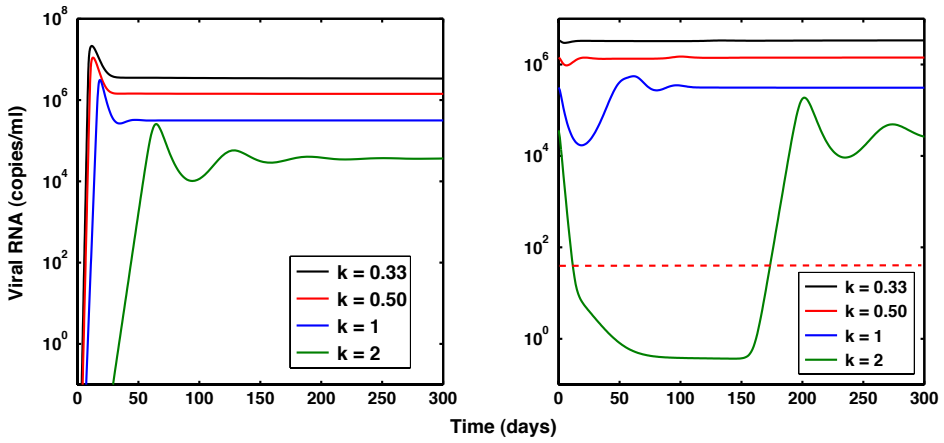

Figure 4.5. Variability in immune function. All immune-system related parameters in the viral dynamics model are varied by a constant factor k. The left panel shows the establishment of viral infection and pre-treatment steady state, while the right panel shows viral dynamics under IDV therapy ($\epsilon_{\text{IDV}} = 0.90$)

our predictions.

4.5 Host-cell targeting

Conventional antiretroviral therapy has aimed at targeting different processes in the viral life cycle. While therapeutic strategies such as the HAART with carefully chosen combinations of drugs, succeed in checking viral proliferation, resistant mutants leading to treatment failure and latently infected cells are recurring threats. To circumvent this menace, recent studies have proposed targeting host-specific factors (see [243] for a detailed review). One particular line of investigation includes the inhibition of host transcription factors like the cyclin dependent kinases (CDKs) [244] using small molecules, thereby preventing the expression of viral proteins. For example, flavopiridol, a drug currently in clinical trials as a chemotherapeutic agent against chronic lymphocytic leukemia, has been shown to possess antiviral properties [68, 103].

In this section, we first briefly review the biology involved in the action of these molecules and then extend our virus dynamics model to accommodate these new drug-types. The calibration of the extended model is then achieved by estimating unknown parameters from *in vitro data* from literature. We then discuss simulation studies performed to mechanistically understand how these molecules act as anti-HIV drugs.

4.5.1 The biology of HIV transcription

The transcription of a gene resulting in mRNA transcripts is a highly complex and tightly regulated process [245]. RNA Polymerase II (RNA Pol II) plays the driving role and HIV makes extensive use of the transcription machinery of the host cell for its replication. Recent studies have resulted in the acknowledgement that the pausing of the RNA Pol II after the initiation of transcription is an important regulatory feature in many cells [246, 247]. After clearing the promoter sequence, the RNA Pol II pauses for a variable

length of time and is assisted by different transcription factors to overcome this block. Amongst them, the positive transcription elongation factor-b (P-TEFb) plays a vital role. We refer to [248] for an excellent, recent review of the detailed mechanisms. In short, P-TEFb is recruited to overcome the hurdle to elongation. Of particular note is the fact that P-TEFb is also an important co-factor for HIV-1. The P-TEFb moiety infact comprises of two proteins, namely CDK9 and CyclinT1 (CycT1). The CDK-Cyc protein complexes have occupied a central role in oncology for the last two decades [249].

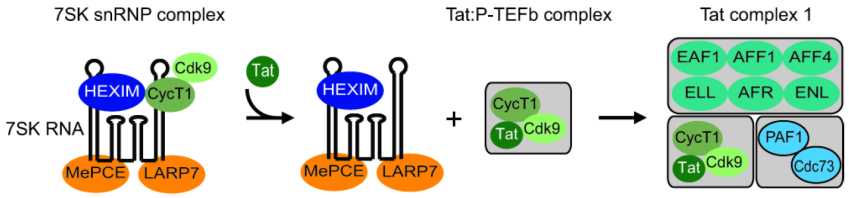

Figure 4.6. The P-TEFb-Tat interaction. P-TEFb (CDK9+Cyc T1) is found complexed with other regulatory molecules such as HEX1M1 and 7SK RNA. Tat recruits P-TEFb to promote transcriptional elongation. The P-TEFb-Tat complex can contain other transcription elongation factors (some of which, like EAF1 and ELL are shown). The above graphic is reproduced from [250] for illustrating the interplay between the viral and host proteins at the transcription stage.

P-TEFb phosphorylates the carboxy-terminal domain of RNA Pol II, and releases it from stalling along the gene to be transcribed. The key to targeting P-TEFb in virology is the Tat-TAR-P-TEFb interplay. Infact, P-TEFb is an attractive target for other viral infections, as it has been implicated in the Epstein-Barr virus associated with Hodgkin's lymphoma and certain other cancers [251]. The *Tat* protein of HIV recruits P-TEFb, which is normally sequestered via complexing with other factors, of which HEX1M1 is an important member. HEX1M1 is a protein that has been known to limit replication of lentiviruses [252]. *Tat* binds to the TAR RNA that is nascently formed during transcription initiation and also to P-TEFb. This relieves the pause in elongation.

CDK inhibitors have been attractive molecules to inhibit P-TEFb for two main reasons—a) they have been extensively characterized in anti-cancer therapy, and b) the IC50 for antiviral effects of many CDKIs is much lower than levels safely tolerated in patients [243]. Amongst the first molecules to be characterized in this regards was flavopiridol. Now under clinical trials (as Alvocidib), flavopiridol (FVP) is a broad-spectrum CDKI inhibiting CDK1, 2 and 4 [253]. In 2000, Price and colleagues demonstrated that FVP inhibits P-TEFb and blocks RNA Pol II mediated transcription *in vitro* [103]. Interestingly, the IC50 of FVP for antiviral action (measured by an infectivity assay) was about 10 nM, much lower than the maximally tolerated 200-400 nM in cancer patients [254]. This study set in motion several others. In 2004, Chiu et al [255] used RNA interference techniques to knock down P-TEFb in HeLa cells and remarkably reported non-lethality in addition to antiviral effects. This observation further strengthened the attractiveness of P-TEFb inhibitors. Another molecule, roscovitine (CYC202) that targets CDK2-CycE by contrast, was also shown to possess anti-HIV properties [69]. The Kashanchi lab has

also performed a virtual screening of 24 CDKIs and identified alsterpaullone as the most potent and selective candidate for antiviral effects, amongst those examined [256]. Most recently, Heredia et al established the *in vivo* efficacy of indirubin 3'-monoxime, a P-TEFb inhibitor, against resistant HIV strains, using humanized mice [257]. However, they also noted the lack of persistent viral suppression with indirubin 3'-monoxime alone as an antiretroviral agent.

To summarize, by checking the clearance of paused RNA Pol II by P-TEFb, the CDKIs represent a promising target for inhibiting HIV replication.

As discussed in Chapter 2, the latent reservoirs of viral infection pose a significant hurdle to the eradication of HIV by evading ART. While in principle, latency is possible prior to integration of the viral DNA into the host genome, the major part of latency in HIV occurs in resting $CD4^+$ T-cells post-integration [258, 259]. To dissect the whole molecular machinery behind the establishment and maintenance of latent reservoirs is a challenging task (see [260] for an overview). Briefly, transcription silencing is known to occur in cells that transit to latency and this is mediated by a host of repressor complexes such as HDACs and histonemethyl transferases. Low levels of *Tat* also contribute to a cell entering latency [72], and this suggests blocks even during transcription initiation. P-TEFb is also thought to influence latency, since molecules such as hexamethylbisacetamide (HMBA) that activate P-TEFb have shown promise as latency activators [261]. Currently, different classes of molecules are being examined for their roles as latency disrupters, including NFκB inducing agents (anti-CD3/CD28 [262]) and HDAC inhibitors (vorinostat [263]).

4.5.2 Extended viral dynamics model incorporating host-targeting molecules

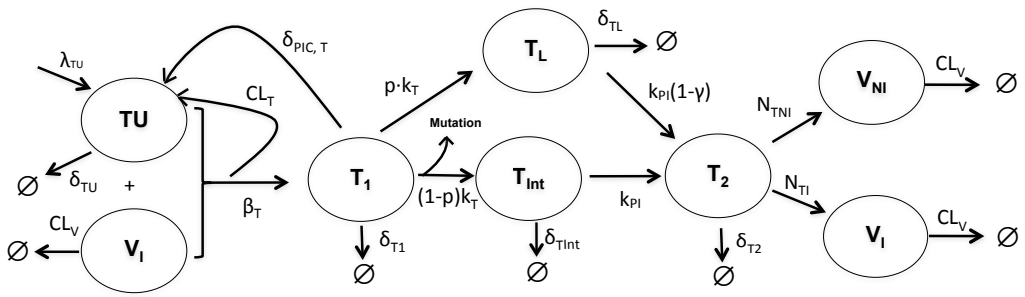

Figure 4.7. Extended viral dynamics model. An extended virus dynamics model to capture the transcription-related events that occur after integration. We included an additional stage (labelled T_{Int}) in our model before the productively infected stage T_2. At this stage, the viral DNA is integrated into the host genome, but is yet to undergo transcription, splicing and extranuclear mRNA export.

We extended our model of viral dynamics to include drugs that inhibit transcription and those that activate latently infected cells. This was achieved by introducing an additional stage in the model T_{Int} (Figure 4.7) where the integration of viral DNA into the host genome is complete, but transcription and further events have not begun. For

simplicity, we first focussed only on the T-cells. The infected cells T_{Int} with integrated viral DNA undergo transcription, appropriate splicing processes of the generated mRNA, followed by their export from the nucleus to the cytoplasmic space. These processes that occur post-integration were lumped and represented by a reaction rate constant k_{PI}. This resulted in the productively infected stage T_2, that is on the cusp of translation, protein assembly and viral release. Note that such extensions of the two-stage infection models have been discussed earlier in [6], although only for qualitative analyses and comparisons with two-stage models.

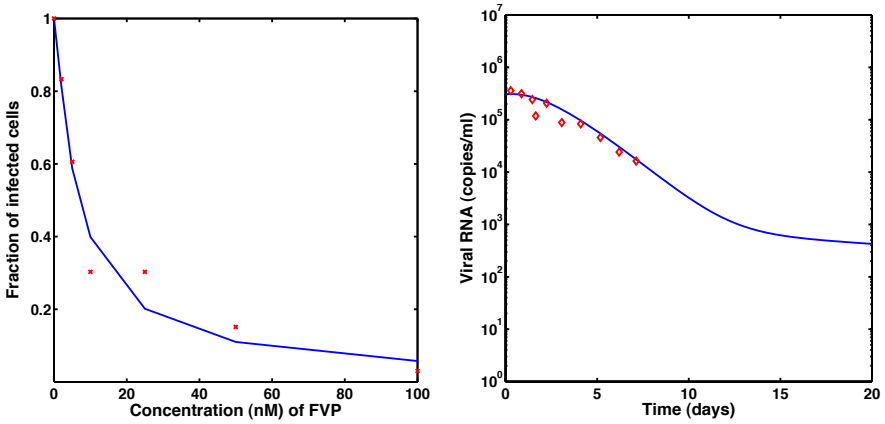

Figure 4.8. Parametrization and validation of extended viral dynamics model. **A.** The extended model in Figure 4.7 was used to estimate the parameter k_{PI} from *in vitro* data based on viral infectivity assays in the presence of FVP (IC50 = 8 nM), **B.** The extended model also performs well in an *in vivo* setting. The data shown are from [114] and represent viral decay under therapy with a PI (a drug efficacy of $\epsilon = 1$ was used.)

We estimated the parameter k_{PI} from *in vitro* data [103]. A strong benefit of our model is it can readily be adapted to an *in vitro* setting after appropriate parametrizations. Owing to the absence of a primary immune system in such an environment, we set all death rates and viral clearances to zero. We fixed the initial number of target cells to be 10^4 and the number of infecting viruses to be 100 (in accordance with the the inoculation protocols used in [103]). The single-cycle replication assay used in [103] measures the number of infected target cells (using a β-galactosidase florescence read-out) after 41 hours. Our equivalent prediction was the number of late-stage infected cells (T_2) after the same time. We performed a least-squares minimization procedure to estimate an optimal k_{PI} of 0.97 day^{-1}. The optimization was straightforward and robust with respect to initial estimates and convergence was noted. The model predictions compared well with experimental data (Figure 4.8A).

As a further test on the validity of the modified model, we simulated the *in vivo* decay in viral load after administration of a protease inhibitor with 100% efficacy, and compared the results to experimental data [114] (Figure 4.8B). Again, our model predictions agreed with data.

4.5.3 Treatment simulations with transcription inhibitors

Having parametrized and validated the model, we next aimed at understanding the action of the transcription inhibitors on the viral replication cycle *in vivo*. We used our extended model, included macrophages (as before) and simulated monotherapy with FVP. We observed that transcription inhibitors like FVP have a rather low impact on nadir levels of viral load (Figure 4.9). In particular, even at high values of drug-efficacy ($\epsilon_{\mathrm{FVP}} \sim 0.95$), the viral load drops by only 1-log unit. This raises questions about *in vivo* efficacies of such drugs.

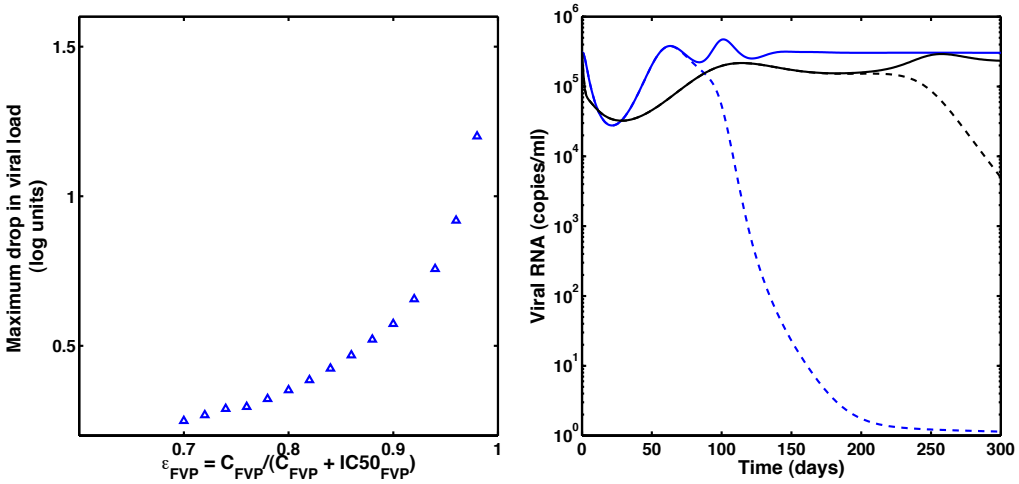

Figure 4.9. Efficacy of flavopiridol *in vivo*. The left panel shows the impact of FVP efficacy (ϵ_{FVP}) on the maximal drop in viral load, while the left panel shows viral load decay with PI monotherapy (blue) and PI together with FVP (black). Drug efficacies of $\epsilon_{\mathrm{PI}}) = 0.9$ and $\epsilon_{\mathrm{FVP}} = 0.88$ (corresponding to ∼8-fold, compared to its IC50 concentration of FVP, in agreement with tolerated doses in clinical trials [254] were used.

A very recent study by Heredia et al [257] noted a drop of 2-log units with another CDK inhibitor drug indirubin 3'-monoxime in humanized mice. To our knowledge, this is the first *in vivo* investigation of the antiviral activity of CDK inhibitors. The authors also note the poor efficacy and remark that such drugs have to be used necessarily with more potent anti-HIV drugs. Nevertheless, a major benefit of such drug classes is the lack of emergence of resistance mechanisms, at least thus far.

4.6 Summary

Multiple drug regimens are the current standard-of-care in the management of HIV infection and disease. Mathematical and statistical models of viral dynamics and mutations are in the process of adapting to clinical requirements in this context. They have a remarkable potential to offer insights into reasons for failure of certain treatment regimens and aid in the rationale choice of potential salvage therapies. Our model of viral dynamics with drug-specific mutation schemes is a first step in this direction. It extends naturally to drug combinations and needs only commonly available sparse data. The generality of the modelling approach also permits the integration of novel drug classes

targeting host-specific factors that are under development. We extended the model to include the action of such molecules and parameterize the model using *in vitro* data. The model performed well in predicting *in vivo* viral load profiles. The analysis of variability amongst infected individuals, the diversity in their immune responses and the need for hybrid deterministic-stochastic simulations present future lines of investigation.

Chapter 5

Pharmacokinetic-pharmacodynamic interplay in HIV therapy

5.1 Introduction

In this chapter, we focus on a key aspect of antiretroviral drug development and clinical therapy, namely drug pharmacokinetics. Pharmacokinetics refers to the relationship between drug input (with its associated features such as dose, dosing interval, dosage form etc) and the concentration attained in the body with time [264]. Loosely speaking, pharmacokinetics (PK) has been characterized as the study of what the body does to the drug (as opposed to pharmacodynamics, which can be viewed as what the drug does to the body). In the context of HIV therapy, time-dependent changes in drug concentration may impact viral suppression and hence influence clinical outcome. The long-term nature of HIV therapy also raises questions concerning drug accumulation. Understanding drug PK associated with multiple dosing is thus vital for the design and development of new drug candidates, and to devise safe and efficacious dosage regimens. It is not uncommon in literature to report one or the other of several possible measures of accumulation or half-life. We illustrate how this can be misleading when such measures are taken in isolation, especially with drugs exhbiting multi-phasic pharmacokinetic behaviour, and can sometimes result in seemingly unrelated or even conflicting statements.

We begin with a short introduction to compartment PK models and define various notions of drug accumulation and half life. We then present a concise framework that links key PK characteristics of multiple dosing to the parameters of the underlying compartment models. Our framework provides an integrated understanding of different drug accumulation and half-life measures. We illustrate its utility by reconciling two apparently conflicting remarks in literature on the pharmacokinetics of the HIV integrase inhibitor raltegravir.

We explore the impact of PK on viral suppression by coupling PK models to simple models of viral dynamics. We then incorporate the PK of ZDV in our viral dynamics model with drug-specific mutation schemes to examine the impact of fluctuating concentrations of ZDV on its antiviral effect. Finally, we conclude with an outlook for further work in these directions.

5.2 Compartment PK models

Pharmacokinetic data can be modelled using several approaches and compartmental PK analysis is both standard and ubiquitous. We refer to [265] for an extensive treatment

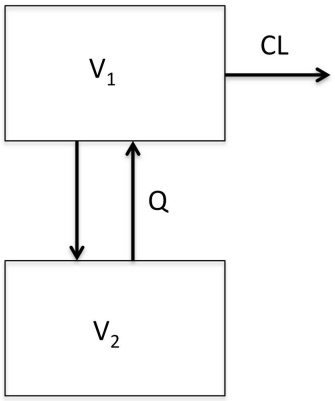

Figure 5.1. A two-compartment PK model.

of compartment-based PK modelling approaches. Here, we only state the mathematical framework for such models that enables us to define and derive key PK characteristics.

A one-compartment PK model describes the decrease in concentration of drug after its administration by a linear first-order ordinary differential equation (ODE).

$$V \cdot \frac{\mathrm{d}}{\mathrm{dt}} C = -\mathrm{CL} \cdot C. \tag{5.1}$$

Here, C denotes the drug-concentration, while V is the volume of the compartment. CL is the linear clearance of the drug.

A biphasic decline in drug concentration is frequently seen in PK studies, which can be described by a two-compartment model (Figure 5.1). This is mathematically specified by a linear system of coupled ODEs.

$$\begin{aligned} V_1 \cdot \frac{\mathrm{d}}{\mathrm{dt}} \mathrm{C}_1 &= Q \cdot (C_2 - C_1) - \mathrm{CL} \cdot C_1 \\ V_2 \cdot \frac{\mathrm{d}}{\mathrm{dt}} \mathrm{C}_2 &= Q \cdot (C_1 - C_2). \end{aligned} \tag{5.2}$$

Here, C_1 and C_2 are the drug concentrations in the two compartments (frequently referred to as the central and peripheral compartments). The parameter Q refers to the inter-compartmental clearance, while V_1 and V_2 are the compartmental volumes.

A generalization to multi-compartment models is readily conceivable. In this case, the mathematical specification would still be a system of linear ODEs, as long as the clearance (and absorption, where this is modelled) mechanisms remain linear. Non-linear clearances (for example, saturable) are possible, especially for monoclonal antibodies [266]. In this chapter, we concern ourselves only with linear PK models. We next present some nomenclature and definitions of key PK characteristics.

5.2.1 Volume of distribution

The volume of distribution is a standard parameter used in characterizing the pharmacokinetic behaviour of drugs. It was originally defined by Dominguez [267] as the hypothetical volume of body fluids dissolving the drug substance at the same concentration as that in the plasma. As the kinetics of drug disposition in the body is a dynamic process and the plasma concentration itself is time varying, there are different ways of formulating this volume. The steady state volume of distribution [268] V_{ss} is defined as the ratio of the amount of drug A_{ss} in the body and the drug concentration in plasma C_{ss} at steady state conditions.

$$V_{\text{ss}} = \frac{A_{\text{ss}}}{C_{\text{ss}}}. \tag{5.3}$$

Another quantity of frequent interest in the study of the pharmacokinetic behaviour of a drug is its terminal volume of distribution V_z. This is defined as the ratio of the amount of drug in the body A_z and its plasma concentration C_z during the final phase of elimination.

$$V_z = \frac{A_z}{C_z}. \tag{5.4}$$

5.2.2 Accumulation factors

A drug can be administered by different routes, for example, as intravenous (i.v.) bolus rally. Drug PK after a single dose is extensively characterized in the early stages of drug development. In the later stages of development and naturally in the clinical setting, multiple dosing (at certain dosing intervals) is a norm (at least in HIV therapy). Defining, computing and understanding measures of drug accumulation and half-lifes, therefore becomes relevant in such situations. We refer to [269] and references therein for many of the following definitions.

The AUC accumulation factor R_{AUC} represents the increase in exposure after multiple dosing. It is defined as

$$R_{\text{AUC}} = \frac{\text{AUC}_{\text{ss},0\to\tau}}{\text{AUC}_{0\to\tau}}, \tag{5.5}$$

where $\text{AUC}_{0\to\tau}$ denotes the area under the plasma concentration-time curve from time $t = 0$ to $t = \tau$ after the first dose, and $\text{AUC}_{\text{ss},0\to\tau}$, the corresponding area over one dosing interval in the steady state regime.

The peak accumulation factor R_{peak} is defined as

$$R_{\text{peak}} = \frac{C_{\text{ss,peak}}}{C_{\text{peak}}}, \tag{5.6}$$

where $C_{\text{ss,peak}}$ and C_{peak} denote the peak plasma concentrations at steady state and after the first dose, respectively. The steady state and single dose peak concentrations are attained at times $t_{\text{ss,peak}}$ and t_{peak}, respectively, after the previous dose. Hence, $C_{\text{ss,peak}} = C_{\text{ss}}(t_{\text{ss,peak}})$ and $C_{\text{peak}} = C(t_{\text{peak}})$, with $C_{\text{ss}}(t)$ and $C(t)$ being the concentration-time

profiles at steady state and after first dose, respectively. For i.v. bolus administration, $t_{\text{ss,peak}} = t_{\text{peak}} = 0$, while for oral administration, $0 < t_{\text{ss,peak}} < t_{\text{peak}}$ (see Section 5.3.3.).

Analogously, the trough accumulation factor R_{trough} can be defined as

$$R_{\text{trough}} = \frac{C_{\text{ss,trough}}}{C_{\text{trough}}}, \tag{5.7}$$

where $C_{\text{ss,trough}}$ and C_{trough} denote the trough concentrations at steady state and after the first dose, respectively. Note that, we have, by definition, $C_{\text{ss,trough}} = C_{\text{ss}}(\tau)$ and $C_{\text{trough}} = C(\tau)$.

Together with AUC, peak and trough concentrations at steady-state are commonly used as summary measures of exposures (and to compare exposures across different populations), and the accumulation factors provide an easy means of quantifying how exposures change in a multiple-dose setting, relative to a single dose.

The peak-to-trough ratio PT_{ss} at steady state conditions is defined as

$$\text{PT}_{\text{ss}} = \frac{C_{\text{ss,peak}}}{C_{\text{ss,trough}}}. \tag{5.8}$$

5.2.3 Half-lifes

The terminal half life, a measure of how long the drug takes to leave the body via its slowest process of elimination, can be written as

$$t_{1/2} = \frac{\ln 2}{\lambda_z}, \tag{5.9}$$

where λ_z is the slope of the terminal phase of elimination. The (plasma) terminal half-life of a drug can then be regarded as the time to reduce the plasma concentration by a factor 1/2 after reaching pseudo-equilibrium. It has been observed that the terminal half life is the most reported, yet commonly misinterpreted pharmacokinetic parameter [270]. The clinical utility of this quantity, for example, lies in selecting appropriate dosing intervals for drugs, as it dictates the degree of drug accumulation and time to reach equilibrium in multiple dosing regimens.

Other kinds of half-lifes have also been defined and characterized in literature. The effective half-life t_{eff} [271] is defined in terms of the AUC accumulation factor R_{AUC} as

$$t_{\text{eff}} = \frac{\log(2)}{k_{\text{eff}}}, \tag{5.10}$$

where the effective rate constant k_{eff} is implicitly defined by

$$\frac{1}{1 - \exp(-k_{\text{eff}}\tau)} = R_{\text{AUC}}. \tag{5.11}$$

Unlike the terminal half life $t_{1/2}$, the effective half-life t_{eff} depends on the dosing interval τ, i.e., $t_{\text{eff}} = t_{\text{eff}}(\tau)$.

The effective non-compartmental analysis (NCA) half-life $t_{1/2,\mathrm{NCA}}$ is defined as

$$t_{1/2,\mathrm{NCA}} = \log(2) \cdot \mathrm{MRT}, \tag{5.12}$$

where MRT is the mean residence time, defined as MRT = AUC/AUMC with AUMC being the area under the first moment curve (see section 2.4.2 in [272]).

The operational half-life $t_{1/2,\mathrm{op}}$ [269] is defined on the basis of the peak accumulation ratio R_{peak}. It is equal to that dosing interval where the peak concentration at steady-state is twice the peak concentration after the first dose *and* where the fall-off to the trough from this peak steady-state concentration is consistent with this half-life. In addition, the authors in [269] also observe graphically that when the dosing interval $\tau = t_{1/2,\mathrm{op}}$, the peak concentration at steady-state is twice the trough-concentration. We later demonstrate this to be a corollary of the definition of operational half-life.

5.2.4 The interplay of accumulation factors, half-lifes and dosing interval

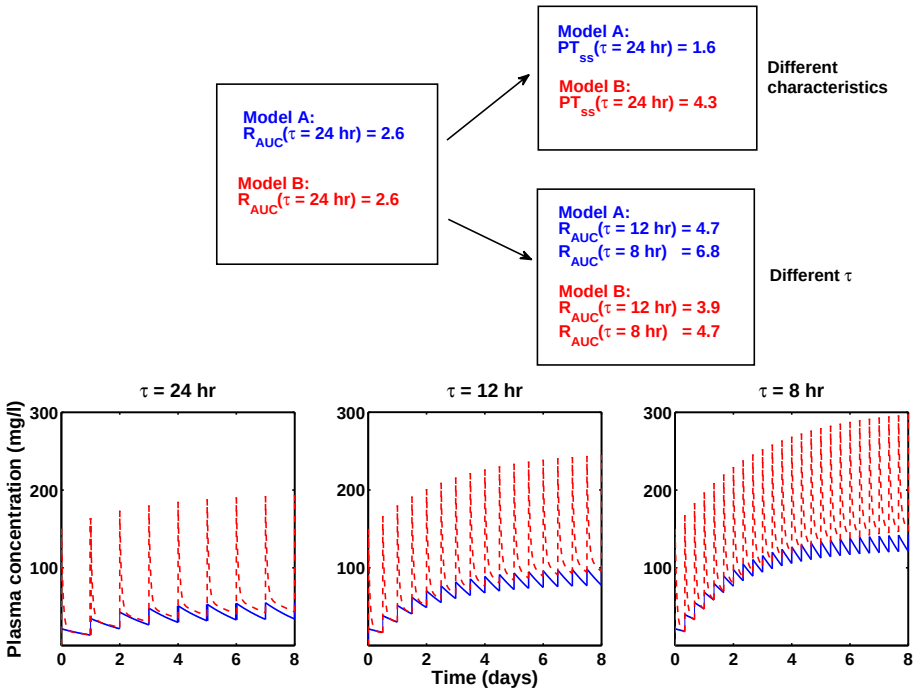

Figure 5.2. Key characteristics of compartment models differ amongst themselves and with dosing interval. Top: Models A (blue) and B (red) are one and two-compartment models with i.v. bolus administration. Model A has parameters $V_{\mathrm{ss}} = 14$ L and CL $= 0.28$ L/hr, while model B has $V_1 = 2$ L ,$V_2 = 10$ L, $Q = 1.1$ L/hr and CL $= 0.2$ L/hr. The AUC accumulation factor R_{AUC} is identical for both models when the dosing interval $\tau = 24$ hr (once-daily dosing). However, the peak-to-trough ratio at steady state $\mathrm{PT}_{\mathrm{ss}}$ for the models are markedly different. Further, the equality in R_{AUC} itself ceases to hold when τ is varied. **Bottom:** The concentration-time profiles for the models clearly shows the difference in PK behaviour, in spite of identical AUC accumulation factors at a certain dosing interval.

For a general multi-compartment model, the accumulation factors, in general, depend on the dosing interval, in addition to the model parameters. Although, each of these factors, individually, can be computed explicitly once the model is completely specified, the complicated functional dependence (for example, mathematically, the computation of terminal half-life in a linear multi-compartment model is an eigenvalue problem and a closed form of eigenvalues for the linear system of ODEs can rapidly become complex!) makes any interpretation or prediction of relationships difficult. For illustration, in Figure 5.2, we show how two models with identical AUC accumulation factors can have remarkably different steady-state peak-to-trough ratios. Further, the initial degeneracy in the AUC accumulation ratios itself lifts, when the dosing interval is varied. This clearly illustrates the inadequacy of using or reporting one accumulation parameter to analyze different features in PK models.

There are several examples of anti-retroviral drugs where an isolated examination of one or the other accumulation factor or half-life could potentially be misleading. For example, the authors in [269] point out how Iwamoto et al [15] report little accumulation of raltegravir (with AUC and peak accumulation factors determined to be 1.06 and 1.0 respectively) in a twice-daily multiple dose study, but simultaneously calculate a long terminal half-life of 10-12 hours (that is suggestive of accumulation). Interestingly, for a different integrase inhibitor S/GSK1349572, a comparable terminal half-life of 13-15 hours is reported, but with moderate accumulation factors of up to 1.5 [273]. Therefore, to reconcile such unrelated results and to establish unequivocal relationships (or a lack of them!) between different measures of half-lifes and accumulation, there is a need to examine these quantities in an integrated framework.

Additionally, a linear 1-compartment PK model with i.v. bolus administration is typically used to illustrate the concepts of multiple dosing and to introduce key characteristics like half-lifes, accumulation indices, peak-to-trough ratio etc, see, e.g., [264]. However, the ability to translate the 1-compartment i.v. bolus case PK model to more common 2- or multi-compartment PK models with i.v. or extravascular drug administration, is limited, and these attempts can be very misleading. Brocks et al [274] recognize this need and provide some characterizations of accumulation factors and half-lifes for 1-compartment oral administration and for a 2-compartment model with i.b. bolus administration.

In the next section, we develop a framework that shows how key characteristics of multiple dosing in multi-compartment models are linked to the different model parameters. Our framework enables us to integrate seemingly unrelated previous results —e.g., on effective and operational half-lifes, or the relationship between the terminal volume of distribution and the steady state volume of distribution into this framework. We accomplish this by linking the solution of multi-compartment PK to sums of solutions of 1-compartment PK. This allows us to state key characteristics of multiple dosing of multi-compartment models as weighted sums of the key characteristics of multiple dosing of associated 1-compartment models with i.v. bolus administration.

5.3 An integrated framework to derive characteristics of multiple dosing regimens

We focus on key accumulation characteristics and half-lifes derived from the plasma concentration profiles after single dose $C(t)$ and steady-state profiles during multiple dose $C_{\mathrm{ss}}(t)$. We review the results of 1-compartment model with i.v. bolus administration, and use this to establish notation. We then present results for 2-compartment model with i.v.bolus administration, where we observe the possibility of decomposition of all characteristics into associated weighted one-compartment models. We then extend the framework for oral administration.

5.3.1 1-compartment PK model with i.v. bolus administration revisited

Given the volume of distribution V_{ss} and the total plasma clearance CL, the rate of change of the plasma (central) concentration C after a first i.v. bolus dose D is governed by the ODE

$$V_{\mathrm{ss}}\frac{\mathrm{d}}{\mathrm{d}t}C = -\mathrm{CL}\cdot C. \tag{5.13}$$

with initial condition $C(0) = D/V_{\mathrm{ss}}$. The analytical solution of the plasma concentration is given as

$$C(t) = L\cdot\exp(-\lambda t), \tag{5.14}$$

with initial concentration $L = D/V_{\mathrm{ss}}$ and rate constant $\lambda = \mathrm{CL}/V_{\mathrm{ss}}$. In multiple dosing, under steady-state conditions with dosing interval τ, the analytical solution at time t (relative to the last dose) can be given as

$$C(t) = R_\lambda L\cdot\exp(-\lambda t), \tag{5.15}$$

where $R_\lambda = 1/(1-\exp(-\lambda\tau))$ denotes an index of accumulation. Note that $R_\lambda = R_\lambda(\tau)$ is a function of the dosing interval τ. Thus, the plasma concentration in the steady state multiple dosing regime is just a multiple of the single dosing plasma concentration, with a scaling factor equal to the accumulation index R_λ.

From eqs. (5.14) and (5.15), several key characteristics of multiple dosing can be determined. The terminal half-life is given by

$$t_{1/2} = \frac{\log(2)}{\lambda}. \tag{5.16}$$

The AUC, peak and trough accumulation factors are all identical and given by

$$R_{\mathrm{AUC}} = R_{\mathrm{peak}} = R_{\mathrm{trough}} = \frac{1}{1-\exp(-\lambda\tau)}, \tag{5.17}$$

where all three accumulation ratios are functions of the dosing interval τ. Combining eqs. (5.16)-(5.17) and the definition of the accumulation index, we obtain $R_\lambda = 1/(1-\exp(-\log(2)\tau/t_{1/2}))$ so that $R_\lambda = 2$ for $\tau = t_{1/2}$. In other words, from a graphic of R_λ versus τ, we may easily read off the half-life: it is that value of τ, for which R_λ equals 2

(i.e., the value of the abscissa when the ordinate equals 2). Finally, the peak-to-trough ratio under steady state is given by

$$\mathrm{PT}_{\mathrm{ss}} = \exp(\lambda\tau). \tag{5.18}$$

Note that none of the key characteristics introduced above depend on the dose (since the factor L cancels out)! We highlight three unique features of the 1-compartment model with i.v. bolus administration:

1. half-life, accumulation factors and peak-to-trough ratio are all expressed in terms of a single, model-specific quantity λ;
2. all three accumulation factors are identical;
3. knowing one of the above key characteristics of multiple dosing allows one to determine λ and therefore all other key characteristics.

None of the three features continue to hold for multi-compartment models.

5.3.2 2-compartment PK model with i.v. bolus administration

Given the central and peripheral volumes V_1 and V_2, and the distribution and total plasma clearances Q and CL, the rate of change of the plasma (central) and peripheral concentrations C_1 and C_2 after a single i.v. bolus dose D is governed by the system of ODEs (5.2) with initial conditions $C_1(0) = D/V_{\mathrm{ss}}$ and $C_2(0) = 0$. The analytical solution of the plasma concentration is given by

$$C_1(t) = A \cdot L\exp(-\alpha t) + B \cdot L\exp(-\beta t), \tag{5.19}$$

with $L = D/V_{\mathrm{ss}}$, coefficients $A = (\alpha - Q/V_2)/(\alpha - \beta)$; $B = (Q/V_2 - \beta)/(\alpha - \beta)$; and rate constants $\beta = \mathrm{CL}/V_{\mathrm{z}}$ and $\alpha \cdot \beta = (Q/V_2)(\mathrm{CL}/V_1)$, where V_{z} denotes the terminal volume of distribution. By definition, $\alpha > Q/V_2 > \beta$.

We make the following simple, but key observation (Figure 5.3 top): one may interpret the plasma concentration C_1 in eq. (5.19) as the weighted sum of the solutions of two 1-compartment PK models:

(a) with initial concentration L, rate constant α and weighting factor A; and

(b) with initial concentration L, rate constant β and weighting factor B.

This simple observation enables us to leverage on the 1-compartment theory. We refer to these models as the 1-compartment models associated with the 2-compartment model. For each of the 1-compartment models, we determine the key characteristics as follows.

(a) $t_{1/2,\alpha} = \log(2)/\alpha$, $R_{\mathrm{AUC},\alpha} = R_{\mathrm{peak},\alpha} = R_{\mathrm{trough},\alpha} = R_\alpha$, and $\mathrm{PT}_{\mathrm{ss},\alpha} = \exp(\alpha\tau)$, where $R_\alpha = 1/(1 - \exp(-\alpha\tau))$ denotes the accumulation index;

(b) $t_{1/2,\beta} = \log(2)/\beta$, $R_{\mathrm{AUC},\beta} = R_{\mathrm{peak},\beta} = R_{\mathrm{trough},\beta} = R_\beta$ and $\mathrm{PT}_{\mathrm{ss},\beta} = \exp(\beta\tau)$, where $R_\beta = 1/(1 - \exp(-\beta\tau))$ denotes the accumulation index.

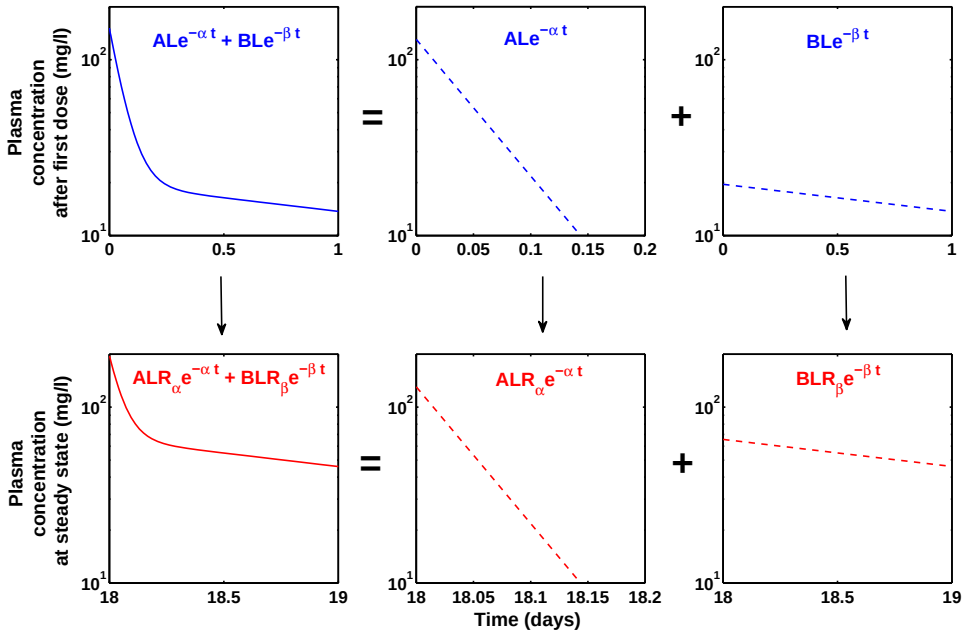

Figure 5.3. Decomposition of multi-compartment PK profiles into associated one-compartment profiles in multiple dosing settings. Top: A two-compartment PK profile after the first dose can be decomposed into associated one-compartment profiles. **Bottom:** A similar decomposition can also be carried out for the PK profile at steady-state conditions during multiple dosing. Notably, the associated one-compartment profiles are scaled versions of the corresponding single-dose profiles.

Under steady state multiple dosing conditions with dosing interval τ, the plasma concentration of the 2-compartment PK model at time t (relative to the last dose) can be given by

$$C_1(t) = A \cdot R_\alpha L \exp(-\alpha t) + B \cdot R_\beta L \exp(-\beta t), \tag{5.20}$$

with accumulation indices R_α and R_β defined above. In this case, the plasma concentration in the steady state multiple dosing regime is *not* just a scaled version of the single dosing plasma concentration. Notably, however, the associated one-compartment profiles reveal scaling by the corresponding accumulation ratios (Figure 5.3 bottom).

From eqs. (5.19) and (5.20), the following key characteristics of multiple dosing can be determined. The terminal half-life is $t_{1/2} = \log(2)/\beta$ and can thus be written as

$$t_{1/2} = 0 \cdot t_{1/2,\alpha} + 1 \cdot t_{1/2,\beta}. \tag{5.21}$$

Based on eqs. (5.5), (5.19) and (5.20), we obtain the AUC accumulation factor R_{AUC}

as follows.

$$\begin{aligned} R_{\mathrm{AUC}} &= \frac{\mathrm{AUC}_{\mathrm{ss},0\to\tau}}{\mathrm{AUC}_{0\to\tau}} \\ &= \frac{A\cdot \mathrm{AUC}_{\mathrm{ss},0\to\tau,\alpha} + B\cdot \mathrm{AUC}_{\mathrm{ss},0\to\tau,\beta}}{A\cdot \mathrm{AUC}_{0\to\tau,\alpha} + B\cdot \mathrm{AUC}_{0\to\tau,\beta}} \\ &= \frac{A\cdot R_\alpha \mathrm{AUC}_{0\to\tau,\alpha} + B\cdot R_\beta \mathrm{AUC}_{0\to\tau,\beta}}{A\cdot \mathrm{AUC}_{0\to\tau,\alpha} + B\cdot \mathrm{AUC}_{0\to\tau,\beta}} \\ &= \frac{A\cdot R_\alpha L/\alpha R_\alpha^{-1} + B\cdot R_\beta L/\alpha R_\beta^{-1}}{A\cdot L/\alpha R_\alpha^{-1} + B\cdot L/\alpha R_\beta^{-1}} \\ &= \frac{A/\alpha + B/\beta}{A/\alpha\cdot R_\alpha^{-1} + B/\alpha\cdot R_\beta^{-1}}, \end{aligned}$$

where the subscripts α and β indicate that the AUC is determined with respect to the corresponding 1-compartment model. Taking the inverse of the above relation results in

$$R_{\mathrm{AUC}}^{-1} = \frac{A/\alpha}{A/\alpha + B/\beta}\, R_\alpha^{-1} + \frac{B/\beta}{A/\alpha + B/\beta}\, R_\beta^{-1}. \tag{5.22}$$

Calculating on similar lines, the peak and trough accumulation factors are determined as

$$R_{\mathrm{peak}} = \frac{A}{A+B}\cdot R_\alpha + \frac{B}{A+B}\cdot R_\beta, \tag{5.23}$$

and

$$\begin{aligned} R_{\mathrm{trough}} &= \frac{A\exp(-\alpha\tau)}{A\exp(-\alpha\tau) + B\exp(-\beta\tau)}\, R_\alpha + \\ &\quad \frac{B\exp(-\beta\tau)}{A\exp(-\alpha\tau) + B\exp(-\beta\tau)}\, R_\beta. \end{aligned} \tag{5.24}$$

Interestingly, under the usual condition of $A > B > 0$, it can be shown that

$$R_{\mathrm{peak}} < R_{\mathrm{trough}}, \tag{5.25}$$

To prove the above inequality, we note that under the assumption of $A > B > 0$:

$$\frac{B}{A+B} < \frac{B}{A\exp(-(\alpha-\beta)\tau) + B} = \frac{B\exp(-\beta\tau)}{A\exp(-\alpha\tau) + B\exp(-\beta\tau)},$$

since by definition $\alpha > \beta$, implying $\exp(-(\alpha-\beta)\tau) < 1$. As $R_{\mathrm{peak},\alpha} = R_{\mathrm{trough},\alpha} = R_\alpha < R_\beta = R_{\mathrm{peak},\beta} = R_{\mathrm{trough},\beta}$, the inequality (5.25) follows.

The peak-to-trough ratio under steady state multiple dosing conditions is determined as

$$\mathrm{PT}_{\mathrm{ss}}^{-1} = \frac{AR_\alpha}{AR_\alpha + BR_\beta}\, \mathrm{PT}_{\mathrm{ss},\alpha}^{-1} + \frac{BR_\beta}{AR_\alpha + BR_\beta}\, \mathrm{PT}_{\mathrm{ss},\beta}^{-1}. \tag{5.26}$$

We emphasize that the peak accumulation factor and the peak-to-trough ratio are derived under the implicit assumption that the time at which the peak is attained satisfies $t_{\mathrm{peak}} = 0$. This is the case for i.v. bolus administration, while it does not hold for the case of oral administration (details follow in the next sub-section). Again, we note that none

of the key characteristics depend on the dose.

We highlight the following features of the 2-compartment PK model with i.v. bolus administration:

1. the key characteristics of multiple dosing for a 2-compartment model depend on the key characteristics of the two associated 1-compartment models;

2. the relative impact of each of these two 1-compartment key characteristics depends on weighting factors; these differ between the key characteristics;

3. in general, knowledge of one of the above key characteristics of multiple dosing does *not* allow one to predict some other key characteristics.

These observations are not restricted to the 2-compartment model and naturally generalize to multi-compartment PK models. This also includes the case of a 1-compartment PK model with oral administration, since it can be formulated as a 2-compartment PK model.

5.3.3 1-compartment PK model with p.o. administration

Oral administration of a drug is a popular dosage route and is referred to as p.o. administration. Here, the absorption kinetics of a drug after ingestion is generally described by two parameters, a gastro-intestinal (GI) rate constant $k_{\text{p.o.}}$ and bioavailability F_{bio} (interpretation of these parameters follows later). Given a volume of distribution V_{ss}, a total plasma clearance CL, the rate of change of the plasma (central) concentration C_1 and the amount in the GI tract A_2 after a single p.o. dose D is described by the system of ODEs

$$V_{\text{ss}}\frac{\mathrm{d}}{\mathrm{d}t}C_1 = -\text{CL}\cdot C + F_{\text{bio}}k_{\text{p.o.}}\cdot A_2 \tag{5.27}$$

$$\frac{\mathrm{d}}{\mathrm{d}t}A_2 = -k_{\text{p.o.}}\cdot A_2, \tag{5.28}$$

with initial conditions $C_1(0) = 0$ and $A_2(0) = D$. The analytical solution can be written down as

$$C_1(t) = L\frac{k_{\text{p.o.}}}{k_{\text{p.o.}}-\lambda}\big(\exp(-\lambda t) - \exp(-k_{\text{p.o.}}t)\big), \tag{5.29}$$

with $L = F_{\text{bio}}D/V_{\text{ss}}$ and rate constant $\lambda = \text{CL}/V_{\text{ss}}$. We assume $k_{\text{p.o.}} \neq \lambda$ (otherwise see [275]).

Under steady state multiple dosing conditions with dosing interval τ, the analytical solution at time t (relative to the last dose) is given by

$$C_1(t) = L\frac{k_{\text{p.o.}}}{k_{\text{p.o.}}-\lambda}\big(R_\lambda\exp(-\lambda t) - R_{k_{\text{p.o.}}}\exp(-k_{\text{p.o.}}t)\big), \tag{5.30}$$

with accumulation indices $R_{k_{\text{p.o.}}} = 1/(1-\exp(-k_{\text{p.o.}}\tau))$ and $R_\lambda = 1/(1-\exp(-\lambda\tau))$.

Depending on the magnitudes of $k_{\text{p.o.}}$ and λ, we distinguish two scenarios:

(i) Common case: $k_{\text{p.o.}} > \lambda$. We defined $\alpha = k_{\text{p.o.}}$, $A = -k_{\text{p.o.}}/(k_{\text{p.o.}}-\lambda)$, $B = -A$ and $\beta = \lambda$;

(ii) Flip-flop case: $k_{\text{p.o.}} < \lambda$. We defined $\alpha = \lambda$, $A = -k_{\text{p.o.}}/(\lambda - k_{\text{p.o.}})$, $B = -A$ and $\beta = k_{\text{p.o.}}$.

Note that in both scenarios, $A < 0$ and $B > 0$. Again, we associate with eqs. (5.29) and (5.30), two 1-compartment models: (a) with initial concentration L, rate constant α and weighting factor A; and (b) with initial concentration L, rate constant β and weighting factor B. This formal analogy allows us again to write key characteristics of multiple dosing for the 1-compartment model with p.o. administration as weighted sums of the corresponding key characteristics of the two associated 1-compartment models. The only difference being, that the times of peak concentration $t_{\text{ss,peak}}$ and t_{peak} are different from zero. For explicit calculation of these times, we refer to [276]. They are given by

$$t_{\text{peak}} = \frac{\log(k_{\text{p.o.}}) - \log(\lambda)}{k_{\text{p.o.}} - \lambda} \tag{5.31}$$

and, defining the shift in steady state

$$\Delta_{\text{ss,peak}} = \frac{\log(R_{k_{\text{p.o.}}}) - \log(R_\lambda)}{k_{\text{p.o.}} - \lambda}, \tag{5.32}$$

we have $t_{\text{ss,peak}} = t_{\text{peak}} + \Delta_{\text{ss,peak}}$.

Note that for both the common and the flip-flop scenario, the shift is negative, such that $t_{\text{ss,peak}} < t_{\text{peak}}$, i.e., the peak concentration is reached earlier under steady state multiple dosing condition compared to the first dose (in both cases, the time is relative to last dose).

Exploiting the association between the 1-compartment PK model with p.o. dosing and two 1-compartment models (as discussed above), one can easily determine the key characteristics of multiple p.o. dosing from eqs. (5.21)-(5.26), taking into account the differences in peak times at steady state dosing $t_{\text{ss,peak}}$ and at single dose t_{peak}. This nicely illustrates the usefulness of our proposed framework. For the common scenario ($k_{\text{p.o.}} > \lambda$), we explicitly state the resulting key characteristics below, where we further simplify the equations by exploiting $B = -A$.

The AUC accumulation factor is given by

$$R_{\text{AUC}} = \frac{k_{\text{p.o.}} - \lambda}{k_{\text{p.o.}}(1 - \exp(-\lambda\tau)) - \lambda(1 - \exp(-k_{\text{p.o.}}\tau))}. \tag{5.33}$$

The trough and peak accumulation factors can also be derived as

$$R_{\text{trough}} = \frac{\frac{\exp(-\lambda\tau)}{1-\exp(-\lambda\tau)} - \frac{\exp(-k_{\text{p.o.}}\tau)}{1-\exp(-k_{\text{p.o.}}\tau)}}{\exp(-\lambda\tau) - \exp(-k_{\text{p.o.}}\tau)}. \tag{5.34}$$

$$R_{\text{peak}} = \frac{\frac{\exp(-\lambda(t_{\text{ss,peak}}))}{1-\exp(-\lambda\tau)} - \frac{\exp(-k_{\text{p.o.}}(t_{\text{ss,peak}}))}{1-\exp(-k_{\text{p.o.}}\tau)}}{\exp(-\lambda t_{\text{peak}}) - \exp(-k_{\text{p.o.}} t_{\text{peak}})}. \tag{5.35}$$

These accumulation factors are identical to the formulae given in eq. A-9 in [274]. Finally, the peak-to-trough ratio PT_{ss} in steady state can be determined from eqs. (5.29)-

(5.30) as

$$\mathrm{PT}_{\mathrm{ss}} = \frac{AR_\lambda \exp(-\lambda(t_{\mathrm{ss,peak}})) + BR_{k_{\mathrm{p.o.}}} \exp(-k_{\mathrm{p.o.}}(t_{\mathrm{ss,peak}}))}{AR_\lambda \exp(-\lambda\tau) + BR_{k_{\mathrm{p.o.}}} \exp(-k_{\mathrm{p.o.}}\tau)}. \tag{5.36}$$

For the flip-flop scenario, the corresponding equations can be similarly derived.

As in [270], we emphasize that $k_{\mathrm{p.o.}}$ includes the processes of GI transition, absorption, and metabolism in the gut as well as in the liver. It quantifies the rate of loss of the drug that can potentially be absorbted into the systemic circulation. In terms of the fraction excreted unchanged in feces E_{feces}, the metabolic extraction of the gut E_{gut} and the hepatic extraction ratio E_{hep}, we may quantify the different processes as follows: $(1 - E_{\mathrm{feces}})k_{\mathrm{p.o.}}$ characterizes the rate of absorption into the gut wall; $E_{\mathrm{gut}}(1-E_{\mathrm{feces}})k_{\mathrm{p.o.}}$ characterizes the rate of gut wall metabolism, while $(1 - E_{\mathrm{gut}})(1 - E_{\mathrm{feces}})k_{\mathrm{p.o.}}$ characterizes the absorption into the portal vein. Finally, $(1 - E_{\mathrm{hep}})(1 - E_{\mathrm{gut}})(1 - E_{\mathrm{feces}})k_{\mathrm{p.o.}}$ characterizes the rate of absorption into the systemic circulation. Note that the latter is identical to $F_{\mathrm{bio}}k_{\mathrm{p.o.}}$, since by definition $F_{\mathrm{bio}} = (1 - E_{\mathrm{hep}})(1 - E_{\mathrm{gut}})(1 - E_{\mathrm{feces}})$.

In many models, an absorption rate constant defined as $k_a = F_{\mathrm{bio}} \cdot k_{\mathrm{p.o.}}$ is used, resulting in $k_{\mathrm{p.o.}} = k_a/F_{\mathrm{bio}}$. It is important to realize that while k_a could in principle be very small, $k_{\mathrm{p.o.}}$ will normally not be, since it is limited by e.g., the natural GI transit time. It is, however, $k_{\mathrm{p.o.}}$ (and not k_a) that determines whether absorption is characterized by a flip-flop scenario.

5.3.4 2-compartment PK model with p.o. administration and beyond

The case of 2-compartment PK models with p.o. administration and other multi-compartment models can be treated analogously as in the 2-compartment i.v. bolus case. The common property of all these models is that their analytical solution is a sum of two or more exponentials with different rate constants (e.g., α and β; or λ and $k_{\mathrm{p.o.}}$ etc). Each exponential term can be formally associated with a 1-compartment model with i.v. bolus administration. Therefore, we may determine the half-life, accumulation factors, peak-to-trough ratio for each of those exponential terms. Then, the key characteristics of the multi-compartment PK model can again be written as weighted sums of the key characteristics of the associated 1-compartment models.

5.3.5 Half-lifes in the integrated framework

Effective (accumulation) half-life

For a 1-compartment model with i.v. bolus administration, it is clear that $k_{\mathrm{eff}} = \lambda$, and thus $t_{\mathrm{eff}} = t_{1/2}$. For a 2-compartment model with i.v. bolus administration, R_{AUC} depends on both accumulation factors $R_{\mathrm{AUC},\alpha} = R_\alpha$ and $R_{\mathrm{AUC},\beta} = R_\beta$ according to eq. (5.22). Rearranging terms yields

$$\begin{aligned} \exp(-k_{\mathrm{eff}}\tau) &= \frac{A/\alpha}{A/\alpha + B/\beta} \cdot \exp(-\alpha\tau) \\ &+ \frac{B/\beta}{A/\alpha + B/\beta} \cdot \exp(-\beta\tau). \end{aligned} \tag{5.37}$$

Consequently, $k_{\text{eff}} = k_{\text{eff}}(\tau)$ is a weighted sum of both rate constants, α and β.

Effective (NCA) half-life

For a 2-compartment model with i.v. bolus administration, $\text{AUMC} = A/\alpha^2 + B/\beta^2$, resulting in

$$t_{1/2,\text{NCA}} = \frac{A/\alpha}{A/\alpha + B/\beta} \cdot t_{1/2,\alpha} + \frac{B/\beta}{A/\alpha + B/\beta} \cdot t_{1/2,\beta}. \tag{5.38}$$

Although the similarity to eq. (5.22) is striking, in general, R_{AUC} is not linked to the half-life $t_{1/2,\text{NCA}}$. Furthermore, in general $t_{1/2,\text{NCA}} \neq \log(2)/k_{\text{eff}}$ with k_{eff} defined in eq. (5.11).

Operational half-life

Our framework enables us to precisely formulate the complex definition of operational half-life. We use a two-compartment model with i.v. bolus administration for illustration. When $R_{\text{peak}} = 2$, from eq. (5.23), we have

$$AR_\alpha + BR_\beta = 2. \tag{5.39}$$

On computing the peak-to-trough concentration ratio at steady-state from eq. (5.26), we see

$$\text{PT}_{\text{ss}}{}^{-1} = (AR_\alpha e^{-\alpha\tau} + BR_\beta e^{-\beta\tau})/2. \tag{5.40}$$

Using the definitions of the accumulation factors R_α and R_β of the associated one-compartment models, and exploiting the fact that A + B = 1, it is clear that $\text{PT}_{\text{ss}} = 2$. It can be shown that this relation holds for any multi-compartment model for i.v. bolus administration. Thus, we note that the operational half life is **completely** characterized by $R_{\text{peak}}(\tau = t_{1/2,\text{op}}) = 2$.

5.3.6 Approximation of the terminal volume of distribution

We also derive a new approximation to the terminal volume of distribution V_{z} for multi-compartment models, that allows for an understanding of the difference between the steady-state and terminal volume of distribution in terms of relevant PK processes and quantities.

Exploiting the definition of λ_z and $t_{1/2}$, we write the terminal half-life as

$$t_{1/2} = \log(2)\frac{V_{\text{z}}}{\text{CL}}, \tag{5.41}$$

where V_{z} denoted the volume of distribution at terminal phase. In the absence of knowledge of the inter-compartmental clearance Q, the terminal volume of distribution is sometimes approximated by the steady-state volume of distribution V_{ss}, resulting in the approximative half-life

$$t_{1/2,V_{\text{ss}}} = \log(2)\frac{V_{\text{ss}}}{\text{CL}}. \tag{5.42}$$

For 1-compartment PK models, we have $t_{1/2,V_{\text{ss}}} = t_{1/2}$ by definition. For multi-compartment PK models, the approximation quality, however, can be very different.

To present our approximation of the terminal volume of distribution, we first consider a 2-compartment PK model parameterized in terms of V_1, V_2, Q and CL (as in (5.2)). We

define the approximate terminal volume of distribution

$$\widehat{V}_z = (1 - E_z) \cdot V_1 + \frac{1}{1 - E_z} \cdot V_2, \tag{5.43}$$

where E_z denotes the terminal extraction ratio given by

$$E_z = \frac{\mathrm{CL}}{\mathrm{CL} + Q}. \tag{5.44}$$

In what follows, we derive an error bound on the approximation quality of $\widehat{V}_\mathrm{z}$ for the 2-compartment PK model and observe that when $V_1 < V_2$, the error in approximation is only about 5%. For our analysis, we introduce the dimensionless quantities $r = Q/CL$ and $s = V_1/V_2$. A rigorous mathematical justification of such non-dimensionalizing methods and their utility in the analysis of compartmental systems can be found in [277], where the authors discuss physiologically relevant bounds for the dimensionless quantities in a pharmacokinetic context and suggest that $s < 0.5$ for several known drugs.

We define the relative error of approximation as

$$\mathrm{err}_\mathrm{rel} = \frac{|\widehat{V}_\mathrm{z} - V_\mathrm{z}|}{V_\mathrm{z}} = 1 - \frac{\widehat{V}_\mathrm{z}}{V_\mathrm{z}}. \tag{5.45}$$

To derive explicit bounds on the relative error, it is advantageous to rewrite $\mathrm{err}_\mathrm{rel}$ as a function of r and s. To this end, we exploit the following relationships: $V_\mathrm{z} = \mathrm{CL}/\lambda_z$ with

$$\lambda_z = \frac{-1}{2} \cdot (\mathrm{Tr}(\mathcal{M}) + \sqrt{(\mathrm{Tr}(\mathcal{M}))^2 - 4 \cdot \det(\mathcal{M})}), \tag{5.46}$$

where $\mathcal{M} = \begin{pmatrix} -\frac{Q+CL}{V_1} & \frac{Q}{V_1} \\ \frac{Q}{V_2} & \frac{-Q}{V_2} \end{pmatrix}$, and $\mathrm{Tr}(\mathcal{M})$ and $\det(\mathcal{M})$ denote the trace and determinant of the matrix $\mathcal{M}$, respectively.

Using the non-dimensional parameters r and s, we then write

$$E_z = \frac{\mathrm{CL}}{\mathrm{CL} + Q} = \frac{1}{1 + r} \tag{5.47}$$

and

$$V_\mathrm{z} = \frac{1}{\frac{-1}{2}\left[\frac{-(r+1)}{sV_2} - \frac{r}{V_2} + \sqrt{\frac{r^2}{V_2^2} - \frac{2r^2}{V_2^2} - \frac{2r}{sV_2^2} + \frac{(r+1)^2}{s^2V_2^2}}\right]}. \tag{5.48}$$

Inserting these relationships into eq. (5.45), and exploiting the definition of V_z yields

$$\begin{aligned} \mathrm{err}_\mathrm{rel}(r, s) = 1 - \frac{1}{2s}\left(\frac{rs}{r+1} + \frac{r+1}{r}\right) \\ \left((rs + r + 1) - \sqrt{(rs + r + 1)^2 - 4rs}\right). \end{aligned} \tag{5.49}$$

In Fig. 5.4 (left), the function $g_s(r) = \mathrm{err}_\mathrm{rel}(r, s)$ is shown for different values of $s = 0.1, \ldots, 0.9$. We infer that the function $g_s(r)$ has a unique maximum at some point $r_\mathrm{max} =$

$r_{\max}(s)$, which is characterized by

$$\frac{\partial g_s}{\partial r}(r_{\max}) = 0 \quad \text{and} \quad \frac{\partial^2 g_s}{\partial r^2}(r_{\max}) < 0. \tag{5.50}$$

We solved eq. (5.50) using Mathematica$^{\text{TM}}$ 8. The maximal relative error $\text{maxerr}_{\text{rel}}(s) = g_s(r_{\max}(s))$ as a function of s is shown in Fig. 5.4 (right). From the function $\text{maxerr}_{\text{rel}}$ we determine:

$$\text{maxerr}_{\text{rel}} < 5.08\% \qquad \text{if} \quad s < 1 \tag{5.51}$$

and

$$\text{maxerr}_{\text{rel}} < 18.7\% \qquad \text{if} \quad s < 3 \tag{5.52}$$

This shows that for the most common situation of $V_1 < V_2$, the relative approximation error is less than about 5%. Further, weakening the condition to $V_1 < 3 \cdot V_2$ still results in a relative approximation error of less than 20%.

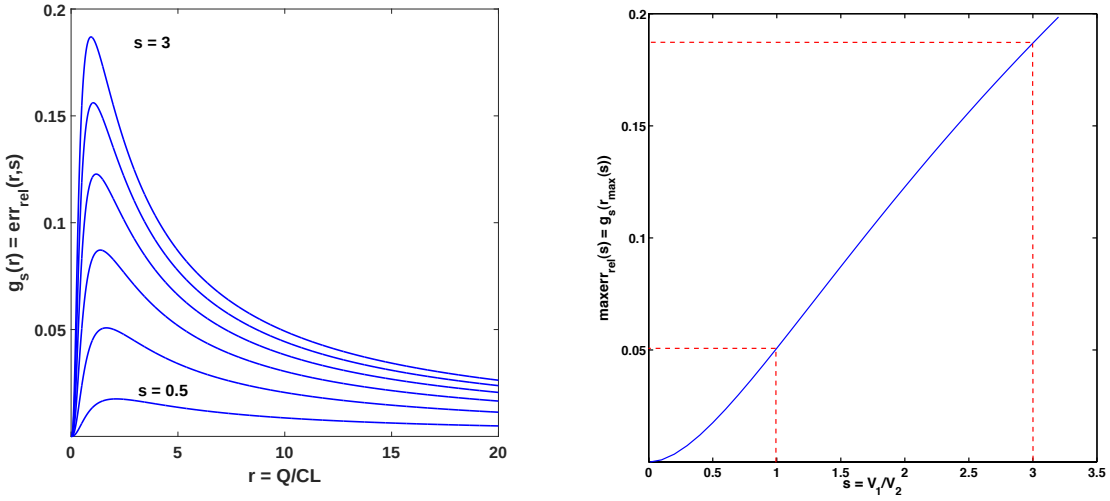

Figure 5.4. Left: Error function $g_s(r) = \text{err}_{\text{rel}}(r, s)$ for different values of $s = 0.5, \ldots, 3$. We observed that g_s always attained a unique maximum at some value $r_{\max} = r_{\max}(s)$. Right: Maxima $g_s(r_{\max}(s))$ as a function of s. We note that the maximal error incurred by the approximation is bounded by $\sim 5\%$ when $s < 1$ and by $\sim 18\%$ when $s < 3$.

Our approximation can be generalized to multi-compartment models with central volume V_1, plasma clearance CL and peripheral compartments with volumes and distribution clearances V_i and Q_i, respectively, for $i = 2, \ldots, k$, where $k \geq 2$ denotes the number of compartments. We define the slowest compartment 'slow' as the compartment with the smallest Q_i/V_i ratio, i.e.,

$$\frac{Q_{\text{slow}}}{V_{\text{slow}}} < \frac{Q_i}{V_i} \quad \text{for } i = 2, \ldots, k. \tag{5.53}$$

In this case, we define the approximate terminal volume of distribution

$$\widehat{V_{\mathrm{z}}} = (1 - E_{\mathrm{slow}}) \cdot (V_{\mathrm{ss}} - V_{\mathrm{slow}}) + \frac{1}{1 - E_{\mathrm{slow}}} \cdot V_{\mathrm{slow}}, \tag{5.54}$$

where the terminal extraction ratio E_z is defined as

$$E_z = \frac{\mathrm{CL}}{\mathrm{CL} + Q_{\mathrm{slow}}}. \tag{5.55}$$

We illustrate the performance of our approximation by comparing terminal volumes of distribution computed from pharmacokinetic parameters for five different drugs exhibiting a three-compartment PK behaviour to our approximate terminal volume of distribution (Table 5.1). In all instances, the error in approximation is limited to less than 20%.

The approximate terminal volume of distribution allows us to understand a potential difference between V_{ss} and V_{z} in terms of relevant PK processes. Under the condition of $V_1 < V_2$, it is

$$V_{\mathrm{z}}/V_{\mathrm{ss}} \approx (1 - E_z) \cdot (1 - V_2/V_{\mathrm{ss}}) + \frac{1}{1 - E_z} \cdot V_2/V_{\mathrm{ss}}. \tag{5.56}$$

Hence, for given volumes V_1 and V_2, the ratio growth is monotonous with E_z, i.e., with increasing ratio CL/Q. For given clearances CL and Q and fixed V_{ss}, the ratio growth is monotonous with V_2/V_1, i.e., when the peripheral constitutes a larger fraction of the steady-state volume of distribution.

Table 5.1. Comparison of exact and approximate terminal volumes of distribution for five different anaesthetic drugs exhibiting a three compartment PK behavior.

Drug	V_1	V_2	V_3	Q_2	Q_3	CL	E_z	s	V_{ss}	V_{z}	$\widehat{V_{\mathrm{z}}}$	$\mathrm{err}_{\mathrm{rel}}$
Propofol	16	35	250	1800	650	1900	0.75	0.2	301	994.7	993.8	0.1
Thiopental	6	34	150	2750	590	215	0.27	0.3	190	235.7	234	0.7
Remifentanil	5	10	6	2050	770	2600	0.77	2.5	21	35	29.7	15.1
Alfentanil	10	12.0	15	810	130	300	0.7	1.5	37	59.1	56.3	4.9
Fentanyl	15	35.0	250	3460	1650	1000	0.38	0.2	300	434.6	432.6	0.5

Volume in L, clearances in mL/min, $\mathrm{err}_{\mathrm{rel}}$ in %. The parameters of the three compartment are PK model are all taken from [278].

5.3.7 Understanding the accumulation and half-life of raltegravir

We now return to the raltegravir example. The authors in [15] assess the PK of 400 mg raltegravir administered twice a day and report AUC and peak accumulation factors of close to 1.0, while determining a long terminal half-life of 9-12 hours (depending on the dose-group studied) which is suggestive of accumulation. Benet et al [269] reconcile this apparent contradiction by computing an effective half-life, that unsurprisingly turns out to be lower (∼2 hours). On the other hand, Min et al [273] report comparable terminal half-lifes but moderate accumulation with a different integrase inhibitor. We now dissect the key characteristics using our framework to better understand such seeming discrepancies.

Iwamoto et al [15] use a bi-exponential of the form $C(t) = A{\cdot}\exp(-\alpha t)+B{\cdot}\exp(-\beta t)$ to fit multiple dose PK data. They report determining the parameter A by visual inspection and estimate parameters $t_{1/2,\alpha}$ and $t_{1/2,\beta}$, the half-lifes corresponding to a first and second phase of the decaying PK profile. They also report times to peak concentration after single dose and multiple doses to be 1 hour (although, theoretically, the latter is always lesser, see eqs. (5.31) and (5.32)). Since the drug is orally administered and shows a biphasic decline, we derive the AUC accumulation ratio (motivated by eqs. (5.22) and (5.33)) as

$$R_{\text{AUC}} = \frac{A/\alpha + B/\beta - (A+B)/k_{\text{p.o}}}{A/\alpha \cdot R_{\alpha}^{-1} + B/\beta \cdot R_{\beta}^{-1} - (A+B)/k_{\text{p.o}} \cdot R_{k_{\text{p.o}}}^{-1}}. \tag{5.57}$$

Now, setting $R_{\text{AUC}} = 1.05$ (as determined in [15]) and using an absoprtion rate constant of raltegravir of $k_{\text{p.o}} = 0.60$ (estimated in [279]), we obtain

$$A \approx -1230 \cdot B. \tag{5.58}$$

We next derive the peak accumulation ratio as

$$R_{\text{peak}} = \frac{A{\cdot}R_{\alpha}{\cdot}\exp(-\alpha{\cdot}t_{\text{ss,peak}})+B{\cdot}R_{\beta}{\cdot}\exp(-\beta{\cdot}t_{\text{ss,peak}})-(A+B){\cdot}R_{k_{\text{p.o}}}{\cdot}\exp(-k_{\text{p.o}}{\cdot}t_{\text{ss,peak}})}{A{\cdot}\exp(-\alpha{\cdot}t_{\text{sd,peak}})+B{\cdot}\exp(-\beta{\cdot}t_{\text{sd,peak}})-(A+B){\cdot}\exp(-k_{\text{p.o}}{\cdot}t_{\text{sd,peak}})} \tag{5.59}$$

Substituting eq. (5.58) above and using $t_{\text{ss,peak}} = t_{\text{sd,peak}} = 1$ hour, we obtain

$$R_{\text{peak}} \approx 1 \tag{5.60}$$

Having reproduced the observations in [15], we analyze why the accumulation factors are close to 1. As can be inferred from eq. (5.58), we have $|A| \gg |B|$. In this example, we have $R_{\alpha} \approx 1$. Additionally, when $k_{\text{p.o}} = 0.60$, we have $R_{k_{\text{p.o}}} = 1$. Under these conditions, we have R_{AUC} reducing to

$$R_{\text{AUC}} = \frac{A/\alpha + B/\beta - A/k_{\text{p.o}}}{A/\alpha + B/\beta \cdot R_{\beta}^{-1} - A/k_{\text{p.o}}}. \tag{5.61}$$

Since $\alpha \approx 10 \cdot \beta$, and $|A| \approx 1000 \cdot |B|$, we have $|A/\alpha| \gg |B/\beta|$, and it is clear that $R_{\text{AUC}} \approx 1$. A similar approximation analysis yields a jusifcation for $R_{\text{peak}} \approx 1$.

Hence, we note the ratios A/B and α/β determine the dominance of one or the other phase and terminal half-life (which is a measure of the rate of decline in the final phase) is independent of accumulation ratios (which are weighted composite measures of all phases of drug decline).

Thus, our framework enables us to isolate key characteristics of the system, analyze their dependence on the underlying pharmacokinetic parameters, and interpret them appropriately.

5.4 Impact of PK on viral dynamics

In this section, we examine the impact of PK fluctuations on viral dynamics. We first use a simple time-dependent concentration profile of an antiviral and study how this affects

the behaviour of a simplified viral dynamics model. After discussing such an incorporation of PK into a viral dynamics model, we show how fluctuations in drug concentrations could result in both qualitative and quantitative differences in virological outcomes, compared to a constant-drug effect scenario. We then assess the impact of PK on our viral dynamics model with drug-specific mutation schemes using ZDV as an example.

Monoexponential PK and simplified viral dynamics model

Consider a monoexponentially decaying drug concentration (or equivalently, a one-compartment PK model) described by

$$C_{\text{drug}}(t) = \frac{\text{Dose}}{V} \cdot \exp\left(-\frac{\text{CL}}{V} \cdot t\right), \tag{5.62}$$

where 'Dose' refers to the administered amount of drug, and CL and V are the clearance and volume of distribution of the drug, respectively. For simplicity of illustration of different parameter scenarios, we assume an i.v. bolus administration. Note that while the above equation describes the concentration-time profile after a single dose, a multiple dose generalization (as is required for our example) is straightforward to realize. For our example, we set CL = 1 L/hr and V = 50 L.

A two-stage viral dynamics model with three mutant genotypes —two single point mutants and one double point mutant (refer Figure 2.10 and Figure 2.11 of Chapter 2) is used. The fitness costs of the single mutants were assumed to be 0.05, while that of the double mutant is assumed to be 0.1, and the resistance factors are assumed to be 10 and 100, respectively. We note that these parameters were chosen only to illustrate the impact of fluctuating drug concentrations on viral dynamics, and are arbitrary, in that sense.

The drug concentration C_{drug} drives the efficacy, and hence the drug efficacy ϵ_{g} (eq. 2.4 of Chapter 2) becomes a function of time, $\epsilon_{\text{g}}(t)$.

$$\epsilon(t) = \epsilon_g(t) = \frac{C_{\text{drug}}(t)/\text{IC50}_g}{1 + C_{\text{drug}}(t)/\text{IC50}_g}. \tag{5.63}$$

For our illustration here, we chose an integrase inhibitor administered at a dose of 100 mg with a dosing interval τ of 1 day. Again, this choice of parameters does not impact our foregoing discussions. We chose an average (over time) drug efficacy of 90% for the wild type, i.e., $\epsilon_{\text{avg,WT}}(t) = 0.90$, which is realized through a time-averaged drug concentration (over a dosing interval). Over a certain dosing interval τ, we defined the average drug concentration $C_{\text{avg}}(t)$ as

$$C_{\text{avg}}(t) = \frac{1}{\tau}\int_0^{\tau} C_{\text{drug}}(t)\,\mathrm{d}t, \tag{5.64}$$

where the integration is over one dosing interval. The drug efficacies for the different mutant genotypes are obtained as earlier (Chapter 3) using their corresponding fitness costs and resistance factors.

We observed both qualitative and quantitative differences in viral dynamics depending on the underlying PK fluctuations. A key parameter that influences the dynamics of mutant genotypes is the stead-state peak-to-trough ratio PT_{ss} of the drug. In our simplified

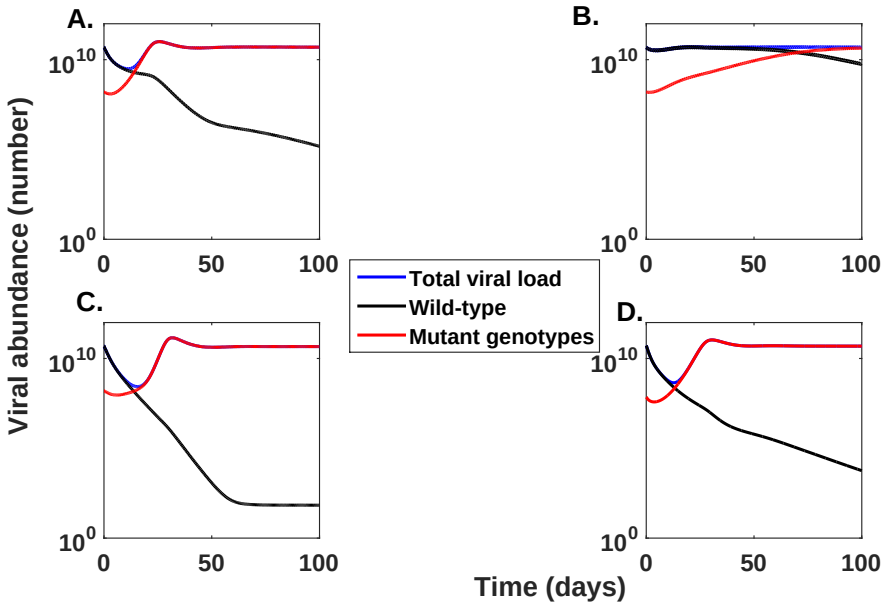

Figure 5.5. Impact of PK fluctuations on viral dynamics. Steady-state peak-to-trough ratios are varied as **(A)** $\mathrm{PT_{ss}} = 1.6$, **(B)** $\mathrm{PT_{ss}} = 121$, and **(C)** $\mathrm{PT_{ss}} \sim 1$. In **(D)**, we show the dynamics with no PK fluctuations, for comparison.

PK model, this is easily calculated (eq. 5.18). For example, when CL = 1 L/hr and $V = 50$ L, therapy failure was due to mutations, as was the case when there are no PK fluctuations incorporated (panels A and D, respectively, in Figure 4). Interestingly, between these two situations, we noticed minor differences in the time to mutations, with the mutations taking up to 5 days longer to appear at detectable levels, when PK is incorporated. The peak-to-trough ratio $\mathrm{PT_{ss}}$ for Panel A is about 1.6. When the fluctuations were decreased to $\mathrm{PT_{ss}} \sim 1$ (Panel C), by decreasing the clearance 10 times, the failure was again due to mutations with mutant genotypes appearing later ($\sim$35 days). This difference in the time to appearance of different mutations can be attributed to the finite non-zero time for the drug concentration (and thereby the drug efficacy ϵ_{g}) to attain steady-state (as opposed to the constant drug-effect situation). With an increase in fluctuations realized by setting CL = 10L/hr and $V = 50$ L (resulting in $\mathrm{PT_{ss}} = 121$), we noted failure due to wild type (Panel B). Here, viral load rebounds within 10 days, while mutant genotypes take up to 60 days or longer to be detected. With such large fluctuations in drug concentrations and increased time spent at low concentrations, the selection pressure on mutant genotypes is not very high, leading to their delayed appearance.

Impact of ZDV PK on emergence of mutant genotypes

In Chapters 3 and 4, we assumed a constant drug effect (ϵ_{wt})—as is commonly done in viral dynamics models [6, 7, 115]. As discussed in the previous section, the integration of pharmacokinetic drug profiles can also be realized in our viral dynamics model with drug-specific *in vivo* mutation schemes. For illustration, we consider a two-compartment PK model of ZDV with parameters from literature [280, 281]) (a clearance $CL = 1.6$ L/h/kg, central and peripheral volumes $V_1 = 1.6$ L/kg and $V_2 = 3.2$ L/kg respectively, and an

inter-compartmental clearance $Q = 3.2$ L/h/kg). Here, Q and V_2 are chosen to obtain a steady-state peak-to-trough ratio in the peripheral (effect) compartment of about 2-3, in line with previous observations for NRTIs [280, 282]. More detailed physiologically-based PK models have been proposed [280], but this is beyond our current scope.

Table 5.2. Statistical and mechanistic waiting times to observe mutations under ZDV therapy with ZDV concentration described by a two-compartment pharmacokinetic model.

Mutation	Statistical average waiting times	Mechanistic waiting times
41L	1.00	1.00
67N	1.10	1.06
70R	2.18	1.81
210W	1.28	1.10
215Y	1.08	1.02
219Q	2.34	1.81

The average statistical waiting times and the corresponding mechanistic waiting times to observe mutations at the different positions under ZDV therapy. ZDV concentration is assumed to be described by a two-compartment PK model. The average statistical and mechanistic waiting times are calculated as described in Chapter 3. Both waiting times are expressed relative to the time to the fastest occurring mutation. The predicted mechanistic waiting times has a high and significant correlation (r = 0.99, p-value = 0.0001) with the statistical waiting times.

Our simulations are scaled for an individual with body weight of 70 kg, administered a dose of 300 mg twice daily, in accordance with clinical recommendations The concentration in the peripheral (effect) compartment is coupled to the virus dynamics model similar to the example in the previous section. ZDV is an NRTI, and as a consequence, the parameters β_{T}, CL_{T}, β_{M} and CL_{M}, influenced by ZDV, are now functions of the drug concentration and therefore, of time. We observed that the predicted mechanistic waiting times did not vary significantly (Table 5.2) from the constant drug-concentration case. The mechanistic waiting times retained a high correlation with the average statistical waiting times (r = 0.99, p-value = 0.0001). The order of appearance of mutations was also preserved.

5.5 Summary

Viral suppression by an anti-HIV drug depends on time-dependent pharmacokinetic fluctuations in drug concentrations. Drug accumulation ratios and half-lifes play an important role in drug development and therapeutics. In this chapter, we reviewed various measures of accumulation and half-lifes. We then presented an integrated framework to derive and interpret key PK characteristics and illustrated the utility of such an approach using raltegravir as an example. Our framework afforded a consistent understanding of multiple dosing phenomena, and can be readily generalized to multi-compartment models. Importantly, it also lends itself to an intuitive understanding and interpretation of different

measures of drug accumulation. We also study the impact of PK on antiviral effect and noted the possibility of qualitative and quantitiave differences in virological outcome, compared to constant drug-effect models. Finally, we assessed the impact of incorporating PK on the dynamics of mutant genotypes under ZDV therapy using our viral dynamics model with detailed mutation schemes. With combination therapy and drug-drug interactions, the behaviour is expected to be more complex. Different models for the coupling of concentration to effect can also be explored. Recent work by Rosenbloom et al [160] proposes the existence of mutant selection windows and studies the impact of drug concentrations on mutant selection. However, this work relies on mono-exponential PK profiles combined with *in vitro* IC50 measurements. More detailed investigations into the influence of PK on mutant selection are certainly warranted.

Chapter 6

Parameter estimation and identifiability in viral dynamics models

6.1 Introduction

Parameter estimation is an ubiquitous task in systems biology where detailed models with several parameters are used to adequately reflect the biological system of interest [283,284]. The uncertainties in the estimated parameters is a crucial feature when the model is subsequently used to simulate biological behaviour, in particular when experimental data is either unavailable or scanty. Owing to both the unavoidable complexities (such as nonlinearities) in the model and the paucity of experimental data, parameter identifiability and sloppiness (sloppiness refers to high sensitivity of models to certain parameter combinations, and not others) [285] are frequent concerns in such settings.

There are several techniques based on diverse approaches that have been devised to assess parameter identifiability, to address sloppiness, and to infer meaningful estimates of parameters [286–289]. Occasionally, statistical regularization techniques have also been used—see [290] for an excellent review of how formal statistical methods designed for ill-posed inverse problems find applications in systems biology.

In this chapter, we focus on parameter identifiability problems encountered in our settings of viral dynamics models. We begin by presenting a technique that we adapt from literature to alleviate issues of parameter identifiability in the estimation of fitness characteristics of HIV mutant genotypes. Next, we briefly review a few theoretical aspects of regularization as applied to linear models and examine the utilitzation of such regularization methods in nonlinear models. In general, regularization methods in parameter estimation with nonlinear models are far less studied in comparison to linear models, and some of our numerical results represent a promising step towards utilizing such methods for parameter estimation in virus dynamics models.

6.2 Family of model fits

In general, the procedure of parameter estimation for a given model can have different outcomes (see [291] for a review) —A) a single, unique solution set of parameter estimates (the solution set of parameter estimates refers to the set of estimates obtained for each of the model parameters by an optimization procedure) rendering the model globally identifiable, B) a countable number of solution sets of parameter estimates rendering the model locally identifiable, C) an uncountably infinite number of solution sets of parameters rendering the model unidentifiable, D) no parameter solution set. Of these, many estimation

problems in systems biology fall under Scenarios B and C, mainly due to model nonlinearities necessary to effectively reflect biological phenomena. Chen et al [288] rightly observe that while parameter identifiability has received extensive attention in fields as diverse as climate change and nuclear reaction modelling, it has largely been ignored in biology.

In complex models riddled with nonlinearities, the authors in [288] suggest estimating not one parameter solution set, but a family of solutions (due to the underlying non-identifiability common in such models, the parameter solutions comprising the family would not be expected to be all identical) using Monte Carlo based approaches like simulated annealing [292]. A selected subset of such solutions (for example, based on a root-mean-squared deviation (RMSD)) can then be examined and useful features relevant to the biological situation at hand, can be extracted.

We investigated the validity of this approach in alleviating parameter identifiability issues while estimating fitness costs of HIV mutant genotypes. To understand this approach and demonstrate its utility, we first illustrate its performance using a viral dynamics model with a simple mutation scheme.

6.2.1 A simple example

We consider the two-stage virus dynamics model (Figure 2.10, Chapter 2). In the following, the uninfected target cells comprise of only T-cells; we drop macrophages and latently infected cells from the model for purposes of simplicity. Apart from altering the dynamics in a limited manner, incorporating these features would not alter our conclusions, especially regarding features of parameter estimation. We modelled the action of an integrase inhibitor and assumed a simple mutation scheme (Figure 6.1), wherein the wild type virus firstly acquires one mutation and subsquently accumulates another mutation. This results in two possible mutant genotypes: a single mutant and a double mutant. Note that this corresponds to a CBN model of mutations with a poset such that mutation at position 1 occurs from the wild type, followed by a further accumulation of mutation at position 2. The mutation rate μ was fixed to be $3.4 \cdot 10^{-5}$, as before. We first simulated this model using certain fixed fitness costs ($s(\{1,0\}) = 0.2$, $s(\{1,1\}) = 0.1$) and resistance factors for the two mutant genotypes and compute (mechanistic) waiting times for the two mutations. We then examined if these 'true' fitness costs and/or key features of the model can be recovered via parameter estimation using the waiting times 'data'. The drug-effect and other parameters used in this study are summarized in Table 6.1.

Table 6.1. Drug effect and resistance parameters used in the simulation-estimation procedure.

Parameter	Value
Resistance factor of single mutant {1,0}	10
Resistance factor of double mutant {1,1}	100
Drug-effect (ϵ_{wt}) on wild type	0.90

We perfomed 50 rounds of estimation starting from different initial estimates using the simplex-search based algorithm *fminsearchbnd* in MATLAB^{TM}. Here, the waiting times

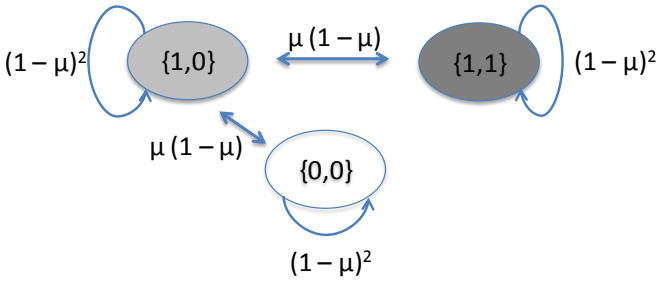

Figure 6.1. A simple mutation scheme wherein the wild type virus accumulates two mutations in sequence.

used to estimate the fitness costs come from simulations (as opposed to being learned statistically from experimental data) and so are known to arbitrary precision. Hence, we used all 50 estimated sets of fitness costs for analysis. As would be expected, the estimated fitness costs were not all identical and depended on the initial estimates. Statistical measures of dispersion of the distributions of estimates such as the standard deviations also revealed unidentifiability (Table 6.2). However, we noted several features of utility in the obtained family of fits. Firstly, the 'true' fitness costs (and selective advantages) were recovered and corresponded to the best fit in the family (the fit with the lowest objective function value in the estimation). Secondly, each round of estimation yielded a set of fitness costs (and selective advantages) that was highly rank correlated (Spearman rank correlation $\rho = 1$) to the set of the true fitness costs (and selective advantages). This suggests that despite the lack of global identifiability in the estimation, the family of fitness estimates possess a certain robustness as regards their order (we give a plausible qualitative reasoning later).

Table 6.2. Original (simulated) and estimated fitness characteristics

Fitness characteristic	Original (simulated)	Estimated best fit	Mean (SD) from family of fits
Fitness cost of single mutant {1,0}	0.2	0.2	0.29 (0.1)
Fitness cost of double mutant {1,1}	0.1	0.1	0.22 (0.13)
Selective advantage of single mutant {1,0}	7.3	7.3	6.4 (0.96)
Selective advantage of double mutant {1,1}	8.9	8.9	7.1 (1.2)

When the 'true' fitness costs were fixed to be sufficiently close (within 0.02) to each other, their recovery with parameter estimation was not robust. However, we observed that in these situations, the estimated fitness costs were also very close to each other. Alternate optimization procedures may be investigated. In general, we caution against making conclusions on the order of fitness costs in such instances.

To further systematically assess the utility of this approach, we repeated the above

simulation-estimation procedure with 50 different samples of randomly generated 'true' fitness costs (instead of one, as above) ensuring that the single and double mutant genotypes had sufficiently different (apart by greater than 0.02) fitness costs. For each sample of these 'true' fitness costs, we computed associated mechanistic waiting times and used these to perform parameter estimation. 50 rounds of estimation were performed for each sample. We observed that in 28 out of the 50 samples (56%), the 'true' fitness costs were recovered. However, more remarkably, for each of the 50 samples, the true fitness costs and all sets of estimated fitness costs were rank correlated (Spearman rank correlation $\rho = 1$). This indicates that parameter estimation of fitness costs, in this example, yields solutions that are rank correlated with the underlying 'true' fitness costs. A semi-quantitative reasoning for such a correlation would involve the structure of the poset and goes as follows. The poset, by itself, imposes a certain regularization on the estimation problem. In our current simple example, the only way to detect the second mutation at position 2 would be via the the double mutant genotype. This genotype can reach detectable levels and fixate in the viral population only if its selective advantage exceeds that of the single mutant genotype. Using the definition of selective advantage (eq. (3.6) in Chapter 3), and substituting for resistance factors and ϵ_{wt} with values used above, we obtained

$$s(\{1,1\}) < 0.082 + 0.918 \cdot s(\{1,0\}). \tag{6.1}$$

Such regularizations are imposed even in more complex posets as those for ZDV or IDV therapy. Analytical calculations of these regularizing conditions and the degree of redundancy therein, may be dissuadingly involved mainly due to multiple escape pathways available to the virus from any given genotype. Nevertheless, such constraints that are automatically imposed by the poset assist in enhancing correlations between the estimated sets of fitness characteristics.

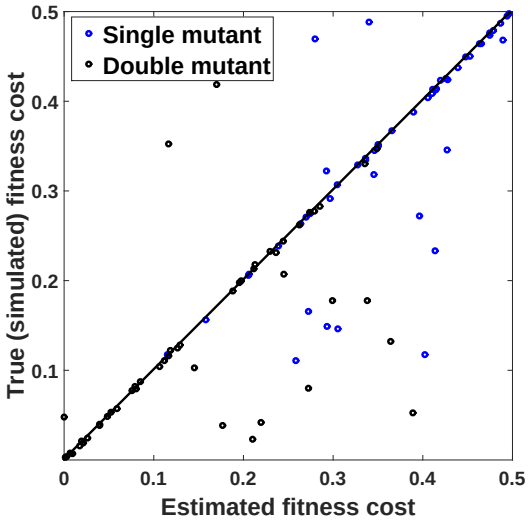

Figure 6.2. True and estimated fitness costs. A plot of 'true' and estimated fitness costs for single and double mutant genotypes induced by the poset shown in Figure 6.1

Additionally, many of the estimated fitness costs are over-predicted (rather than un-

derpredicted) as seen in Figure 6.2. This suggests that further regularization on the magnitude of fitness costs by statistical techniques such as ridge regression may be useful and this serves as a motivation for Section 6.3.

6.2.2 Estimation of fitness costs of ZDV and IDV mutant genotypes

To study the robustness of our estimated fitness characteristics of HIV mutant genotypes arising during ZDV and IDV monotherapies (Sections 3.4 and 3.5, Chapter 3), we performed 500 rounds of repeated estimation by randomly choosing different initial estimates. We also subsequently performed simulated annealing with the function *simulannealbnd* in MATLAB$^{\text{TM}}$ to test for convergence of our estimates. We did not explicitly observe non-identifiability (indicated by a flat cost function surface in multiple dimensions near the best estimate). However, as in [288], we noted that several rounds of simulated annealing converge to different estimates indicating a rugged search landscape and a possible lack of a well-defined minimum. Following the approach in [288], we considered all fits with an RMSD of less than 0.1 between the mechanistic and statistical waiting times as equally valid (since we estimated the average error in the normalized statistical waiting times data to be $\pm 10\%$). All fits with an RMSD less than the error incurred in the data used for estimating fitness costs cannot essentially be distinguished. The RMSD for a fit f was defined as follows:

$$\text{RMSD}_f = \sqrt{\frac{1}{n} \cdot \sum_{e \in \mathcal{E}} (\mathbb{E}[T_{e,\text{stat}}] - T_{e,\text{mech}})^2}, \tag{6.2}$$

where e denotes a mutation occurring in the corresponding poset $\mathcal{E}$ and n denotes the total number of mutations considered. We investigated all our results on fitness characteristics based on this ensemble of fits.

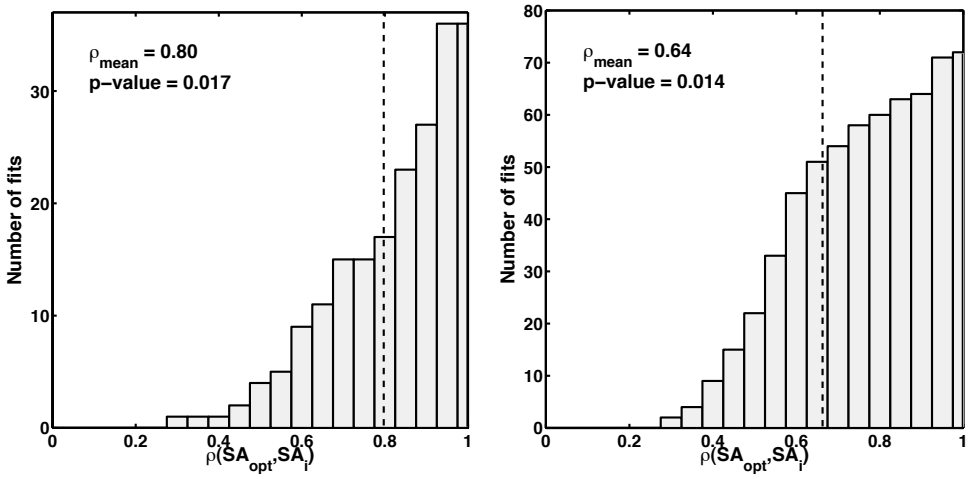

Figure 6.3. Cumulative histograms of correlations of fitnesses between valid fits and best fit. Cumulative histograms of Spearman rank correlation of estimated fitnesses of mutants (quantified by selective advantages) between the best fit and every other valid fit for ZDV mutants (left) and IDV mutants (right). The vertical dashed line shows the mean correlation.

Of the $N = 500$ fits, we recovered 35 valid fits for ZDV and 72 valid fits for IDV. For

ZDV mutants, we noted a strong and significant Spearman rank correlation ($\rho_{\text{mean}} = 0.80$, p-value = 0.01) of selective advantages between the best fit and all other valid fits (Figure 6.3A). Similarly for IDV mutants (Figure 6.3B), the correlation was 0.64 (p-value = 0.01). This indicated that the order of fitness characteristics that we estimated is strongly preserved across all the considered fits and enabled us to make valid inferences from our fitness estimates. We also examined specific observations on fitness characteristics for their behavior across valid fits and observed that they are strongly conserved.

Table 6.3. Conservation of estimated fitness characteristics of ZDV and IDV mutants amongst valid fits.

Drug	Observation	% of valid fits where conserved
ZDV	Average fitness cost of TAM-1 mutants < Average fitness cost of TAM-2 mutants	90
	Average SA of TAM-1 mutants > Average SA of TAM-2 mutants	100
	s({41L, 210W, 215Y}) > s({41L, 215Y})	92
	s({67N,70R}) > s({67N})	80
	s({41L, 210W, 215Y}) < s({67N, 70R, 219Q})	81
	SA({41L, 210W, 215Y}) > SA({41L, 215Y})	64
IDV	s({90M}) < s({71V})	65
	71V compensates fitness	77
	SA({71V, 82A}) ≈ SA({54V, 71V, 82A})	71

For ZDV mutant genotypes, in about 90% of the valid fits, we found that the average fitness cost of TAM-1 mutants is less than that of TAM-2 mutants, while in approximately 92% of valid fits, the deleterious effect of 210W inserted in a {41L, 215Y} backbone in the absence of ZDV was preserved. Similarly, we examined the validity of each of our conclusions (in Sections 3.4 and 3.5 of Chapter 3) and found that they are all well-conserved across the valid fits (Table 6.2). For IDV mutant genotypes, we again found the average fitness estimates (Figure 3.7C, Chapter 3) to be very strongly conserved ($\rho_{\text{mean}} = 0.90$, $p = 0.02$).

6.3 Regularization

Regularized methods of parameter estimation are standard techniques employed routinely in statistics, at least since the seminal paper by Tibshirani in 1996 [293]. A strong motivation behind the use of regularized estimators is that they result in a marked reduction in prediction error, in spite of introducing a bias. We refer to [294] for a concise review of regularization approaches and do not delve into all underlying details in this thesis. Informally, a bias of an estimator is the difference between its expected value and the 'true' value, thereby a biased estimator of a parameter suffers from an inability to yield a 'correct' value of the parameter, on average, even with precise and unlimited data. The most commonly used least squares estimator is an unbiased estimator. While a bias in an estimator appears to be an undesirable property, in most practical problems we are

concerned about consistency in parameter estimation, rather than an asymptotic convergence to the true underlying parameter value (in fact, given the uncertainty and paucity in data, the recovery of 'true' parameters cannot be guaranteed in practice, even with an unbiased estimator). As the authors in [294] argue, consistency or predictive behaviour of the model is of more direct relevance. Thus, sacrificing unbiasedness in favour of enhanced precision (in what is commonly referred to as the bias-variance trade-off) would be valuable in many practical problems, including in biology.

Two of the most common methods of regularization employed are the lasso (short for Least Absolute Shrinkage and Selection Operator) [293] and ridge regression [295]. In this section, we first formally define the regularization methods and illustrate them with a linear model. We then explore the utility of implementing regularization in nonlinear models using a viral dynamics model.

6.3.1 Linear models

We first state the problem of least squares based parameter estimation in a linear model and then introduce the additional regularization terms. Consider a linear regression model for a response variable $\mathbf{Y}= (y_1, ..., y_n)$ in terms of $\mathbf{X} = (x_{ij})$, with p parameters $\boldsymbol{\beta} = (\beta_1, ..., \beta_p)$, where $i = 1, ..., n$ and $j = 1, ..., p$. We write

$$\mathbf{Y} = \mathbf{X} \cdot \boldsymbol{\beta} + \epsilon. \tag{6.3}$$

Here, $\boldsymbol{\beta} = (\beta_1, ..., \beta_p)$ is a vector of p regression parameters and $\mathbf{X}$ is the design matrix. The regression problem is then to estimate $\boldsymbol{\beta}$ from n observations of the response variable $\mathbf{Y}$ and n observations of each of the p regressors in $\mathbf{X}$. One common estimation procedure is to minimize the squared errors of model predictions compared to the data i.e.,

$$\hat{\boldsymbol{\beta}} = \arg\min_{\boldsymbol{\beta}} \left\{ \sum_{i=1}^{n} \left(y_i - \sum_{j=1}^{p} x_{ij}\beta_j \right)^2 \right\}. \tag{6.4}$$

This is the ordinary least squares (OLS) estimation and is known to be the best linear unbiased estimator (BLUE) under the assumptions of the Gauss-Markov theorem. However, owing to its particular susceptibility for over-fitting in ill-conditioned problems and to enhance predictability, regularization terms may be introduced in the above estimator. Regularization terms can be viewed as penalty terms on the magnitude of parameters and popular choices include the L_1 or L_2 norm of the parameters. Accordingly, we have the lasso and ridge regression approaches. We do not go into the details, merits, drawbacks and extensions of each of those, and merely illustrate their application with a simple example. With ridge regression, the minimization problem can be written as

$$\hat{\boldsymbol{\beta}} = \arg\min_{\boldsymbol{\beta}} \left\{ \sum_{i=1}^{n} \left(y_i - \sum_{j=1}^{p} x_{ij}\beta_j \right)^2 + \lambda \cdot \sum_{k=1}^{p} \beta_k^2 \right\}. \tag{6.5}$$

Here, λ is the ridge parameter that dictates the extent of penalty (when $\lambda = 0$, the estimation reduces to ordinary least squares, while for large values of λ, all parameters

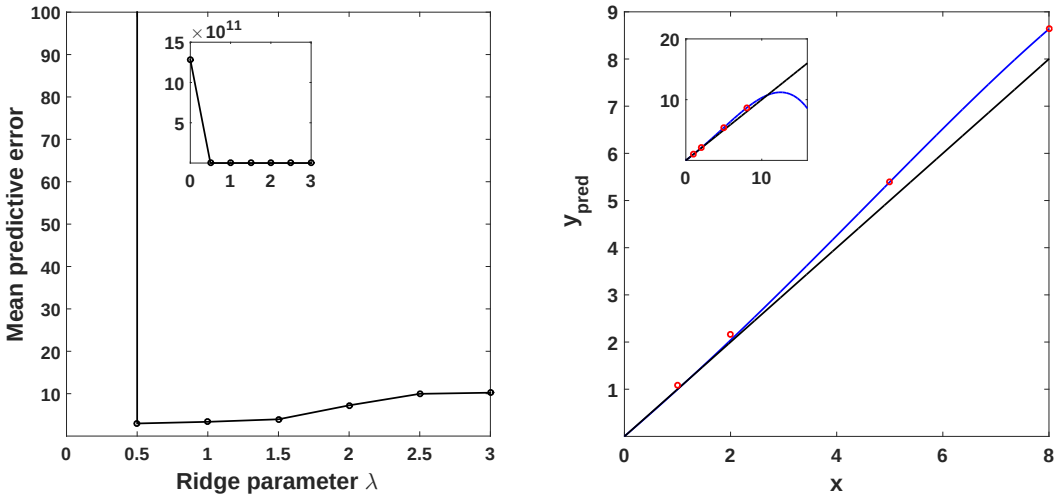

Figure 6.4. Performance of OLS fitting versus ridge regression. A bi-quadratic polynomial is fitted to (approximately) linear data by OLS and ridge regression based fitting. For a certain $\lambda > 0$, the mean predictive error drops lower than that from an OLS fit (panel A). The inset in (A) is a magnified view, that illustrates a minimum predictive error at $\lambda = 0.5$. While OLS fits the observed data better (panel B), ridge regression clearly benefits from a higher predictive power. The inset in (B) illustrates the poor behaviour of OLS (blue) when used for predictive purposes, compared to more robust performance of ridge regression (black). Here, x is the predictor in the regression model, while y_{pred} is the predicted response variable. The observed data are indicated by red circles.

shrink close to zero). The ridge parameter is generally calculated by computing the mean predictive error (typically by cross validation) for a range of values of λ and choosing that value which minimizes the error (for detailed discussions, see [294]).

Table 6.4. (Approximately) linear data fitted to a bi-quadratic polynomial model by OLS and ridge regression.

Parameter	True value	OLS	Ridge regression
A_0	0	$1.01 \cdot 10^6$	0.01
A_1	1	$-1.84 \cdot 10^6$	0.94
A_2	0	$1.02 \cdot 10^6$	0.03
A_3	0	$2.02 \cdot 10^5$	0
A_4	0	$1.26 \cdot 10^4$	0
MSE of estimates	-	$5.5 \cdot 10^{12}$	0.005
OFV	-	$3 \cdot 10^{-6}$	0.07

For an illustration of the utility of ridge regression, we study the following 'toy' problem. Consider a response variable Y and a dependent variable X with a 'true' underlying linear model $Y = X$. Note that one does not have any knowledge of this true model during the model building and parameter estimation process. We have data consisting of measurements X_{obs} of X and Y_{obs} of Y. Since Y_{obs} is typically measured by experiments,

we may expect it to be different from its 'true' value of $Y_{\text{true}} = X_{\text{obs}}$. In fact, Y_{obs} would almost never exactly be Y_{true} in practice. Hence, we randomly perturb Y_{true} by up to 10% and consider this to be Y_{obs} used for estimation. To illustrate the benefit of ridge regression in an illconditioned/over-fitting scenario, we fit the data to the bi-quadratic polynomial model $\mathcal{M}$ given by

$$\mathcal{M}: \quad \sum_{i=0}^{4} A_i \cdot x^i. \tag{6.6}$$

We would now certainly desire a solution closest to our 'true' values of parameters, but would also like the model to have good predictive power. Predictability is assessed via cross-validation by the leave-one-out approach, where one observation is left-out in turn from the data, the model is fit and the prediction compared to the observed value at the left-out point. Cross validation error can then be computed as the mean of such predictive errors. We observe that while OLS fitting suffers from poor predictive abilities, ridge regression overcomes this to a large extent (Table 6.4). Moreover, the mean squared errors of the parameter estimates is also smaller. As seen in Figure 6.4A, we note the existence of a certain λ, for which the mean predictive error is less than that of OLS. The existence of such a ridge parameter that lowers the prediction error can infact be theoretically proved for linear models in general (see [294] for example). Further, while OLS performs better in explaining the observed data, the ridge regression is far less susceptible to overfitting (Figure 6.4B).

6.3.2 Regularized estimation of fitness costs of HIV mutant genotypes

We now examined if such regularizing approaches are useful in the context of estimation of fitness costs of HIV mutant genotypes. There are several challenges involved, the main one being the nonlinearity of the model. Very few investigations have been performed on the application of methods like ridge regression in nonlinear problems. While the theoretical foundations are much harder, there are some examples in literature of employing ridge regression in nonlinear parameter estimation [296]. However, there is still a marked need to further explore the benefits of such approaches. We first used a virus dynamics model with a simplified mutation scheme (Figure 6.5) and estimated fitness costs of mutant genotypes from (simulated) waiting times of mutations. We compared the performance of ordinary least squares approach with the ridge regression based estimation. We then explored the utility of ridge regression in estimating fitness costs using our integrated model for ZDV monotherapy with the full mutation scheme

With the simplified mutation scheme, we modelled three mutations (and the five genotypes induced by them, in accordance with the poset in Figure 6.5). OLS estimation was carried out, as usual and its predictive performance was assessed via cross validation, as before. Ridge regression was performed with different values of the ridge parameter. The true fitness costs and other estimation characteristics are presented in Table 6.5. Firstly, we observed that for a certain $\lambda > 0$, ridge regression resulted in a lower mean predictive error compared to the OLS estimation (Figure 6.6). Note that unlike in linear models,

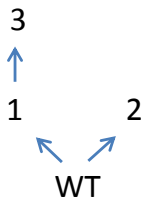

Figure 6.5. A mutation poset with three mutations modelled. Mutations are modelled at three positions with mutation at the third position requiring a parent mutation at position 1 to occur. The poset will induce a genotype lattice comprising of two single mutant genotypes, two double mutant genotypes and one triple mutant.

this is not guaranteed, and in fact, a formal proof of the existence of such a λ cannot be found in literature. Moreover, estimation via ridge regression also resulted in a lower mean squared error for the fitness costs.

Using such approaches in virus dynamics models enforces a further degree of regularization apart from the natural constraints imposed by the structure of the poset. The resultant estimates, thus represent some kind of a 'minimal' set of fitness costs explaining the observed waiting times and make predictions in line with the poset constraints.

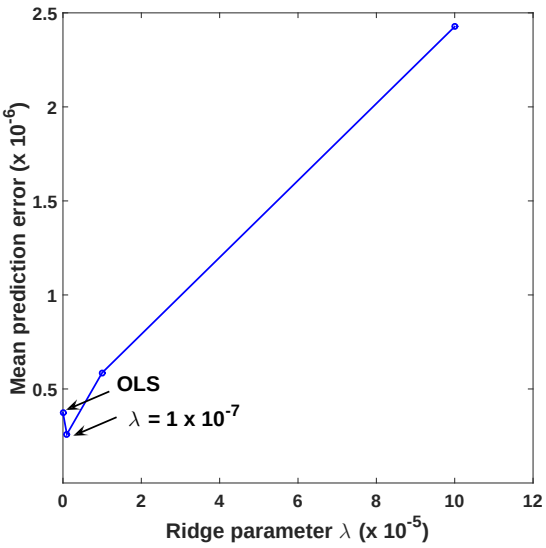

Figure 6.6. Mean prediction error of ridge regression in the estimation of fitness costs. The mean prediction errors in waiting times is computed for different values of the ridge parameter λ. For $\lambda = 10^{-5}$, ridge regression out-performs OLS by displaying a lower mean prediction error.

We also explored the possibility of application of ridge regression to our integrated model with the complete genotype lattice for ZDV monotherapy (Figure 3.1 , Chapter 3). At this stage, we point out a complication of using this approach in our setting. An important step in using ridge regression is the determination of a suitable ridge parameter λ. As discussed, this is usually accomplished by calculating mean prediction errors for a range of λ values via the leave-one out approach. However, cross validation in our model

Table 6.5. (Simulated) waiting times fitted to a virus dynamics model with three mutations (and five mutant genotypes) by ordinary least squares (OLS) and ridge regression.

Parameter	True value	OLS	Ridge regression
$s(1)$	0.1	0.06	0.006
$s(2)$	0.2	0.14	0.14
$s(1,2)$	0.3	0.36	0.34
$s(1,3)$	0.3	0.29	0.29
$s(1,2,3)$	0.1	0.05	0.06
MSE of estimates	-	$3.7 \cdot 10^{-7}$	$2.6 \cdot 10^{-7}$

has limited meaning, if any. This is because, if one drops an observation of waiting time, this implies that the associated mutation in the poset also needs to be dropped. In turn, this would warrant re-learning of the poset, leading to some kind of cross-validation at the poset level. In our preceding example with the simplified mutation scheme, we ignored this complication by assuming that dropping an observed waiting time for purposes of cross validation does not require dropping the associated mutation, i.e., we know that a mutation has occurred and retain it in the poset, but for some reason, we do not have a waiting time.

An alternative approach to determining the ridge parameter involves a graphical aid, the ridge trace [297]. This is based on the premise that parameter estimates stabilize around the region when $\lambda = \lambda_{\text{crit}}$ (λ_{crit} is the critical value of the ridge parameter where the prediction error drops below that of the OLS fit). A ridge plot implemented for our ZDV example suggested such a behaviour (Figure 6.7). However, we caution that a rigorous mathematical justification is sketchy, at best for linear models.

Another remark on the ridge parameter is not out of place here. In the current work, we concerned ourselves only with exploring the effects of regularization on the robustness of estimated fitness costs. To this end, we are satisfied when we locate a certain value of the ridge parameter that results in a better predictive performance compared to the OLS approach. A finer discretization of the ridge parameter space would be required if we desire to find an optimum value resulting in a truly minimal prediction error.

6.4 Summary

Parameter estimation and identifiability is an ever-present challenge in complex models used in systems biology. In the context of virus dynamics models, we explored two techniques to alleviate this issue. Firstly, estimating a family of fitness parameters instead of one optimal set enabled us to analyze fitness characteristics that are better conserved and more robust to the vagaries of fitting. We also demonstrated how posets of mutations impose natural constraints and aided in the estimation process. Secondly, regularization approaches such as ridge regression are extremely common in linear models, while the theoretical complexity inherent in nonlinear problems has limited investigations on their

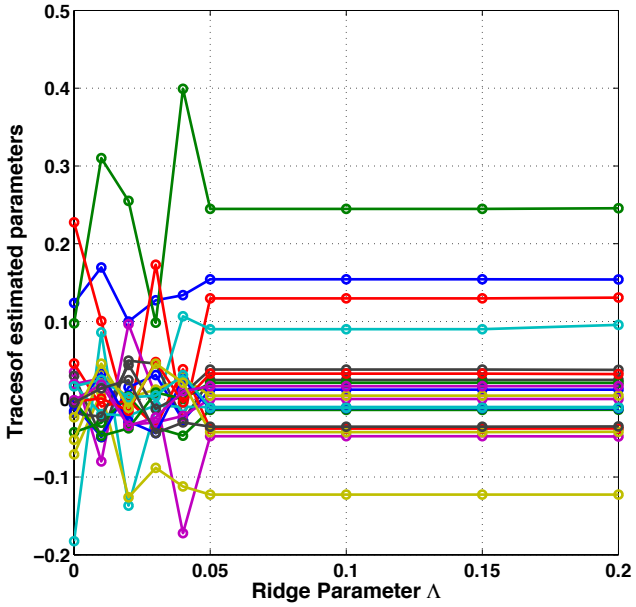

Figure 6.7. Ridge trace for the ZDV example The mean prediction error in waiting times is assessed for a range of the ridge parameter λ values for the virus dynamics model under ZDV therapy with the full genotype lattice (Figure 3.1, Chapter 3). The fitness costs of the sixteen mutant genotypes (shown in different colours) stabilizes around $\lambda = 0.05$.

utility in such settings. We demonstrated their better predictive performance in nonlinear models of viral dynamics and our results show promise for more detailed further work in this direction.

Chapter 7

Summary and conclusion

Since its discovery in 1983, there has been a significant increase in our understanding of the biology of human immunodeficiency virus. Numerous therapeutic options in the form of more than 25 antiretroviral drugs and several of their combinations have been made available to patients. Nevertheless, a cure as evinced by viral eradication has remained elusive, mainly owing to the evolutionary adaptation that HIV exhibits by acquiring drug resistant mutations. Given such inevitable resistance development and the multitude of drug combinations available to the physician, a major challenge confronting the clinical community has been the choice of optimal drugs to treat a patient, particularly in the background of previous treatment failure with other drugs. Hence, an analysis of the causes and mechanisms of treatment failure becomes crucial in the quest to decide on potential next-line drug combinations.

Mathematical models of viral dynamics and statistical models of mutation accumulation pathways have both been invaluable in enhancing our understanding of the viral life cycle, mechanisms of action of different drug classes, treatment outcomes and other aspects of viral evolution. However, the mechanistic models of virus dynamics typically lack realistic and drug-specific mutation or resistance information, that makes a direct comparison of model predictions to clinical data difficult. This imposes a limitation on their utility in assessing treatment failure with a certain drug combination. On the other hand, statistical models do not incorporate drug effects or account for temporal features explicitly, thereby disabling an analysis of time-dependent characteristics of HIV therapy such as pharmacokinetics and pharmacodynamics.

In this thesis, we developed a mechanistic model of the viral life cycle that incorporates drug-specific mutation schemes statistically learned from clinical data. Such an integrated approach is beneficial in several ways. Firstly, even structurally, it represents a unified approach of modelling the viral life cycle and drug effects, together with clinically observed mutations and resistance. Thus, it bridges the two worlds of statistical and dynamical modelling. Secondly, it provides a better understanding of the dynamics of drug-resistant mutant genotypes, the underlying competition and viral abundance at treatment failure, that would aid in assessing potential salvage therapies. We are able to estimate *in vivo* fitness characteristics of different viral mutants in the absence and presence of drugs, and examine epistatic effects between mutations. Importantly, our approach relies only on sparse clinical data, as opposed to detailed time-course measurements of viral load. Thirdly, our modelling approach easily generalizes to multiple-drug therapy and we are able to analyze how individual drugs in a combination regimen impact treatment outcome, while retaining a mechanistic framework.

Another important aspect of HIV therapy is the pharmacokinetics of antiretroviral

drugs, particularly under the multiple dosing scenario. The pharmacokinetics of a multiple dosing regimen has its challenges in terms of appropriate representation of different accumulation and half-life measures. As part of this thesis, we developed a framework that provides an integrated understanding of such different measures and enables their easy interpretation. We also coupled pharmacokinetic models to models of viral dynamics to assess the impact of changing drug concentrations.

Finally, parameter estimation and identifiability in complex nonlinear models is always a challenge. We investigated techniques to alleviate these issues in our setting. Adapting a technique from literature, we find that estimating a family of fits, instead of a single fit, and making biologically relevant inferences from the entire family leads to more robust conclusions. We also explored if well-known statistical regularization approaches such as ridge regression aid in more reliable estimates of fitness costs in virus dynamics models. While regularization methods are well-established in linear models, to the best of our knowledge, this is a first attempt at adapting them to such nonlinear models of virus dynamics. Our results show a marked improvement in predictive power of the model when such regularizers are used.

As systems biology of HIV continues to be as relevant as before, there still remain several directions of research to be inveesigated. The incorporation of stochastic or hybrid deterministic-stochastic approaches to better model low levels of mutants and the integration of virus dynamics models with drug-specific mutation schemes with patient-level models of pharmacokinetics and pharmacogenomics can greatly enhance current model predictive capabilities. The role of parameter identifiabilty in such complex models can hardly be over-stated, and an analysis of more robust methods of parameter estimation would remain a highly relevant and interesting question.

In conclusion, the work presented in this thesis contributes to bridging two distinct approaches of modelling HIV dynamics and mutations, and in doing so, enables realistic predictions of mutant dynamics during antiretroviral therapy. Our work marks another small step in the quest of using mathematical models to aid informed and individualized HIV therapy.

Bibliography

1. The top 10 causes of death, UN Fact Sheet N314, 2014.

2. Ledford H (2014) HIV rebound dashes hope of Mississippi baby cure. Nature News 10.

3. Hirsch MS, Günthard HF, Schapiro JM, Vézinet FB, Clotet B, et al. (2008) Antiretroviral drug resistance testing in adult HIV-1 infection: 2008 recommendations of an international AIDS society-USA panel. Clinical Infectious Diseases 47: 266–285.

4. Thompson MA, Aberg JA, Cahn P, Montaner JS, Rizzardini G, et al. (2010) Antiretroviral treatment of adult HIV infection: 2010 recommendations of the international AIDS society–USA panel. JAMA 304: 321–333.

5. Perelson AS, Nelson PW (1999) Mathematical analysis of HIV-1 dynamics in vivo. SIAM Review 41: 3–44.

6. Sedaghat AR, Dinoso JB, Shen L, Wilke CO, Siliciano RF (2008) Decay dynamics of HIV-1 depend on the inhibited stages of the viral life cycle. Proc Natl Acad Sci U S A 105: 4832–4837.

7. von Kleist M, Menz S, Huisinga W (2010) Drug-class specific impact of antivirals on the reproductive capacity of HIV. PLoS Comput Biol 6: e1000720.

8. Beerenwinkel N, Schmidt B, Walter H, Kaiser R, Lengauer T, et al. (2002) Diversity and complexity of HIV-1 drug resistance: A bioinformatics approach to predicting phenotype from genotype. Proc Natl Acad Sci U S A 99: 8271–8276.

9. Zhang J, Hou T, Wang W, Liu JS (2010) Detecting and understanding combinatorial mutation patterns responsible for HIV drug resistance. Proc Natl Acad Sci U S A .

10. Prosperi MC, Prosperi L, Bruselles A, Abbate I, Rozera G, et al. (2011) Combinatorial analysis and algorithms for quasispecies reconstruction using next-generation sequencing. BMC Bioinformatics 12: 5.

11. Domingo E, Escarmis C, Sevilla N, Moya A, Elena S, et al. (1996) Basic concepts in RNA virus evolution. The FASEB Journal 10: 859–864.

12. Fraser C, Lythgoe K, Leventhal GE, Shirreff G, Hollingsworth TD, et al. (2014) Virulence and pathogenesis of HIV-1 infection: an evolutionary perspective. Science 343: 1243727.

13. Wiegand R, Taylor J (1960) Kinetics of plasma drug levels after sustained release dosage. Biochemical pharmacology 3: 256–263.

14. Sheiner LB, Rosenberg B, Marathe VV (1977) Estimation of population characteristics of pharmacokinetic parameters from routine clinical data. Journal of pharmacokinetics and biopharmaceutics 5: 445–479.

15. Iwamoto M, Wenning L, Petry A, Laethem M, De Smet M, et al. (2008) Safety, tolerability, and pharmacokinetics of raltegravir after single and multiple doses in healthy subjects. Clinical Pharmacology & Therapeutics 83: 293–299.

16. Kuan-Teh Jeang (2007) HIV 1: Molecular Biology and Pathogenesis: Clinical Applications. Academic Press.

17. Mandell GL, Bennett JE, Dolin R (2010) Mandell, Douglas, and Bennett's principles and practice of infectious diseases. Churchill Livingstone/Elsevier.

18. Kallings LO (2008) The first postmodern pandemic: 25 years of HIV/AIDS. J Int Med 263: 218–243.

19. UNAIDS Report on the Global AIDS epidemic, 2013.

20. Piot P, Bartos M, Ghys PD, Walker N, Schwartländer B (2001) The global impact of HIV/AIDS. Nature 410: 968–973.

21. Pantaleo G, Graziosi C, Fauci AS (1993) The immunopathogenesis of human immunodeficiency virus infection. N Engl J Med 328: 327–335.

22. Castro KG, Ward JW, Slutsker L, Buehler JW, Jaffe HW, et al. (1993) 1993 revised classification system for HIV infection and expanded surveillance case definition for AIDS among adolescents and adults. Clin Infect Dis 17: 802–810.

23. Henderson DK, Fahey BJ, Willy M, Schmitt JM, Carey K, et al. (1990) Risk for occupational transmission of human immunodeficiency virus type 1 (HIV-1) associated with clinical exposures: A prospective evaluation. Ann Intern Med 113: 740–746.

24. De Cock KM, Fowler M, Mercier E, et al (2000) Prevention of mother-to-child hiv transmission in resource-poor countries: Translating research into policy and practice. JAMA 283: 1175–1182.

25. Attia S (2009) Sexual transmission of HIV according to viral load and antiretroviral therapy: systematic review and meta-analysis. AIDS 23: 1397.

26. Simon V, Ho DD, Abdool Karim Q (2006) HIV/AIDS epidemiology, pathogenesis, prevention, and treatment. Lancet 368: 489–504.

27. Pope M, Haase AT (2003) Transmission, acute HIV-1 infection and the quest for strategies to prevent infection. Nat Med 9: 847–852.

28. Kahn JO, Walker BD (1998) Acute human immunodeficiency virus type 1 infection. N Engl J Med 339: 33–39.

29. Branson BM, Stekler JD (2012) Detection of acute HIV infection: We can't close the window. J Infect Dis 205: 521–524.

30. Mattapallil JJ, Douek DC, Hill B, Nishimura Y, Martin M, et al. (2005) Massive infection and loss of memory CD4+T cells in multiple tissues during acute SIV infection. Nature 434: 1093–1097.

31. Ho DD (1996) Viral counts count in HIV infection. Science 272: 1124–1125.

32. Kaplan JE, Benson C, Holmes KK, Brooks JT, et al. (2009) Guidelines for prevention and treatment of opportunistic infections in HIV-infected adults and adolescents. CDC MMWR Recommendations and Reports 58.

33. Margolis L, Shattock R (2006) Selective transmission of CCR5-utilizing HIV-1: the 'gatekeeper' problem resolved? Nat Rev Micro 4: 312–317.

34. Stacey AR, Norris PJ, Qin L, Haygreen EA, Taylor E, et al. (2009) Induction of a striking systemic cytokine cascade prior to peak viremia in acute human immunodeficiency virus type 1 infection, in contrast to more modest and delayed responses in acute hepatitis b and c virus infections. J Virol 83: 3719–3733.

35. Alter G, Teigen N, Ahern R, Streeck H, Meier A, et al. (2007) Evolution of innate and adaptive effector cell functions during acute HIV-1 infection. J Infect Dis 195: 1452–1460.

36. Ward J, Bonaparte M, Sacks J, Guterman J, Fogli M, et al. (2007) HIV modulates the expression of ligands important in triggering natural killer cell cytotoxic responses on infected primary T-cell blasts. Blood 110: 1207–1214.

37. Pantaleo G, Demarest JF, Soudeyns H, Graziosi C, Denis F, et al. (1994) Major expansion of CD8+ T cells with a predominant Vβ usage during the primary immune response to HIV. Nature 370: 463–467.

38. Salazar-Gonzalez JF, Salazar MG, Keele BF, Learn GH, Giorgi EE, et al. (2009) Genetic identity, biological phenotype, and evolutionary pathways of transmitted/founder viruses in acute and early HIV-1 infection. J Exp Med 206: 1273–1289.

39. Letvin NL, Walker BD (2003) Immunopathogenesis and immunotherapy in AIDS virus infections. Nat Med 9: 861–866.

40. Sawyer SL, Emerman M, Malik HS (2004) Ancient adaptive evolution of the primate antiviral DNA-Editing enzyme APOBEC3G. PLoS Biol 2: e275.

41. Wahl SM, Greenwell-Wild T, Vázquez N (2006) HIV accomplices and adversaries in macrophage infection. J Leukoc Biol 80: 973–983.

42. Clavel F, Guetard D, Brun-Vezinet F, Chamaret S, Rey MA, et al. (1986) Isolation of a new human retrovirus from west african patients with AIDS. Science 233: 343–346.

43. Kuiken C, Leitner T, Foley B, Hahn B, Marx P, et al. (1999) HIV sequence compendium 1999. Los Alamos, New Mexico: Los Alamos National Laboratory, Theoretical Biology and Biophysics .

44. Sharp PM, Hahn BH (2011) Origins of HIV and the AIDS pandemic. Cold Spring Harb Perspect Med 1: a006841.

45. Gao F, Bailes E, Robertson DL, Chen Y, Rodenburg CM, et al. (1999) Origin of HIV-1 in the chimpanzee Pan troglodytes troglodytes. Nature 397: 436–441.

46. Chen Z, Telfier P, Gettie A, Reed P, Zhang L, et al. (1996) Genetic characterization of new west african simian immunodeficiency virus SIVsm: geographic clustering of household-derived SIV strains with human immunodeficiency virus type 2 subtypes and genetically diverse viruses from a single feral sooty mangabey troop. J Virol 70: 3617–3627.

47. Berry N, Jaffar S, van der Loeff MS, Ariyoshi K, Harding E, et al. (2002) Low level viremia and high CD4% predict normal survival in a cohort of HIV type-2-infected villagers. AIDS Res Hum Retroviruses 18: 1167–1173.

48. Evans L, Odehouri K, Moreau J, Seto D, Thomson-Honnebier G, et al. (1988) Simultaneous isolation of HIV-1 and HIV-2 from an AIDS patient. Lancet 332: 1389–1391.

49. Wainberg MA, Brenner BG (2010) Role of HIV subtype diversity in the development of resistance to antiviral drugs. Viruses 2: 2493–2508.

50. Wainberg MA (2004) HIV-1 subtype distribution and the problem of drug resistance. AIDS 18 Suppl 3: S63–68.

51. Cohen MS, Hellmann N, Levy JA, DeCock K, Lange J (2008) The spread, treatment, and prevention of HIV-1: evolution of a global pandemic. J Clin Invest 118: 1244–1254.

52. Global report: UNAIDS report on the global AIDS epidemic 2012. Joint United Nations Programme on HIV/AIDS (UNAIDS).

53. Sullivan PS, Jones JS, Baral SD (2014) The global north: HIV epidemiology in high-income countries. Curr Opin HIV AIDS 9: 199–205.

54. Brookmeyer R (2010) Measuring the HIV/AIDS epidemic: Approaches and challenges. Epidemiol Rev 32: 26–37.

55. Zhu P, Chertova E, Bess J, Lifson JD, Arthur LO, et al. (2003) Electron tomography analysis of envelope glycoprotein trimers on HIV and simian immunodeficiency virus virions. Proc Natl Acad Sci U S A 100: 15812–15817.

56. Esté JA, Telenti A (2007) HIV entry inhibitors. Lancet 370: 81–88.

57. Melikyan GB (2008) Common principles and intermediates of viral protein-mediated fusion: the HIV-1 paradigm. Retrovirology 5: 111.

58. Wilen CB, Tilton JC, Doms RW (2012) Molecular mechanisms of HIV entry. In: Rossmann MG, Rao VB, editors, Viral Molecular Machines, Springer US, 726. pp. 223–242.

59. Garwin L, Lincoln T (2010) A Century of Nature: Twenty-One Discoveries that Changed Science and the World. University of Chicago Press.

60. Jonckheere H, Anné J, De Clercq E (2000) The HIV-1 reverse transcription (RT) process as target for RT inhibitors. Med Res Rev 20: 129–154.

61. Preston BD, Poiesz BJ, Loeb LA (1988) Fidelity of HIV-1 reverse transcriptase. Science 242: 1168–1171.

62. Mansky LM, Temin HM (1995) Lower in vivo mutation rate of human immunodeficiency virus type 1 than that predicted from the fidelity of purified reverse transcriptase. J Virol 69: 5087–5094.

63. Greber UF, Fassati A (2003) Nuclear import of viral DNA genomes. Traffic 4: 136–143.

64. Wang GP, Ciuffi A, Leipzig J, Berry CC, Bushman FD (2007) HIV integration site selection: Analysis by massively parallel pyrosequencing reveals association with epigenetic modifications. Genome Res 17: 1186–1194.

65. Laspia MF, Rice AP, Mathews MB (1989) HIV-1 tat protein increases transcriptional initiation and stabilizes elongation. Cell 59: 283–292.

66. Wimmer J, Fujinaga K, Taube R, Cujec TP, Zhu Y, et al. (1999) Interactions between tat and TAR and human immunodeficiency virus replication are facilitated by human cyclin T1 but not cyclins T2a or T2b. Virology 255: 182–189.

67. Sherr CJ, Roberts JM (1995) Inhibitors of mammalian G1 cyclin-dependent kinases. Genes Dev 9: 1149–1163.

68. Chao SH, Price DH (2001) Flavopiridol inactivates P-TEFb and blocks most RNA polymerase II transcription in vivo. J Biol Chem 276: 31793–31799.

69. Agbottah E, Fuente C, Nekhai S, Barnett A, Gianella-Borradori A, et al. (2005) Antiviral activity of CYC202 in HIV-1-infected cells. J Biol Chem 280: 3029–3042.

70. Weinberger LS, Burnett JC, Toettcher JE, Arkin AP, Schaffer DV (2005) Stochastic gene expression in a lentiviral positive-feedback loop: HIV-1 tat fluctuations drive phenotypic diversity. Cell 122: 169–182.

71. Lassen KG, Ramyar KX, Bailey JR, Zhou Y, Siliciano RF (2006) Nuclear retention of multiply spliced HIV-1 RNA in resting CD4+T-cells. PLoS Pathog 2: e68.

72. Pearson R, Kim YK, Hokello J, Lassen K, Friedman J, et al. (2008) Epigenetic silencing of human immunodeficiency virus (HIV) transcription by formation of restrictive chromatin structures at the viral long terminal repeat drives the progressive entry of HIV into latency. J Virol 82: 12291–12303.

73. Sundquist WI, Krausslich HG (2012) HIV-1 assembly, budding, and maturation. Cold Spring Harb Perspect Med 2.

74. Könnyű B, Sadiq SK, Turányi T, Hírmondó R, Müller B, et al. (2013) Gag-pol processing during HIV-1 virion maturation: A systems biology approach. PLoS Comput Biol 9: e1003103.

75. Fischl MA, Richman DD, Grieco MH, Gottlieb MS, Volberding PA, et al. (1987) The efficacy of azidothymidine (AZT) in the treatment of patients with AIDS and AIDS-Related complex. a double-blind, placebo-controlled trial. N Engl J Med 317: 185–191.

76. Larder BA, Kemp SD (1989) Multiple mutations in HIV-1 reverse transcriptase confer high-level resistance to zidovudine (AZT). Science 246: 1155–1158.

77. Cadilla A, Qureshi N, Johnson DC (2010) Pediatric antiretroviral therapy. Expert review of anti-infective therapy 8: 1381–1402.

78. Kitchen VS, Skinner C, Ariyoshi K, Weber JN, Pinching AJ, et al. (1995) Safety and activity of saquinavir in HIV infection. Lancet 345: 952–955.

79. Roberts NA (1995) Drug-resistance patterns of saquinavir and other HIV proteinase inhibitors. AIDS 9 Suppl 2: 27–32.

80. Molla A, Korneyeva M, Gao Q, Vasavanonda S, Schipper PJ, et al. (1996) Ordered accumulation of mutations in HIV protease confers resistance to ritonavir. Nat Med 2: 760–766.

81. Dorr P, Westby M, Dobbs S, Griffin P, Irvine B, et al. (2005) Maraviroc (UK-427,857), a potent, orally bioavailable, and selective small-molecule inhibitor of chemokine receptor CCR5 with broad-spectrum anti-human immunodeficiency virus type 1 activity. Antimicrob Agents Chemother 49: 4721–4732.

82. Roche M, Jakobsen MR, Sterjovski J, Ellett A, Posta F, et al. (2011) HIV-1 escape from the CCR5 antagonist maraviroc associated with an altered and less-efficient mechanism of gp120-CCR5 engagement that attenuates macrophage tropism. J Virol 85: 4330–4342.

83. Lalezari JP, Henry K, O'Hearn M, Montaner JS, Piliero PJ, et al. (2003) Enfuvirtide, an HIV-1 fusion inhibitor, for drug-resistant HIV infection in North and South America. N Engl J Med 348: 2175–2185.

84. Maggi P, Ladisa N, Cinori E, Altobella A, Pastore G, et al. (2004) Cutaneous injection site reactions to long-term therapy with enfuvirtide. J Antimicrob Chemother 53: 678–681.

85. Skowron G, Ogden R (2007) Reverse Transcriptase Inhibitors in HIV/AIDS Therapy. Springer.

86. Brinkman K, Smeitink JA, Romijn JA, Reiss P (1999) Mitochondrial toxicity induced by nucleoside-analogue reverse-transcriptase inhibitors is a key factor in the pathogenesis of antiretroviral-therapy-related lipodystrophy. Lancet 354: 1112–1115.

87. Usach I, Melis V, Peris JE (2013) Non-nucleoside reverse transcriptase inhibitors: a review on pharmacokinetics, pharmacodynamics, safety and tolerability. J Int AIDS Soc 16.

88. Smith RL, de Boer R, Brul S, Budovskaya Y, van Spek H (2012) Premature and accelerated aging: HIV or HAART? Frontiers in genetics 3.

89. Grinsztejn B, Nguyen BY, Katlama C, Gatell JM, Lazzarin A, et al. (2007) Safety and efficacy of the HIV-1 integrase inhibitor raltegravir (MK-0518) in treatment-experienced patients with multidrug-resistant virus: a phase II randomised controlled trial. Lancet 369: 1261–1269.

90. Shimura K, Kodama E, Sakagami Y, Matsuzaki Y, Watanabe W, et al. (2008) Broad antiretroviral activity and resistance profile of the novel human immunodeficiency virus integrase inhibitor elvitegravir (JTK-303/GS-9137). J Virol 82: 764–774.

91. van Lunzen J, Maggiolo F, Arribas JR, Rakhmanova A, Yeni P, et al. (2012) Once daily dolutegravir (S/GSK1349572) in combination therapy in antiretroviral-naive adults with HIV: planned interim 48 week results from SPRING-1, a dose-ranging, randomised, phase 2b trial. Lancet Infect Dis 12: 111–118.

92. Rabi SA, Laird GM, Durand CM, Laskey S, Shan L, et al. (2013) Multi-step inhibition explains HIV-1 protease inhibitor pharmacodynamics and resistance. J Clin Invest 123: 3848–3860.

93. Zeldin RK, Petruschke RA (2004) Pharmacological and therapeutic properties of ritonavir-boosted protease inhibitor therapy in HIV-infected patients. J Antimicrob Chemother 53: 4–9.

94. Walmsley S (2007) Protease inhibitor-based regimens for HIV therapy: safety and efficacy. J Acquir Immune Defic Syndr 45: 5–13.

95. Salzwedel K, Martin DE, Sakalian M (2007) Maturation inhibitors: a new therapeutic class targets the virus structure. AIDS Rev 9: 162–172.

96. Gulick RM, Mellors JW, Havlir D, et al (1998) Simultaneous vs sequential initiation of therapy with indinavir, zidovudine, and lamivudine for HIV-1 infection: 100-week follow-up. JAMA 280: 35–41.

97. Gulick RM, Mellors JW, Havlir D, Eron JJ, Meibohm A, et al. (2000) 3-year suppression of HIV viremia with indinavir, zidovudine, and lamivudine. Ann Intern Med 133: 35–39.

98. Hammer SM, Katzenstein DA, Hughes MD, Gundacker H, Schooley RT, et al. (1996) A trial comparing nucleoside monotherapy with combination therapy in HIV-Infected adults with CD4 cell counts from 200 to 500 per cubic millimeter. N Engl J Med 335: 1081–1090.

99. Kaufmann GR, Perrin L, Pantaleo G, et al (2003) CD4+T-lymphocyte recovery in individuals with advanced HIV-1 infection receiving potent antiretroviral therapy for 4 years: The Swiss HIV cohort study. Arch Intern Med 163: 2187–2195.

100. Mocroft A, Phillips A, Gatell J, Ledergerber B, Fisher M, et al. (2007) Normalisation of CD4 counts in patients with HIV-1 infection and maximum virological suppression who are taking combination antiretroviral therapy: an observational cohort study. The Lancet 370: 407–413.

101. Westby M, van der Ryst E (2005) CCR5 antagonists: host-targeted antivirals for the treatment of HIV infection. Antivir Chem Chemother 16: 339–354.

102. Zhou H, Xu M, Huang Q, Gates AT, Zhang XD, et al. (2008) Genome-scale RNAi screen for host factors required for HIV replication. Cell Host & Microbe 4: 495–504.

103. Chao SH, Fujinaga K, Marion JE, Taube R, Sausville EA, et al. (2000) Flavopiridol inhibits p-TEFb and blocks HIV-1 replication. J Biol Chem 275: 28345–28348.

104. Johnston MI, Fauci AS (2011) HIV vaccine development — improving on natural immunity. N Engl J Med 365: 873–875.

105. Burton DR, Ahmed R, Barouch DH, Butera ST, Crotty S, et al. (2012) A blueprint for HIV vaccine discovery. Cell Host & Microbe 12: 396–407.

106. Walker LM, Burton DR (2010) Rational antibody-based HIV-1 vaccine design: current approaches and future directions. Curr Opin Immunol 22: 358–366.

107. Baeten JM, Donnell D, Ndase P, Mugo NR, Campbell JD, et al. (2012) Antiretroviral prophylaxis for HIV prevention in heterosexual men and women. N Engl J Med 367: 399–410.

108. Cohen J (2007) Promising AIDS vaccine's failure leaves field reeling. Science 318: 28–29.

109. Ledford H (2007) HIV vaccine may raise risk. Nature 450: 325.

110. Fauci AS, Johnston MI, Dieffenbach CW, Burton DR, Hammer SM, et al. (2008) HIV vaccine research: The way forward. Science 321: 530–532.

111. Ho DD, Neumann AU, Perelson AS, Chen W, Leonard JM, et al. (1995) Rapid turnover of plasma virions and CD4 lymphocytes in HIV-1 infection. Nature 373: 123–126.

112. Wei X, Ghosh SK, Taylor ME, Johnson VA, Emini EA, et al. (1995) Viral dynamics in human immunodeficiency virus type 1 infection. Nature 373: 117–122.

113. Coffin JM (1995) HIV population dynamics in vivo: implications for genetic variation, pathogenesis, and therapy. Science 267: 483–489.

114. Perelson AS, Neumann AU, Markowitz M, Leonard JM, Ho DD (1996) HIV-1 dynamics in vivo: Virion clearance rate, infected cell life-span, and viral generation time. Science 271: 1582–1586.

115. Perelson AS, Essunger P, Cao Y, Vesanen M, Hurley A, et al. (1997) Decay characteristics of HIV-1-infected compartments during combination therapy. Nature 387: 188–191.

116. Perelson AS, Ribeiro RM (2013) Modeling the within-host dynamics of HIV infection. BMC Biology 11: 96.

117. De Boer RJ, Perelson AS (1998) Target cell limited and immune control models of HIV infection: A comparison. Journal of Theoretical Biology 190: 201–214.

118. Nowak M, May RM (2000) Virus Dynamics: Mathematical Principles of Immunology and Virology. Oxford University Press.

119. Kim H, Perelson AS (2006) Viral and latent reservoir persistence in HIV-1–Infected patients on therapy. PLoS Comput Biol 2: e135.

120. Rong L, Perelson AS (2009) Modeling HIV persistence, the latent reservoir, and viral blips. Journal of Theoretical Biology 260: 308–331.

121. Shen L, Peterson S, Sedaghat AR, McMahon MA, Callender M, et al. (2008) Dose-response curve slope sets class-specific limits on inhibitory potential of anti-HIV drugs. Nat Med 14: 762–766.

122. von Kleist M, Menz S, Stocker H, Arasteh K, Schütte C, et al. (2011) HIV quasispecies dynamics during pro-active treatment switching: Impact on multi-drug resistance and resistance archiving in latent reservoirs. PLoS One 6: e18204.

123. Abram ME, Ferris AL, Shao W, Alvord WG, Hughes SH (2010) Nature, position, and frequency of mutations made in a single cycle of HIV-1 replication. J Virol 84: 9864–9878.

124. Goldberg DE, Siliciano RF, Jacobs J William R (2012) Outwitting evolution: fighting drug-resistant TB, malaria, and HIV. Cell 148: 1271–1283.

125. Foulkes AS, De Gruttola V (2003) Characterizing the progression of viral mutations over time. J Am Statist Assoc 98: 859–867.

126. Beerenwinkel N, Rahnenführer J, Kaiser R, Hoffmann D, Selbig J, et al. (2005) Mtreemix: a software package for learning and using mixture models of mutagenetic trees. Bioinformatics 21: 2106–2107.

127. Beerenwinkel N, Däumer M, Sing T, Rahnenführer J, Lengauer T, et al. (2005) Estimating HIV evolutionary pathways and the genetic barrier to drug resistance. J Infect Dis 191: 1953–1960.

128. Lawyer G, Altmann A, Thielen A, Zazzi M, Sönnerborg A, et al. (2011) HIV-1 mutational pathways under multidrug therapy. AIDS Res Ther 8: 26.

129. Rosen-Zvi M, Altmann A, Prosperi M, Aharoni E, Neuvirth H, et al. (2008) Selecting anti-HIV therapies based on a variety of genomic and clinical factors. Bioinformatics 24: 399–406.

130. Segal MR, Barbour JD, Grant RM (2004) Relating HIV-1 sequence variation to replication capacity via trees and forests. Stat Appl Genet Molec Biol 3.

131. Rhee SY, Taylor J, Wadhera G, Ben-Hur A, Brutlag DL, et al. (2006) Genotypic predictors of human immunodeficiency virus type 1 drug resistance. Proc Natl Acad Sci U S A 103: 17355–17360.

132. De Luca A, Cingolani A, Di Giambenedetto S, Trotta MP, Baldini F, et al. (2003) Variable prediction of antiretroviral treatment outcome by different systems for interpreting genotypic human immunodeficiency virus type 1 drug resistance. J Infect Dis 187: 1934–1943.

133. Deforche K, Cozzi-Lepri A, Theys K, Clotet B, Camacho RJ, et al. (2008) Modelled in vivo HIV fitness under drug selective pressure and estimated genetic barrier towards resistance are predictive for virological response. Antivir Ther 13: 399–407.

134. Prosperi MCF, Altmann A, Rosen-Zvi M, Aharoni E, Borgulya G, et al. (2009) Investigation of expert rule bases, logistic regression, and non-linear machine learning techniques for predicting response to antiretroviral treatment. Antivir Ther 14: 433–442.

135. Beerenwinkel N, Montazeri H, Schuhmacher H, Knupfer P, von Wyl V, et al. (2013) The individualized genetic barrier predicts treatment response in a large cohort of HIV-1 infected patients. PLoS Comput Biol 9: e1003203.

136. Beerenwinkel N, Rahnenführer J, Däumer M, Hoffmann D, Kaiser R, et al. (2005) Learning multiple evolutionary pathways from cross-sectional data. Journal of Computational Biology 12: 584–598.

137. Pearl J (1988) Probabilistic Reasoning in Intelligent Systems: Networks of Plausible Inference. Morgan Kaufmann Publishers.

138. Neapolitan RE (2009) Probabilistic Methods for Bioinformatics: with an Introduction to Bayesian Networks. Morgan Kaufmann Publishers.

139. Beerenwinkel N, Eriksson N, Sturmfels B (2007) Conjunctive Bayesian networks. Bernoulli 13: 893–909.

140. Beerenwinkel N, Sullivant S (2009) Markov models for accumulating mutations. Biometrika 96: 645–661.

141. Panel on Antiretroviral Guidelines for Adults and Adolescents (2013). Guidelines for the use of antiretroviral agents in HIV-1-infected adults and adolescents.

142. DeGruttola V, Dix L, D'Aquila R, Holder D, Phillips A, et al. (2000) The relation between baseline HIV drug resistance and response to antiretroviral therapy: reanalysis of retrospective and prospective studies using a standardized data analysis plan. Antivir Ther 5: 41–48.

143. Wang D, Larder B (2003) Enhanced prediction of lopinavir resistance from genotype by use of artificial neural networks. J Infect Dis 188: 653–660.

144. Beerenwinkel N, Däumer M, Oette M, Korn K, Hoffmann D, et al. (2003) Geno2pheno: estimating phenotypic drug resistance from HIV-1 genotypes. Nucl Acids Res 31: 3850–3855.

145. Percival D, Roeder K, Rosenfeld R, Wasserman L (2011) Structured, sparse regression with application to HIV drug resistance. Ann Appl Stat 5: 628–644.

146. Beerenwinkel N, Knupfer P, Tresch A (2011) Learning monotonic genotype-phenotype maps. Stat Appl Genet Molec Biol 10: 1–27.

147. Mair P, Hornik K, de Leeuw J (2009) Isotone optimization in R: Pool-adjacent-violators algorithm (PAVA) and active set methods. Journal of Statistical Software 32: 1–24.

148. Rhee SY, Gonzales MJ, Kantor R, Betts BJ, Ravela J, et al. (2003) Human immunodeficiency virus reverse transcriptase and protease sequence database. Nucleic Acids Res 31: 298–303.

149. Petropoulos CJ, Parkin NT, Limoli KL, Lie YS, Wrin T, et al. (2000) A novel phenotypic drug susceptibility assay for human immunodeficiency virus type 1. Antimicrob Agents Chemother 44: 920–928.

150. Hertogs K, Béthune MP, Miller V, Ivens T, Schel P, et al. (1998) A rapid method for simultaneous detection of phenotypic resistance to inhibitors of protease and reverse transcriptase in recombinant human immunodeficiency virus type 1 isolates from patients treated with antiretroviral drugs. Antimicrob Agents Chemother 42: 269–276.

151. Meynard JL, Vray M, Morand-Joubert L, Race E, Descamps D, et al. (2002) Phenotypic or genotypic resistance testing for choosing antiretroviral therapy after treatment failure: a randomized trial. AIDS 16: 727–736.

152. Frentz D, Boucher CAB, Assel M, De Luca A, Fabbiani M, et al. (2010) Comparison of HIV-1 genotypic resistance test interpretation systems in predicting virological outcomes over time. PLoS ONE 5: e11505.

153. Saigo H, Altmann A, Bogojeska J, Müller F, Nowozin S, et al. (2011) Learning from past treatments and their outcome improves prediction of in vivo response to anti-hiv therapy. Statistical applications in genetics and molecular biology 10.

154. Orr HA (2009) Fitness and its role in evolutionary genetics. Nat Rev Genet 10: 531–539.

155. Domingo E (2006) Quasispecies: Concept and Implications for Virology: Concept and Implications for Virology. Springer.

156. Sharpe FR, Lotka AJ (1911) A problem in age-distribution. The London, Edinburgh, and Dublin Philosophical Magazine and Journal of Science 21: 435–438.

157. Heffernan JM, Smith RJ, Wahl LM (2005) Perspectives on the basic reproductive ratio. J R Soc Interface 2: 281–293.

158. Ribeiro RM, Qin L, Chavez LL, Li D, Self SG, et al. (2010) Estimation of the initial viral growth rate and basic reproductive number during acute HIV-1 infection. J Virol 84: 6096–6102.

159. Alexander HK, Bonhoeffer S (2012) Pre-existence and emergence of drug resistance in a generalized model of intra-host viral dynamics. Epidemics 4: 187–202.

160. Rosenbloom DIS, Hill AL, Rabi SA, Siliciano RF, Nowak MA (2012) Antiretroviral dynamics determines HIV evolution and predicts therapy outcome. Nat Med 18: 1378–1385.

161. Stadler T, Kouyos R, Wyl Vv, Yerly S, Böni J, et al. (2012) Estimating the basic reproductive number from viral sequence data. Mol Biol Evol 29: 347–357.

162. Hinkley T, Martins J, Chappey C, Haddad M, Stawiski E, et al. (2011) A systems analysis of mutational effects in HIV-1 protease and reverse transcriptase. Nat Genet 43: 487–489.

163. Naeger LK, Margot NA, Miller MD (2001) Increased drug susceptibility of HIV-1 reverse transcriptase mutants containing M184V and zidovudine-associated mutations: analysis of enzyme processivity, chain-terminator removal and viral replication. Antivir Ther 6: 115–126.

164. Menzo S, Monachetti A, Balotta C, Corvasce S, Rusconi S, et al. (2003) Processivity and drug-dependence of HIV-1 protease: determinants of viral fitness in variants resistant to protease inhibitors. AIDS 17: 663–671.

165. Dykes C, Demeter LM (2007) Clinical significance of human immunodeficiency virus type 1 replication fitness. Clin Microbiol Rev 20: 550–578.

166. Mammano F, Petit C, Clavel F (1998) Resistance-associated loss of viral fitness in human immunodeficiency virus type 1: Phenotypic analysis of protease andgag coevolution in protease inhibitor-treated patients. J Virol 72: 7632–7637.

167. Deeks SG, Wrin T, Liegler T, Hoh R, Hayden M, et al. (2001) Virologic and immunologic consequences of discontinuing combination antiretroviral-drug therapy in HIV-Infected patients with detectable viremia. N Engl J Med 344: 472–480.

168. Holland JJ, Torre JCdl, Clarke DK, Duarte E (1991) Quantitation of relative fitness and great adaptability of clonal populations of RNA viruses. J Virol 65: 2960–2967.

169. Collins JA, Thompson MG, Paintsil E, Ricketts M, Gedzior J, et al. (2004) Competitive fitness of nevirapine-resistant human immunodeficiency virus type 1 mutants. J Virol 78: 603–611.

170. Bates M, Wrin T, Huang W, Petropoulos C, Hellmann N (2003) Practical applications of viral fitness in clinical practice. Curr Opin Infect Dis 16: 11–18.

171. Martinez JP, Bocharov G, Ignatovich A, Reiter J, Dittmar MT, et al. (2011) Fitness ranking of individual mutants drives patterns of epistatic interactions in HIV-1. PLoS ONE 6: e18375.

172. Delwart EL, Gordon CJ (1997) Tracking changes in HIV-1 envelope quasispecies using DNA heteroduplex analysis. Methods 12: 348–354.

173. Rangel HR, Weber J, Chakraborty B, Gutierrez A, Marotta ML, et al. (2003) Role of the human immunodeficiency virus type 1 envelope gene in viral fitness. J Virol 77: 9069–9073.

174. Voronin Y, Overbaugh J, Emerman M (2005) Simian immunodeficiency virus variants that differ in pathogenicity differ in fitness under rapid cell turnover conditions. J Virol 79: 15091–15098.

175. Kouyos RD, von Wyl V, Hinkley T, Petropoulos CJ, Haddad M, et al. (2011) Assessing predicted HIV-1 replicative capacity in a clinical setting. PLoS Pathog 7: e1002321.

176. Barbour JD, Hecht FM, Little SJ, Markowitz M, Daar ES, et al. (2006) Greater CD4 T-cell gains after one year of antiretroviral therapy are associated with lower HIV-1 pol replication capacity. AIDS 20: 2123–2125.

177. Barbour JD, Hecht FM, Wrin T, Segal MR, Ramstead CA, et al. (2004) Higher CD4+ T- cell counts associated with low viral pol replication capacity among treatment-naive adults in early HIV-1 infection. J Infect Dis 190: 251–256.

178. A dual infection/competition .

179. Deeks SG, Martin JN, Sinclair E, Harris J, Neilands TB, et al. (2004) Strong cell-mediated immune responses are associated with the maintenance of low-level viremia in Antiretroviral–Treated individuals with drug-resistant human immunodeficiency virus type 1. J Infect Dis 189: 312–321.

180. Gallant JE (2006) The M184V mutation: what it does, how to prevent it, and what to do with it when it's there. The AIDS Reader 16: 556–559.

181. B Berkhout (1999) Proposed alternatives for the use of anti-HIV drugs. Drug Resist Updates 2: 69–70.

182. Loeb LA, Essigmann JM, Kazazi F, Zhang J, Rose KD, et al. (1999) Lethal mutagenesis of HIV with mutagenic nucleoside analogs. PNAS 96: 1492–1497.

183. Eigen M (2002) Error catastrophe and antiviral strategy. PNAS 99: 13374–13376.

184. Tripathi K, Balagam R, Vishnoi NK, Dixit NM (2012) Stochastic simulations suggest that HIV-1 survives close to its error threshold. PLoS Comput Biol 8: e1002684.

185. Wagner BG, Garcia-Lerma JG, Blower S (2012) Factors limiting the transmission of HIV mutations conferring drug resistance: fitness costs and genetic bottlenecks. Sci Rep 2.

186. Harrigan PR, Bloor S, Larder BA (1998) Relative replicative fitness of zidovudine-resistant human immunodeficiency virus type 1 isolates in vitro. J Virol 72: 3773–3778.

187. Marée AFM, Keulen W, Boucher CAB, Boer RJD (2000) Estimating relative fitness in viral competition experiments. J Virol 74: 11067–11072.

188. Bonhoeffer S, Barbour AD, Boer RJD (2002) Procedures for reliable estimation of viral fitness from time-series data. Proc R Soc Lond B 269: 1887–1893.

189. Marconi V, Bonhoeffer S, Paredes R, Lu J, Hoh R, et al. (2008) Viral dynamics and in vivo fitness of HIV-1 in the presence and absence of enfuvirtide. J Acquir Immune Defic Syndr 48: 572–576.

190. Paredes R, Sagar M, Marconi VC, Hoh R, Martin JN, et al. (2009) In vivo fitness cost of the M184V mutation in multidrug-resistant human immunodeficiency virus type 1 in the absence of lamivudine. J Virol 83: 2038–2043.

191. Karlsson AC, Deeks SG, Barbour JD, Heiken BD, Younger SR, et al. (2003) Dual pressure from antiretroviral therapy and cell-mediated immune response on the human immunodeficiency virus type 1 protease gene. J Virol 77: 6743–6752.

192. Villena C, Prado JG, Puertas MC, Martínez MÁ, Clotet B, et al. (2007) Relative fitness and replication capacity of a multinucleoside analogue-resistant clinical human immunodeficiency virus type 1 isolate with a deletion of codon 69 in the reverse transcriptase coding region. J Virol 81: 4713–4721.

193. Frost SDW, Nijhuis M, Schuurman R, Boucher CAB, Brown AJL (2000) Evolution of lamivudine resistance in human immunodeficiency virus type 1-infected individuals: the relative roles of drift and selection. J Virol 74: 6262–6268.

194. Goudsmit J, Ronde Ad, Rooij Ed, Boer Rd (1997) Broad spectrum of in vivo fitness of human immunodeficiency virus type 1 subpopulations differing at reverse transcriptase codons 41 and 215. J Virol 71: 4479–4484.

195. Devereux HL, Emery VC, Johnson MA, Loveday C (2001) Replicative fitness in vivo of HIV-1 variants with multiple drug resistance-associated mutations. Journal of Medical Virology 65: 218–224.

196. Vaidya NK, Rong L, Marconi VC, Kuritzkes DR, Deeks SG, et al. (2010) Treatment-mediated alterations in HIV fitness preserve CD4+ t cell counts but have minimal effects on viral load. PLoS Comput Biol 6: e1001012.

197. Deforche K, Camacho R, Laethem KV, Lemey P, Rambaut A, et al. (2008) Estimation of an in vivo fitness landscape experienced by HIV-1 under drug selective pressure useful for prediction of drug resistance evolution during treatment. Bioinformatics 24: 34–41.

198. Ribeiro RM, Bonhoeffer S, Nowak MA (1998) The frequency of resistant mutant virus before antiviral therapy. AIDS 12: 461–465.

199. Rong L, Feng Z, Perelson AS (2007) Emergence of HIV-1 drug resistance during antiretroviral treatment. Bull Math Biol 69: 2027–2060.

200. Stilianakis NI, Boucher CA, Jong MDD, Leeuwen RV, Schuurman R, et al. (1997) Clinical data sets of human immunodeficiency virus type 1 reverse transcriptase-resistant mutants explained by a mathematical model. J Virol 71: 161–168.

201. Beerenwinkel N, Lengauer T, Däumer M, Kaiser R, Walter H, et al. (2003) Methods for optimizing antiviral combination therapies. Bioinformatics 19: 16–25.

202. Murray JM, Perelson AS (2005) Human immunodeficiency virus: Quasi-species and drug resistance. Multiscale Model Simul 3: 300–311.

203. Gopalakrishnan S, Montazeri H, Menz S, Beerenwinkel N, Huisinga W (2014) Estimating HIV-1 fitness characteristics from cross-sectional genotype data. PLoS Comput Biol 10: e1003886.

204. von Kleist M, Metzner P, Marquet R, Schütte C (2012) HIV-1 polymerase inhibition by nucleoside analogs: Cellular- and kinetic parameters of efficacy, susceptibility and resistance selection. PLoS Comput Biol 8: e1002359.

205. Korn K, Reil H, Walter H, Schmidt B (2003) Quality control trial for human immunodeficiency virus type 1 drug resistance testing using clinical samples reveals problems with detecting minority species and interpretation of test results. J Clin Microbiol 41: 3559–3565.

206. Dudley DM, Chin EN, Bimber BN, Sanabani SS, Tarosso LF, et al. (2012) Low-cost ultra-wide genotyping using Roche/454 pyrosequencing for surveillance of HIV drug resistance. PLoS ONE 7: e36494.

207. Nelder JA, Mead R (1965) A simplex method for function minimization. The Computer Journal 7: 308–313.

208. Yahi N, Tamalet C, Tourrès C, Tivoli N, Ariasi F, et al. (1999) Mutation patterns of the reverse transcriptase and protease genes in human immunodeficiency virus type 1-infected patients undergoing combination therapy: Survey of 787 sequences. J Clin Microbiol 37: 4099–4106.

209. Hanna GJ, Johnson VA, Kuritzkes DR, Richman DD, Brown AJL, et al. (2000) Patterns of resistance mutations selected by treatment of human immunodeficiency virus type 1 infection with zidovudine, didanosine, and nevirapine. J Infect Dis 181: 904–911.

210. Cozzi-Lepri A, Ruiz L, Loveday C, Phillips AN, Clotet B, et al. (2005) Thymidine analogue mutation profiles: factors associated with acquiring specific profiles and their impact on the virological response to therapy. Antivir Ther 10: 791–802.

211. Loveday C, Kaye S, Tenant-Flowers M, Semple M, Ayliffe U, et al. (1995) HIV-1 RNA serum-load and resistant viral genotypes during early zidovudine therapy. Lancet 345: 820–824.

212. Martinez-Picado J, Savara AV, Sutton L, D'Aquila RT (1999) Replicative fitness of protease inhibitor-resistant mutants of human immunodeficiency virus type 1. J Virol 73: 3744–3752.

213. Harrigan PR, Kinghorn I, Bloor S, Kemp SD, Nájera I, et al. (1996) Significance of amino acid variation at human immunodeficiency virus type 1 reverse transcriptase residue 210 for zidovudine susceptibility. J Virol 70: 5930–5934.

214. Hu Z, Giguel F, Hatano H, Reid P, Lu J, et al. (2006) Fitness comparison of thymidine analog resistance pathways in human immunodeficiency virus type 1. J Virol 80: 7020–7027.

215. Marcelin AG, Delaugerre C, Wirden M, Viegas P, Simon A, et al. (2004) Thymidine analogue reverse transcriptase inhibitors resistance mutations profiles and association to other nucleoside reverse transcriptase inhibitors resistance mutations observed in the context of virological failure. J Med Virol 72: 162–165.

216. Japour AJ, Welles S, D'Aquila RT, Johnson VA, Richman DD, et al. (1995) Prevalence and clinical significance of zidovudine resistance mutations in human immunodeficiency virus isolated from patients after long-term zidovudine treatment. J Infect Dis 171: 1172–1179.

217. Cong Me, Heneine W, García-Lerma JG (2007) The fitness cost of mutations associated with human immunodeficiency virus type 1 drug resistance is modulated by mutational interactions. J Virol 81: 3037–3041.

218. Bonhoeffer S, Chappey C, Parkin NT, Whitcomb JM, Petropoulos CJ (2004) Evidence for positive epistasis in HIV-1. Science 306: 1547–1550.

219. Wang K, Mittler JE, Samudrala R (2006) Comment on "Evidence for positive epistasis in HIV-1". Science 312: 848–848.

220. Bonhoeffer S, Chappey C, Parkin NT, Whitcomb JM, Petropoulos CJ (2006) Response to comment on "Evidence for positive epistasis in HIV-1". Science 312: 848–848.

221. de Jong MD, Veenstra J, Stilianakis NI, Schuurman R, Lange JM, et al. (1996) Host-parasite dynamics and outgrowth of virus containing a single K70R amino acid change in reverse transcriptase are responsible for the loss of human immunodeficiency virus type 1 RNA load suppression by zidovudine. Proc Natl Acad Sci U S A 93: 5501–5506.

222. Gulick RM, Mellors JW, Havlir D, Eron JJ, Gonzalez C, et al. (1997) Treatment with indinavir, zidovudine, and lamivudine in adults with human immunodeficiency virus infection and prior antiretroviral therapy. N Engl J Med 337: 734–739.

223. Nijhuis M, Schuurman R, de Jong D, Erickson J, Gustchina E, et al. (1999) Increased fitness of drug resistant HIV-1 protease as a result of acquisition of compensatory mutations during suboptimal therapy. AIDS 13: 2349–2359.

224. Quiñones-Mateu ME, Arts EJ (2002) Fitness of drug resistant HIV-1: methodology and clinical implications. Drug Resistance Updates 5: 224–233.

225. Berkhout B (1999) HIV-1 evolution under pressure of protease inhibitors: Climbing the stairs of viral fitness. J Biomed Sci 6: 298–305.

226. van Maarseveen NM, Wensing AMJ, Jong Dd, Taconis M, Borleffs JCC, et al. (2007) Persistence of HIV-1 variants with multiple protease inhibitor (PI)-Resistance mutations in the absence of PI therapy can be explained by compensatory fixation. J Infect Dis 195: 399–409.

227. Mammano F, Trouplin V, Zennou V, Clavel F (2000) Retracing the evolutionary pathways of human immunodeficiency virus type 1 resistance to protease inhibitors: Virus fitness in the absence and in the presence of drug. J Virol 74: 8524–8531.

228. Henderson GJ, Lee SK, Irlbeck DM, Harris J, Kline M, et al. (2012) Interplay between single resistance-associated mutations in the HIV-1 protease and viral infectivity, protease activity, and inhibitor sensitivity. Antimicrob Agents Chemother 56: 623–633.

229. Wu H, Ding AA, De Gruttola V (1998) Estimation of HIV dynamic parameters. Statistics in medicine 17: 2463–2485.

230. Huang Y, Liu D, Wu H (2006) Hierarchical bayesian methods for estimation of parameters in a longitudinal HIV dynamic system. Biometrics 62: 413–423.

231. Alfonsi A, Cancès E, Turinici G, Ventura BD, Huisinga W (2005) Exact simulation of hybrid stochastic and deterministic models for biochemical systems. ESAIM Proc 14: 1–23.

232. Arora P, Dixit NM (2009) Timing the emergence of resistance to anti-hiv drugs with large genetic barriers. PLoS Comput Biol 5: e1000305.

233. Sheiner LB, Steimer JL (2000) Pharmacokinetic/Pharmacodynamic modeling in drug development. Ann Rev Pharmacol Toxicol 40: 67–95.

234. Zhang YM, Imamichi H, Imamichi T, Lane HC, Falloon J, et al. (1997) Drug resistance during indinavir therapy is caused by mutations in the protease gene and in its gag substrate cleavage sites. J Virol 71: 6662–6670.

235. Doyon L, Payant C, Brakier-Gingras L, Lamarre D (1998) Novel gag-pol frameshift site in human immunodeficiency virus type 1 variants resistant to protease inhibitors. J Virol 72: 6146–6150.

236. Fuente C, Maddukuri A, Kehn K, Baylor S, Deng L, et al. (2003) Pharmacological cyclin-dependent kinase inhibitors as HIV-1 antiviral therapeutics. Current HIV Research 1: 131–152.

237. Bliss CI (1939) The toxicity of poisons applied jointly. Annals of Applied Biology 26: 585–615.

238. Loewe S (1926) Effect of combinations : mathematical basis of problem. Arch Exp Pathol Pharmakol 114: 313–326.

239. Jilek BL, Zarr M, Sampah ME, Rabi SA, Bullen CK, et al. (2012) A quantitative basis for antiretroviral therapy for HIV-1 infection. Nat Med 18: 446–451.

240. Petrella M, Wainberg MA (2002) Might the M184V substitution in HIV-1 RT confer clinical benefit? AIDS Rev 4: 224–232.

241. Wainberg MA (2004) The impact of the M184V substitution on drug resistance and viral fitness. Expert Rev Anti Infect Ther 2: 147–151.

242. Deval J, White KL, Miller MD, Parkin NT, Courcambeck J, et al. (2004) Mechanistic basis for reduced viral and enzymatic fitness of HIV-1 reverse transcriptase containing both K65R and M184V mutations. J Biol Chem 279: 509–516.

243. Coley W, Kehn-Hall K, Duyne RV, Kashanchi F (2009) Novel HIV-1 therapeutics through targeting altered host cell pathways. Expert Opin Biol Ther 9: 1369–1382.

244. Wang S, Fischer PM (2008) Cyclin-dependent kinase 9: a key transcriptional regulator and potential drug target in oncology, virology and cardiology. Trends in Pharmacological Sciences 29: 302–313.

245. Harbison CT, Gordon DB, Lee TI, Rinaldi NJ, Macisaac KD, et al. (2004) Transcriptional regulatory code of a eukaryotic genome. Nature 431: 99–104.

246. Core LJ, Lis JT (2008) Transcription regulation through promoter-proximal pausing of RNA polymerase II. Science 319: 1791–1792.

247. Hargreaves DC, Horng T, Medzhitov R (2009) Control of inducible gene expression by signal-dependent transcriptional elongation. Cell 138: 129–145.

248. Ramakrishnan R, Chiang K, Liu H, Budhiraja S, Donahue H, et al. (2012) Making a short story long: Regulation of p-TEFb and HIV-1 transcriptional elongation in CD4+ t lymphocytes and macrophages. Biology 1: 94–115.

249. Hunter T, Pines J (1994) Cyclins and cancer II: cyclin D and CDK inhibitors come of age. Cell 79: 573–582.

250. Karn J (2011) The molecular biology of HIV latency: Breaking and restoring the tat-dependent transcriptional circuit. Curr Opin HIV AIDS 6: 4–11.

251. Bark-Jones SJ, Webb HM, West MJ (2005) EBV EBNA 2 stimulates CDK9-dependent transcription and RNA polymerase II phosphorylation on serine 5. Oncogene 25: 1775–1785.

252. Shimizu S, Urano E, Futahashi Y, Miyauchi K, Isogai M, et al. (2007) Inhibiting lentiviral replication by HEXIM1, a cellular negative regulator of the CDK9/cyclin T complex:. AIDS 21: 575–582.

253. Carlson BA, Dubay MM, Sausville EA, Brizuela L, Worland PJ (1996) Flavopiridol induces G1 arrest with inhibition of cyclin-dependent kinase (CDK) 2 and CDK4 in human breast carcinoma cells. Cancer Res 56: 2973–2978.

254. Senderowicz AM, Headlee D, Stinson SF, Lush RM, Kalil N, et al. (1998) Phase I trial of continuous infusion flavopiridol, a novel cyclin-dependent kinase inhibitor, in patients with refractory neoplasms. J Clin Oncol 16: 2986–2999.

255. Chiu YL, Cao H, Jacque JM, Stevenson M, Rana TM (2004) Inhibition of human immunodeficiency virus type 1 replication by RNA interference directed against

human transcription elongation factor p-TEFb (CDK9/CyclinT1). J Virol 78: 2517–2529.

256. Guendel I, Agbottah ET, Kehn-Hall K, Kashanchi F (2010) Inhibition of human immunodeficiency virus type-1 by CDK inhibitors. AIDS Res Ther 7: 1–14.

257. Heredia A, Natesan S, Le NM, Medina-Moreno S, Zapata JC, et al. (2014) Indirubin 3'-monoxime, from a chinese traditional herbal formula, suppresses viremia in humanized mice infected with multidrug-resistant HIV. AIDS Research and Human Retroviruses 30: 403–406.

258. Han Y, Lassen K, Monie D, Sedaghat AR, Shimoji S, et al. (2004) Resting CD4+ t cells from human immunodeficiency virus type 1 (HIV-1)-infected individuals carry integrated HIV-1 genomes within actively transcribed host genes. J Virol 78: 6122–6133.

259. Vatakis DN, Kim S, Kim N, Chow SA, Zack JA (2009) Human immunodeficiency virus integration efficiency and site selection in quiescent CD4+ t cells. J Virol 83: 6222–6233.

260. Karn J, Stoltzfus CM (2012) Transcriptional and posttranscriptional regulation of HIV-1 gene expression. Cold Spring Harb Perspect Med 2.

261. Contreras X, Schweneker M, Chen CS, McCune JM, Deeks SG, et al. (2009) Suberoylanilide hydroxamic acid reactivates HIV from latently infected cells. J Biol Chem 284: 6782–6789.

262. Gallastegui E, Marshall B, Vidal D, Sanchez-Duffhues G, Collado JA, et al. (2012) Combination of biological screening in a cellular model of viral latency and virtual screening identifies novel compounds that reactivate HIV-1. J Virol 86: 3795–3808.

263. Archin NM, Liberty AL, Kashuba AD, Choudhary SK, Kuruc JD, et al. (2012) Administration of vorinostat disrupts HIV-1 latency in patients on antiretroviral therapy. Nature 487: 482–485.

264. Tozer TN, Rowland M (2006) Introduction to pharmacokinetics and pharmacodynamics: the quantitative basis of drug therapy. Lippincott Williams & Wilkins.

265. Bonate PL, Steimer JL (2006) Pharmacokinetic-pharmacodynamic modeling and simulation. Springer.

266. Keizer RJ, Huitema AD, Schellens JH, Beijnen JH (2010) Clinical pharmacokinetics of therapeutic monoclonal antibodies. Clinical pharmacokinetics 49: 493–507.

267. Dominguez R (1934) Studies of renal excretion of creatinine. II. volume of distribution. Experimental Biology and Medicine 31: 1146–1149.

268. Riegelman S, Loo J, Rowland M (1968) Concept of a volume of distribution and possible errors in evaluation of this parameter. Journal of pharmaceutical sciences 57: 128–133.

269. Sahin S, Benet LZ (2008) The operational multiple dosing half-life: a key to defining drug accumulation in patients and to designing extended release dosage forms. Pharmaceutical research 25: 2869–2877.

270. Toutain PL, Bousquet-Mélou A (2004) Plasma terminal half-life. Journal of veterinary pharmacology and therapeutics 27: 427–439.

271. Boxenbaum H, Battle M (1995) Effective half-life in clinical pharmacology. The Journal of Clinical Pharmacology 35: 763–766.

272. Hidalgo M, Eckhardt SG, Clendeninn NJ, Garrett-Mayer E (2010) Principles of Anticancer Drug Development. Springer Science & Business Media.

273. Min S, Song I, Borland J, Chen S, Lou Y, et al. (2010) Pharmacokinetics and safety of S/GSK1349572, a next-generation hiv integrase inhibitor, in healthy volunteers. Antimicrobial agents and chemotherapy 54: 254–258.

274. Brocks DR, Mehvar R (2010) Rate and extent of drug accumulation after multiple dosing revisited. Clinical pharmacokinetics 49: 421–438.

275. Yamaoka K, Nakagawa T, Uno T (1978) Statistical moments in pharmacokinetics. Journal of pharmacokinetics and biopharmaceutics 6: 547–558.

276. Greenberg HE, England MJ, Hellriegel ET, Bjornsson TD (1997) Time of peak drug concentration after a single dose and a dose at steady state. The Journal of Clinical Pharmacology 37: 480–485.

277. Bischoff KB, Dedrick RL (1970) Generalized solution to linear, two-compartment, open model for drug distribution. Journal of theoretical biology 29: 63–83.

278. Hill S (2004) Pharmacokinetics of drug infusions. Continuing Education in Anaesthesia, Critical Care & Pain 4: 76–80.

279. Arab-Alameddine M, Fayet-Mello A, Lubomirov R, Neely M, Di Iulio J, et al. (2012) Population pharmacokinetic analysis and pharmacogenetics of raltegravir in hiv-positive and healthy individuals. Antimicrobial agents and chemotherapy 56: 2959–2966.

280. von Kleist M, Huisinga W (2009) Pharmacokinetic–pharmacodynamic relationship of nrtis and its connection to viral escape: An example based on zidovudine. European journal of pharmaceutical sciences 36: 532–543.

281. Law V, Knox C, Djoumbou Y, Jewison T, Guo AC, et al. (2014) DrugBank 4.0: shedding new light on drug metabolism. Nucleic Acids Res 42.

282. Yuen GJ, Lou Y, Bumgarner NF, Bishop JP, Smith GA, et al. (2004) Equivalent steady-state pharmacokinetics of lamivudine in plasma and lamivudine triphosphate within cells following administration of lamivudine at 300 milligrams once daily and 150 milligrams twice daily. Antimicrob Agents Chemother 48: 176–182.

283. Moles CG, Mendes P, Banga JR (2003) Parameter estimation in biochemical pathways: a comparison of global optimization methods. Genome research 13: 2467–2474.

284. Banga JR (2008) Optimization in computational systems biology. BMC systems biology 2: 47.

285. Gutenkunst RN, Waterfall JJ, Casey FP, Brown KS, Myers CR, et al. (2007) Universally sloppy parameter sensitivities in systems biology models. PLoS Comput Biol 3: e189.

286. Audoly S, Bellu G, D'Angió L, Saccomani MP, Cobelli C (2001) Global identifiability of nonlinear models of biological systems. Biomedical Engineering, IEEE Transactions on 48: 55–65.

287. Raue A, Kreutz C, Maiwald T, Bachmann J, Schilling M, et al. (2009) Structural and practical identifiability analysis of partially observed dynamical models by exploiting the profile likelihood. Bioinformatics 25: 1923–1929.

288. Chen WW, Schoeberl B, Jasper PJ, Niepel M, Nielsen UB, et al. (2009) Input-output behavior of ErbB signaling pathways as revealed by a mass action model trained against dynamic data. Mol Syst Biol 5: 239.

289. Chis OT, Banga JR, Balsa-Canto E (2011) Structural identifiability of systems biology models: A critical comparison of methods. PLoS One 6: e27755.

290. Engl HW, Flamm C, Kügler P, Lu J, Müller S, et al. (2009) Inverse problems in systems biology. Inverse Problems 25: 123014.

291. White L, Evans N, Lam T, Schukken Y, Medley G, et al. (2001) The structural identifiability and parameter estimation of a multispecies model for the transmission of mastitis in dairy cows. Mathematical biosciences 174: 77–90.

292. Kirkpatrick S, et al. (1983) Optimization by simmulated annealing. science 220: 671–680.

293. Tibshirani R (1996) Regression shrinkage and selection via the lasso. Journal of the Royal Statistical Society Series B (Methodological) : 267–288.

294. Hastie T, Tibshirani R, Friedman J (2009) The Elements of Statistical Learning: Data Mining, INference and Prediction. Springer.

295. Hoerl AE, Kennard RW (1970) Ridge regression: Biased estimation for nonorthogonal problems. Technometrics 12: 55–67.

296. Ngo S, Kemény S, Deák A (2003) Performance of the ridge regression method as applied to complex linear and nonlinear models. Chemometrics and intelligent Laboratory systems 67: 69–78.

297. Friendly M (2013) The generalized ridge trace plot: Visualizing bias and precision. Journal of Computational and Graphical Statistics 22: 50–68.

Declaration of Originality

I declare that this is a true copy of my thesis and that this thesis has not been submitted for a higher degree to any other University or Institution. Information derived from the work of others has been acknowledged in the text and references are given in the bibliography.

Weinheim, March 7, 2016

Sathej Gopalakrishnan